

Alma Mater Studiorum - Università di Bologna

TESI DI
DOTTORATO DI RICERCA IN FISICA
CICLO XXVIII

Settore concorsuale di afferenza: 02/A2
Settore Scientifico Disciplinare: FIS/02

**Time-dependent simulations of
one-dimensional quantum systems:
from thermalization to localization**

presentata da Piero Naldesi

Coordinatore Dottorato:
prof. Gastone Castellani

Relatore:
prof.ssa Elisa Ercolessi

Correlatore:
prof. Tommaso Roscilde

Esame finale anno 2016

Abstract

In the first part of this thesis we study the Aubry-Andr model for interacting fermions. We numerically describe its phase diagram at half filling, performing both DMRG and QMC simulations. We show the existence of a localized phase and other three regimes: luttinger liquid, charge density wave and productstate. We study the properties of the excited states of the Hamiltonian, looking for a many-body mobility edge in the spectrum, i.e. an energy threshold that separates localized from ergodic states and analyzing many indicators we prove its existence. Finally we propose a quench-spectroscopy method for detecting the mobility edge dynamically.

In the second part we study the expansion dynamics of two bosons in a one-dimensional lattice as ruled by the Bose-Hubbard model Hamiltonian, both in the attractive and repulsive regime. Using the Bethe Ansatz we identify the bound states effects unambiguously and how the two-particles state evolves in time. We show that, independently from the kind of initial state, there exists a strong relation between the expansion velocity and the presence of bound states in the spectrum. Moreover, we discuss the role of the discrete lattice in expansion of the system.

In the third part we study the time evolution of the entanglement entropy in the Ising model, when it is dynamically driven across a quantum phase transition with different velocities. We computed the time-evolution of the half chain entanglement entropy and we found that, depending on the velocity at which the critical point is reached, it displays different regimes: an adiabatic one when the system evolves according to the instantaneous ground state; a sudden quench regime when the system remains frozen to its initial state; and an intermediate one, where the entropy starts growing linearly but then displays oscillations. Moreover, we discuss the Kibble-Zurek mechanism for the transition between the paramagnetic and the ordered phase.

Contents

Introduction	vii
1 The Aubry-André model	1
1.1 Aubry-André model and self-duality	1
1.2 Spectral properties and numerical results	5
2 Many-body Localization in Quasiperiodic Potentials	9
2.1 Many-Body Localization	9
2.2 Hamiltonian and ground-state properties	13
2.3 Properties of the spectrum	17
2.3.1 Levels statistics	17
2.3.2 Entropy and fluctuations	21
2.3.3 Evidences for mobility edge	24
2.4 Mobility-edge spectroscopy via quench	25
2.4.1 Quench energy	25
2.4.2 Time-dependent Entropy and Density Fluctuations	28
2.5 Conclusions	32
3 Bound states and expansion dynamics of bosons on a one-dimensional lattice	33
3.1 The two-boson problem on a lattice: exact results	33
3.2 Dynamics of product states	37
3.2.1 $ \psi_{PS}^2\rangle$: two bosons on adjacent sites	37
3.2.2 $ \psi_{PS}^1\rangle$: two bosons on the same site	41
3.3 Dynamics of entangled states	42
3.4 Effect of the lattice on the expansion dynamics	46
3.5 Conclusions	48
3.A Expansion velocities for product states in the non-interacting case	49
3.B $U \leftrightarrow -U$ inversion theorem	50
4 Dynamics of entanglement entropy crossing a quantum phase transition	53
4.1 The model	53
4.2 Entanglement Dynamics	56
4.2.1 Adiabatic and sudden regimes	56

4.2.2	Fast sweeps	57
4.2.3	Slow sweeps	59
4.3	Kibble-Zurek Physics	59
4.3.1	Entanglement entropy	60
4.3.2	Schmidt gap	61
4.4	Conclusions	62
4.A	Exact solution of the Ising model	65
4.B	Initial structure of the entanglement spectrum	67
4.C	Bipartite quantities in free fermionic systems	68
	Bibliography	73

Introduction

Recent experimental progresses in atomic, molecular, optical and condensed matter physics have made possible to control and study quantum many-body systems with high accuracy at and out of equilibrium [1–7]. The birth of this new field in the experimental research has renewed the interest on the dynamics of isolated quantum many-body systems, a field vastly studied from a theoretical point of view over the years, but which had so far mainly an academical interest [8]. One of the issues that received an increasing attention in the last years has been the relaxation dynamics of closed quantum system driven out of equilibrium. Two different scenario have been so far observed: thermalization and localization.

In isolated quantum systems, thermalization may occur only if the system itself acts as its own heat bath. In this regime, often called “ergodic”, the long-time behavior of the system is described by a thermal density matrix, all its eigenstates follow the Eigenstate Thermalization Hypothesis (ETH) [9–11] and standard statistical mechanics can be applied to predict the equilibrium properties of the system. This hypothesis, formulated in the early 90s by Deutsch and Srednicki, asserts that the expectation value of any reasonable few-body observable in a certain eigenstate $|\psi_i\rangle$ of a closed system is equal to the microcanonical average of that operator, in the limit in which $|\psi_i\rangle$ is the only state in the microcanonical energy window. When the ETH holds, the thermodynamics of the system is ruled by all the so called “single-eigenstate ensembles”, i.e. ensembles constructed by just one eigenstates of the full system’s Hamiltonian. All these ensembles reproduce the correct thermal equilibrium properties of a subsystem as in the case of standard statistical mechanics.

There are mainly two classes of systems that violate the ETH: integrable and localized systems. For integrable systems, i.e. systems that have an infinite number of non-trivial conserved charges that restrict the dynamics to a portion of the Hilbert space, it has been shown that is possible to build a “generalized Gibbs ensemble” (GGE) [11–13] describing the stationary state reached after relaxation.

For localized systems some correlation from the initial state will last forever during the time evolution and the system will fail to thermalize in any sense. The study of quantum localization started in 1958 when Anderson [14] re-

alized that in a one dimensional system of non interacting particles an infinitesimal disorder is sufficient to localize all the eigenstates of the spectrum. This result aroused interest and in the last 60 years many physicists have addressed their research to this field. Anderson localization has also been recently observed experimentally in different setups [15, 16]

One of the main questions that are still to answer is the following: can localization survive interactions between particles leading to the so-called Many Body Localization (MBL) [17, 18]? Clearly the problem of MBL is not easy, and it is still far from being completely understood.

In recent times, after the work by Basko et al. [19], the existence of MBL has been demonstrated from many different perspectives: perturbative arguments [17, 19–21], numerical exact diagonalization and Density matrix renormalization group (DMRG) studies [22–28], mathematical proof [29] and recently also experimental realization [30–32].

Localized systems exhibit many intriguing phenomena. As described before the excited states of a localized system can not be considered as thermal states since they do not fulfill the ETH and they are characterized by a non-extensive entanglement entropy that violate the *volume law* [33]. From a dynamical point of view localized systems are characterized by a sub-diffusive, in many situations logarithmic, growth of the entanglement entropy (starting the evolution from a product state) [34] as well as by the absence of diffusion and dissipation. Another interesting phenomenon that MBL system can exhibit, is the many-body mobility edge [26], namely an energy threshold in the energy spectrum that separate localized eigenstate from those that respects the ETH.

Another class of systems that display intermediate features between truly disordered and translational invariant are almost periodic systems. These systems, known also as quasiperiodic systems, have been deeply studied in the last thirty years from both a physical and mathematical point of view [35–60]. An example is provided by quasiperiodic crystals [61–65], namely solids exhibiting different periodic structures whose periods are incommensurate with each other.

One of the first quasiperiodic system that has been studied is the so-called Aubry-André [36], or Harper [35], model, that describes a quantum particle in a lattice subject to a chemical potential spatially modulated by a cosine incommensurate with the lattice as well as, for a particular value of the couplings, an electron moving in a two-dimensional lattice in the presence of a perpendicular magnetic field [52, 60]. This model has been extensively studied in several contexts, and there exist excellent reviews [35, 36, 42, 49, 50, 54, 55, 59, 66].

The most peculiar feature of the Aubry-André model is that, for a truly incommensurate potential [46], the system shows a metal-insulator transition at a finite critical value of the quasiperiodic potential strength. This critical point, called *self-dual point* separates localized and extended states at any energy the phase diagram of the model.

Such a systems as the advantage of showing localization properties similar to the truly disordered, but it may be implemented experimentally in a much easier way [15, 30, 67]. Localization in a system of interacting particle, i.e. MBL, has been first observed in an ultracold-atom experiment simulating a quasiperiodic model [30].

In the first part of this thesis, after a brief overview of single particle quasiperiodic system in Ch. 1, we investigate in Ch. 2 the physics of the one-dimensional interacting Aubry-André model. The latter describes the motion of interacting spinless fermions in a incommensurate quasiperiodic potential and is represented by the Hamiltonian:

$$\mathcal{H}^{int} = \sum_{i=1}^{L-1} \left[-j \left(c_i^\dagger c_{i+1} + c_{i+1}^\dagger c_i \right) + V n_i n_{i+1} \right] + \sum_{i=1}^L \Delta \cos(2\pi(\alpha i + \phi)) n_i . \quad (1)$$

Here c_l^\dagger, c_l are fermionic operators, n_i is number operator and j, V, Δ are respectively the hopping rate, the interaction and the quasiperiodic strength. In order to have a quasiperiodic potential the coefficient α must be an irrational number [46]. Since the model is not exactly solvable we will use a mix of analytical (on the two axes) and numerical results to describe the ground state phase diagram as a function of quasi-disorder and interaction. At half filling, we observe the existence of four different phases: Luttinger liquid, charge-density wave, phase separation and localized. Especially we estimate for a particular value of the interaction $V = 2$ the Luttinger liquid to localized transition to occur at $\Delta = 2.5 \pm 0.1$ and $\Delta = 1.5 \pm 0.1$ respectively in the ground and in most excited state of the Hamiltonian.

Motivated by this asymmetry in the two transitions, we then studied the properties of the excited states of the Hamiltonian looking for a many-body mobility edge in the spectrum, i.e. an energy threshold that separates localized from ergodic states. As a first indicator, we analyze the changing in the level statistics of adjacent energy gaps between a Poissonian distribution, for the localized phase, to a distribution consistent with the Gaussian orthogonal ensemble of random matrices, for the ergodic regime. We also analyze the crossover in the scaling of the entanglement entropy from volume to area law, at the transition from ergodic to localized regimes respectively, and its standard deviation that has been shown to diverge with the system size at the boundary. From the results of all these indicators, that, as we will show, are in perfect agreement with each others, we obtain clear evidences for a

many-mobility edge in the spectrum of the Hamiltonian.

In the last section we propose a method for detecting the many-body mobility edge via quench-spectroscopy. The many-body mobility edge can be observed studying the time evolution of a system driven out of equilibrium by a global quench. In fact there is a direct relation between the quench amplitude and the energy window we populated in the spectrum with the quench. Our conjecture is that the expectation value of a given operator over the evolved state of the system after a certain quench, after a long enough time, will be the same as if calculated on the eigenstates in the corresponding energy window. Moreover, this protocol is easily implementable in an experimental setup of ultracold-atoms and can, in principle, lead to the direct observation of the many-mobility edge.

We will apply our method to the interacting Aubry-André model studying the long time behavior of two bipartite quantities: the entanglement entropy and the density fluctuations. We find a good agreement between the long time behavior of the system and the properties of its excited states demonstrating the validity of our surmise.

In the second part of this work, Ch. 1, again related to the general problem of the dynamics in quantum many-body physics, we will study two different protocols for driving the system out of equilibrium: a *sudden quench* for a bosonic Hamiltonian in a lattice and an *adiabatic evolution* in the transverse field Ising model.

The expansion dynamics of bosonic gases in optical lattices has recently been the focus of an increasing attention, both experimental and theoretical. Since the first experimental realizations of Bose-Einstein condensates [68–70], huge efforts have been devoted to the study of ultra-cold bosonic atoms loaded into magnetic-optical traps [71, 72]. For one-dimensional systems a variety of interesting phenomena have been observed: the non-thermalization of a Lieb-Liniger gas [1], the dynamical fermionization of expanding hardcore bosons [73, 74], the quantum distillation of double occupations [75–77] and the dynamical quasi-condensation of an initial product state [78, 79]. Motivated by the experimental results of Ref. [76], we study the expansion dynamics of a bosonic system by means of the well-known Bose-Hubbard model Hamiltonian:

$$\mathcal{H}(U) = -j \sum_{k=-L/2}^{L/2} \left(b_k^\dagger b_{k+1} + b_{k+1}^\dagger b_k \right) + \frac{U}{2} \sum_{k=-L/2}^{L/2} \hat{n}_k (\hat{n}_k - 1) \quad (2)$$

here b_k, b_k^\dagger are bosonic operators and j and U are respectively the hopping and the on-site interaction coefficients.

In this case, despite the non-integrability of the general N-particles Hamiltonian, it is possible to solve the two particles problem exactly, thanks to the separation of center-of-mass and relative coordinates, obtaining information on all the eigenstates and eigenenergies.

We analyze the dynamical expansion starting from two different classes of initial conditions: *a)* product states, corresponding to bosons with well defined initial positions in real space, and *b)* entangled states, corresponding to the ground states of a non interacting Bose-Hubbard Hamiltonian, in an open box of size l .

We show that, independently from the kind of initial state, there exists a strong, almost inverse, relation between the expansion velocity and the presence of bound states in the spectrum, providing a quantitative support to the importance of the bound pair states on the system's dynamics. In addition, we discuss a number of quantitative and qualitative features about the expansion of initially confined bosons on a 1D lattice, as well as the role of the lattice during the expansion, compared to the continuum case.

In the third part of this thesis, Ch. 1, we deal with the problem of studying the time evolution of the Ising model [80–82] in a time dependent transverse field, when it is driven from one phase to another one by allowing the field to change in time. The Hamiltonian of the model is:

$$\mathcal{H} = - \sum_{j=1}^L [\sigma_j^z \sigma_{j+1}^z + h(t) \sigma_j^x] \quad (3)$$

here $\vec{\sigma}$ are the usual Pauli matrices and the magnetic field varies as $h(t) = h_i + \frac{t}{\tau}$ where τ is the inverse of the velocity at which the system is driven and we choose $h_i > 1$ to be in the paramagnetic phase. For different values of τ we obtained three qualitatively different regimes: an adiabatic one (large τ) when the system evolves according to the instantaneous ground state, a sudden quench (small τ) regime when the system is essentially frozen to its initial state and an intermediate one, where the entropy starts growing linearly (because of finite speed the correlations spreading in the system [83, 84]) and starting then to oscillate because the system ends up, after passing the critical point, in a linear combination of excited states of the instantaneous Hamiltonian.

The transition between the paramagnetic and the ordered phase gives us the perfect framework for discuss the Kibble-Zurek mechanism [85–89] that hallows us to predicts the scaling of the number of topological defects produced after the dynamical transition of a critical point.

The evolution of the system can be divided into three parts: a first *adiabatic* one, where the wave function of the system coincides with the ground state of instantaneous Hamiltonian. A second *impulsive*, closed to the critical point where the correlation length ξ starts to diverge and the wave function

of the system is practically frozen and a third adiabatic one, as the system is driven away from the critical point [89]. We will also analyze the formation of topological defects on distances smaller than the correlation length ξ . According to Kibble-Zurek mechanism ξ is supposed to scale as $\xi \sim \tau\nu/(\tau z + 1)$ where, τ is the inverse velocity defined before, and ν and z are the critical exponents that characterize the crossed transition.

The results from the second and third part of this thesis have been collected in two papers published during the PhD.

The part second is published in:

C. Degli Esposti Boschi, E. Ercolessi, L. Ferrari,
P. Naldesi, F. Ortolani, L. Taddia
*Bound states and expansion dynamics of interacting bosons
on a one-dimensional lattice,*
[Phys. Rev. A **90**, 043606 \(2014\).](#)

while the third in:

E. Canovi, E. Ercolessi, P. Naldesi, L. Taddia, D. Vodola,
*Dynamics of entanglement entropy and entanglement spectrum
crossing a quantum phase transition,*
[Phys. Rev. B **89**, 104303 \(2014\).](#)

1

The Aubry-André model

“Philip Warren é ora di rimettere a posto la tua camera!
Aspetteremo la localizzazione la settimana prossima..”
“Ma uffa però mammaaa!!”

— La signora Anderson sul disordine

In the first Sec. 1.1 of this chapter, we review the main features of localization in quasiperiodic systems of non interacting particles discussing the Aubry-André model and its self-duality. We then describe the properties of the energy spectrum in Sec. 1.16 in the different regimes. In this last section we also how to characterize numerically the localization transition via the Inverse Participation Ratio.

1.1 Aubry-André model and self-duality

The single particle Hamiltonian for the fermionic version of the model is composed by a kinetic term, plus a term that couples the quasiperiodic potential with the density:

$$\mathcal{H} = \sum_{l=1}^L \left[-j \left(c_l^\dagger c_{l+1} + c_{l+1}^\dagger c_l \right) + h_l n_l \right] \quad h_l = \Delta \cos(2\pi\alpha l + \phi) \quad (1.1)$$

Here c_l^\dagger, c_l are fermionic creation and annihilation operators, n_l is the number operator defined as $n_l = c_l^\dagger c_l$, j is the hopping rate between neighboring sites and Δ is the strength of the on-site potential, spatially modulated by a cosine with wave number $2\pi\alpha$ and phase shift ϕ .

This Hamiltonian can be mapped onto a hardcore-boson model in a bichromatic potential via a Jordan-Wigner transformation 4.A. Both in the case of bosons or fermions the Aubry-André Hamiltonian can be now implemented in experiments with ultracold atoms trapped in optical lattices [42, 67, 90–94].

Following the seminal work by Aubry André, we derive the self-duality argument for the model that will give us insight into the phase diagram of the system.

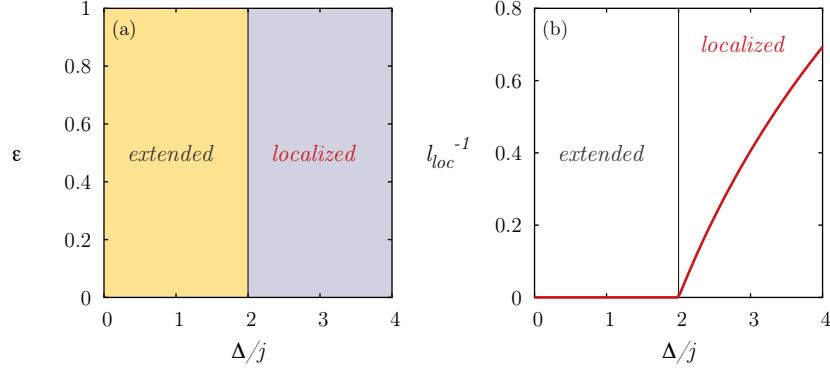


Figure 1.1: The phase diagram of the Aubry-André model, in panel (a), is separated at any energy in the two extended and localized regimes from the line $\Delta/j = 2$. The inverse energy independent localization length as a function of the disorder strength, in panel (b).

Without loss of generality, as we will discuss in the following, we set the parameter α equal to the inverse of the golden number, $\alpha = (\sqrt{5} - 1)/2$. We start the study of the Hamiltonian (1.1) introducing a new set of fermionic operators η_k defined by the following canonical transformation

$$\eta_k = \sum_l \psi_{k,l} c_l \quad \text{with} \quad \sum_k \psi_{k,l} \psi_{k,l'}^* = \delta_{l,l'} \quad (1.2)$$

and recast the Hamiltonian in a diagonal form

$$\mathcal{H} = \sum_k \epsilon_k \left(\eta_k^\dagger \eta_k - \frac{1}{2} \right) \quad (1.3)$$

where both the energy ϵ_k and the coefficients $\psi_{k,l}$ have to satisfy the following *almost Mathieu equation* for every k (we drop the index k for simplify the notation).

$$j(\psi_{l-1} + \psi_{l+1}) + \Delta \cos(2\pi\alpha l + \phi) \psi_l = \epsilon \psi_l . \quad (1.4)$$

We want to transform now the coefficients ψ_l to reciprocal space

$$\chi_l = \sum_m \psi_m e^{im(2\pi\alpha l + \phi)} e^{il\phi} \quad (1.5)$$

where, from eq (1.4), χ_l has to satisfy the following equation

$$\frac{\Delta}{2} (\chi_{l-1} + \chi_{l+1}) + 2j \cos(2\pi\alpha l + \phi) \chi_l = \epsilon \chi_l . \quad (1.6)$$

Now the self-duality is clear since the two equations (1.4) and (1.6) have the same form but with the roles of Δ and $2j$ exchanged.

From equation (1.5) it follows directly that χ_l and ψ_m are connected in particular, if the first is localized, the second is extended, namely:

$$\sum_l |\chi_l|^2 < \infty \quad \rightarrow \quad \sum_m |\psi_m|^2 = \infty . \quad (1.7)$$

From the symmetry of the dual equations (1.4) and (1.6) we can deduce that is valid also the opposite relation: if χ_l is extended, then ψ_m is localized.

$$\sum_l |\chi_l|^2 < \infty \quad \rightarrow \quad \sum_m |\psi_m|^2 = \infty . \quad (1.8)$$

Another step forward in the description of localized and extended states can be taken studying the characteristic exponent $\gamma(E)$ [95] that is defined for a state ψ with energy E as

$$\gamma(E) = - \lim_{m \rightarrow \infty} \frac{\log(\psi_m^2 + \psi_{m+1}^2)}{2m} \geq 0 \quad (1.9)$$

where ψ_m is the coefficient of the wave function at site m . This quantity determines the asymptotic decay of the wave function. From the definition it is always non negative, it vanishes for extended states and it gives the inverse of the localization length l_{loc} for localized states.

The characteristic exponent $\gamma(E)$ is linked to the density of states $\rho(E)$ via a formula due to Thouless [96] that we directly apply to equation (1.4) to obtain the characteristic exponent $\gamma_\psi(E)$ for a state ψ with energy E :

$$\gamma_\psi(E) = \int_{E_{min}}^{E_{max}} dE' \log \left| \frac{E - E'}{t} \right| \rho(E') . \quad (1.10)$$

This formula, that holds for one-dimensional random systems with nearest-neighbor hopping, is also valid for quasiperiodic systems only provided that α , defined in equation (1.1), is not only irrational but as well a Diophantine number [46].

We want now to apply the same formula to equation (1.6), in order to obtain the characteristic exponent $\gamma_\chi(E)$ for the states χ . Since the two dual

equations (1.4) and (1.6) have the same density of states [36] we obtain

$$\gamma_\chi(E) = \int_{E_{min}}^{E_{max}} dE' \log \left| \frac{2(E - E')}{\Delta} \right| \rho(E') \quad (1.11)$$

and straightforwardly from equations (1.10, 1.11) we get a relation between the two characteristic exponents

$$\gamma_\psi(E) = \gamma_\chi(E) + \log(\Delta/2j) \ . \quad (1.12)$$

As we discussed above, if the eigenstates ψ are extended, then $\gamma_\psi(E) = 0$. From the previous equation we have that this condition is met only for $\Delta/j \leq 2$:

$$\gamma_\chi(E) = \log(2j/\Delta) \geq 0 \quad \rightarrow \quad \Delta/j \leq 2 \ . \quad (1.13)$$

On the other hand, if the eigenstates ψ are localized, then the dual states χ are extended with $\gamma_\chi(E) = 0$, i.e.

$$\gamma_\psi(E) = \log(\Delta/2j) \geq 0 \quad \rightarrow \quad \Delta/j \geq 2 \ . \quad (1.14)$$

Since the characteristic exponent gives us the inverse of the localization length for localized states, we can conclude that:

$$l_{loc} = \frac{1}{\log(\Delta/2j)} \ . \quad (1.15)$$

Equations (1.13) and (1.14) show us that, at any energy, the eigenstates ψ are extended for $\Delta/j \leq 2$ and localized for $\Delta/j \geq 2$, and that the transition occurs at $\Delta/j = 2$ giving us the phase diagram of the model in Fig. 1.1.

The really important feature of this transition is that it occurs at every energy for the same intensity of the quasiperiodic potential strength $\Delta/j = 2$. From equation (1.15) we can see also that the localization length is energy-independent. Both features are strikingly in contrast with the case of the Anderson model [14], where the transition occurs for infinitesimal disorder with a localization length that depends both on the disorder strength and on the energy.

Generalizations of this model [97, 98] to long-range hopping have been studied. In these systems the duality relation is not anymore energy-independent and therefore the transition appears at a different strength of the potential for different energy. For a particular value of the Hamiltonian parameters we can then observe a transition in energy between localized and extended states: the critical point that separates the two regimes is called mobility

edge.

The last aspect we want to emphasize is the relation between commensurate and incommensurate system. We said above that a necessary and sufficient condition for the localization transition is to choose the wave number α between the irrational Diophantine numbers [46]. This condition cannot be completely fulfilled in a realistic framework for numerical or experimental realizations. In both situations the system has a finite-size and moreover any number can be in the reality given only with a finite number of digit resulting, as matter of fact, rational. The relation between commensurate and incommensurate potentials it has been the subject of some studies [36, 42] and it has been found that for a realistic system it is sufficient to require to have a large enough number of lattice sites within the actual periodicity of the potential and a size of the system comparable with the latter in order to avoid periodic replicas. A detailed discussion of this problem can be found in a recent work [42].

1.2 Spectral properties and numerical results

The energy spectrum of the Aubry-André model has been studied in numerous works [49, 51–53, 56–58, 99] and it displays very rich structure in both the extended and localized regimes Fig. 1.2.

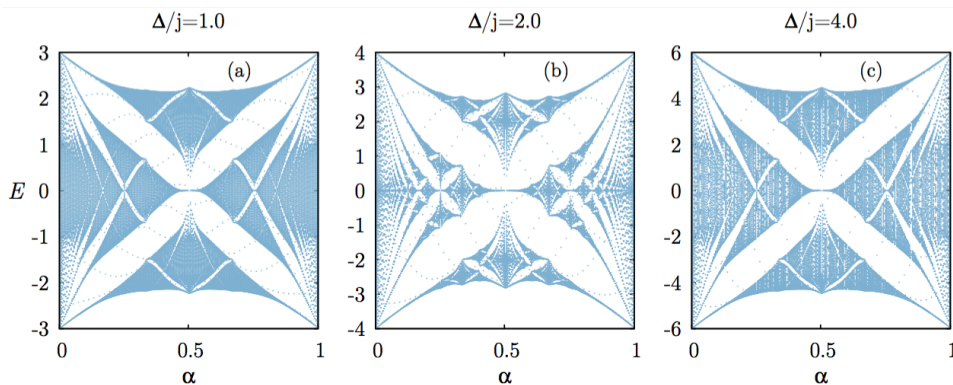


Figure 1.2: Energy spectrum of the Aubry-André model as a function of the wave number α for different values of the ratio Δ/j calculated for a lattice with length $L = 200$. At the transition, $\Delta/j = 2$, the spectrum reproduce a Hofstadter butterfly and shows a rich fractal structure.

At $\Delta = 0$ the single particle spectrum is continuum and given by the usual dispersion relation $\epsilon_k = -2j \cos(k)$ with the momentum quantized as $k_n = 2\pi n/L$.

Turning on the quasi-disorder potential the spectrum organizes in increasingly narrow bands separated by minigaps, as it can be seen in Fig. 1.5 a/b.

Increasing the quasi-disorder the number of minigaps increases in turn and at the transition point $\Delta/j = 2$ the spectrum, in the thermodynamic limit, forms a Cantor set [100]. At this critical point the spectrum as a function of the parameter α is really peculiar and it reproduces a *Hofstadter butterfly* as shown in Fig. 1.2b. This case has been widely studied, since it reproduces the physics of a quantum particle moving on a two dimensional lattice in a transverse magnetic field [52, 60].

Another interesting feature is that, in the localized regime for $\Delta > 2$ the spectrum is strongly dependent on the phase ϕ and it thus changes for different realizations of the disorder as can be seen in Fig. 1.3. This is to be contrasted with the extended regime in which the dependence on ϕ is very weak.

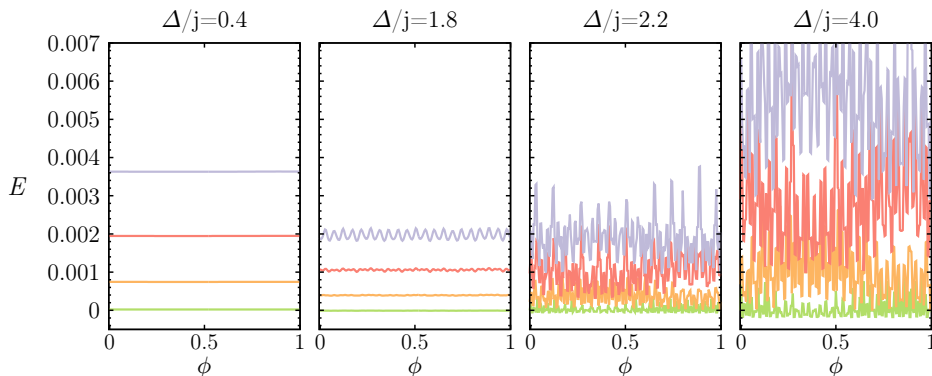


Figure 1.3: First four energy levels in the spectrum as a function of the phase ϕ for different values of the ratio Δ/j calculated for a lattice with length $L = 200$. Energies have been rescaled to zero and the phase ϕ is in units of 2π .

One of the observables that can be considered for describing the localization feature of every eigenstate is the inverse participation ratio (IPR). For a given state ψ_k , it is defined as:

$$IPR_k = \frac{\sum_l |\psi_{k,l}|^4}{(\sum_l |\psi_{k,l}|^2)^2} \quad (1.16)$$

where the index n runs over all the sites of the chain. The IPR gives us the inverse of the number of sites occupied by the wave function: it thus approaches zero as $1/L$ for an extended state, while it effectively tends to 1 for a wave-function localized on a single site. This strong sensitivity to the nature of the wave-function, makes the IPR a good parameter for studying the localization transition.

We want now to probe numerically the analytic results obtained in the previous sections. The single particle Hamiltonian (1.1), is defined by a $L \times L$

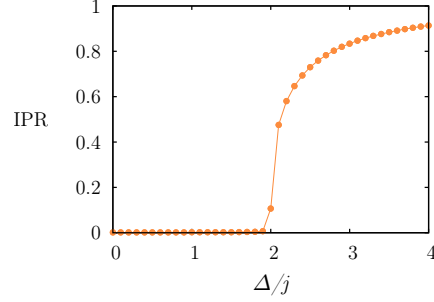


Figure 1.4: The inverse participation ratio IPR as a function of the disorder strength Δ averaged over the full spectrum for a lattice with length $L = 200$, is a good numerical indicator for studying the localization transition in the full spectrum.

square matrix [80] with L the size of the system, that can be easily diagonalized numerically giving us direct access to all the eigenfunctions and eigenvalues.

In Fig. 1.4 we show the IPR as a function of the quasi-disorder strength Δ averaged over all the eigenstates in the spectrum for a lattice of $L = 200$ sites. The IPR vanishes in the extended phase and becomes finite for $\Delta/j \geq 2$ reaching 1 in the limit of strong disorder, where all the eigenstates are localized, exhibiting the transition for $\Delta/j = 2$.

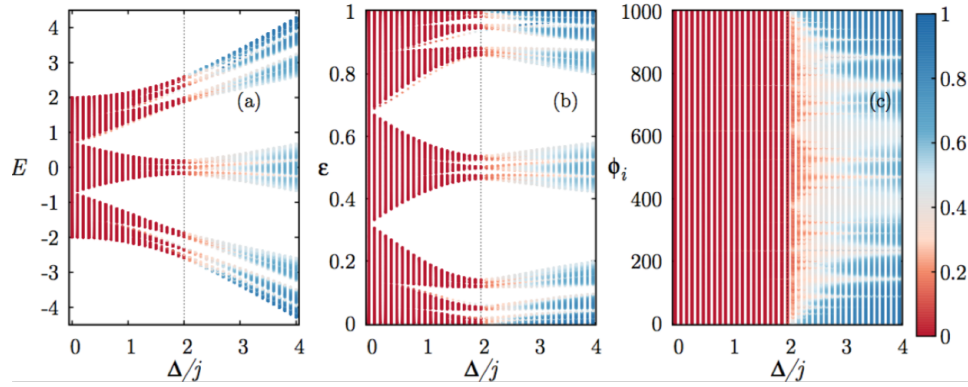


Figure 1.5: Color plot of the IPR for the Aubry-André model as a function of the energy, in panel (a), for different values of the ratio Δ/j calculated for a lattice with length $L = 200$. In panel (b) the energy have been rescaled to the window $[0, 1]$ and in panel (c) with the number of the eigenstates in the ordinate axis, in ascending order of energy.

We perform the numerical analysis of the IPR state by state as a function of the ratio Δ/j on a lattice with length $L = 200$. In Fig. 1.5 we show the color plot of the inverse participation ratio as a function of the energy, in

panel (a), for different values of the ratio Δ/j . In panel (b) energy have been rescaled to the window $[0, 1]$ as:

$$\epsilon = \frac{E - E_{min}}{E_{max} - E_{min}} \quad (1.17)$$

where E_{min} and E_{max} are respectively the ground and the maximum excited states. In panel (c) we show the same plot but with the eigenstate's number in the ordinate axis, in ascending order of energy. We see that the localization transition between the extended and localized regime at critical value $\Delta/j = 2$ is well highlighted by IPR.

2

Many-body Localization in Quasiperiodic Potentials

“Localizziamoci e partite”

— Detto popolare

After introducing in the first Sec. 2.1 the main idea of Many-Body Localization we will introduce in Sec. 2.2 the interacting Aubry-André model (2.8). The ground-state phase diagram of the model is then analyzed in Sec. 2.2 giving particular attention to the Luttinger liquid - localized transition. We then turn to the spectral properties of the Hamiltonian analyzing both the level statistics and the entanglement entropy of the full spectrum proving the existence of a many-body mobility edge. In Sec. 2.4 we propose a method for detecting the mobility edge via quench spectroscopy. We then apply it to the interacting Aubry-André model (2.8) and we provide evidences of its validity. Finally, in Sec. 2.5, we draw our conclusions and comment on possible developments both from a theoretical and from an experimental point of view.

2.1 Many-Body Localization

A system of non interacting particles in presence of disorder, either quasiperiodic as we discussed in Ch. 1 or purely random as in the Anderson model [14], can exhibit the phenomenon of localization. The question of how localization can survive interactions between particles, leading to the so-called many-body localization (MBL) [18, 33, 101], has been of interest to several recent studies after the work by Basko et al. [19] and it is still far from being completely understood. One of the most peculiar properties of MBL is its violation of the eigenstate thermalization hypothesis (ETH) [9–11] resulting in the absence of thermalization. This hypothesis, formulated in the early 90s by Deutsch and Srednicki in the contest of quantum chaos theory, has been verified numerically for several many-body systems [11, 102–105].

In order to introduce the main concept of the ETH, let us consider an isolated quantum N -body system with Hamiltonian \mathcal{H} . Let $|\alpha\rangle$ denote the eigenvectors of \mathcal{H} with eigenvalues E_α and let \hat{A} be a given many-body observable. Starting from the ground state $|\psi_i\rangle$ of a different Hamiltonian $\mathcal{H}_i = \mathcal{H} + \lambda\mathcal{H}_0$, we will turn λ to zero instantaneously as soon as the time evolution starts. This is sometimes referred to as a *sudden quench* protocol, in contrast with a *slow quench* where the Hamiltonian is continuously changed from \mathcal{H} to \mathcal{H}_i over some finite time span (in Ch. 4 we will study an example of slow quench, in a different system)

We can rewrite the initial state in terms of the eigenbasis of \mathcal{H} as $|\psi_i\rangle = \sum_\alpha c_\alpha |\alpha\rangle$, where the coefficients c_α must satisfy $\sum_\alpha |c_\alpha|^2 = 1$ to ensure the normalization. The system, at a certain time t will be in the state (we set from now on $\hbar = 1$):

$$|\psi(t)\rangle = e^{-iHt} |\psi_i\rangle = \sum_\alpha e^{-iE_\alpha t} c_\alpha |\alpha\rangle \quad (2.1)$$

and the time-dependent expectation value of the observable \hat{A} will evolve as:

$$\langle \hat{A}(t) \rangle = \langle \psi(t) | \hat{A} | \psi(t) \rangle = \sum_\alpha |c_\alpha|^2 A_{\alpha,\alpha} + \sum_{\alpha \neq \beta} c_\alpha^* c_\beta e^{i(E_\alpha - E_\beta)t} A_{\alpha,\beta} \quad (2.2)$$

The long-time average of $\langle \hat{A}(t) \rangle$ is, in the case of non-degeneracy of the energy eigenvalues [106], equal to:

$$\overline{\langle \hat{A}(t) \rangle} = \sum_\alpha |c_\alpha|^2 A_{\alpha,\alpha} . \quad (2.3)$$

This result for the time average of the observable \hat{A} is referred to as the one predicted by the *diagonal ensemble* [9, 12, 107, 108]. It must be pointed out that the diagonal ensemble is strongly dependent on the initial state, namely, on the expansion coefficients c_α .

The energy of the system \overline{E} and its uncertainty ΔE can be calculated as:

$$\overline{E} = \sum_\alpha |c_\alpha|^2 E_\alpha \quad \Delta E = \sqrt{\sum_\alpha |c_\alpha|^2 (\overline{E} - E_\alpha)^2} \quad (2.4)$$

We will assume that $\Delta E / \overline{E} \sim N^{-1/2}$ as it is the case for a sudden quench [11], therefore the sum in equation (2.3) mainly sums terms in the energy window $\overline{E} \pm \Delta E/2$, that we populated with the quench.

The ETH asserts that *the diagonal terms* $A_{\alpha,\alpha} = \langle \alpha | \hat{A} | \alpha \rangle$ are almost constant varying α (up to correction exponentially small in the number of

particles N) and that the off-diagonal terms $A_{\alpha,\beta} = \langle \alpha | \hat{A} | \beta \rangle$ are exponentially small in N .

When the ETH holds, all the coefficient $A_{\alpha,\alpha}$ in the right-end side of equation (2.3) are almost constant, and the long-time average expectation value of \hat{A} is then equivalent to its microcanonical average in the same energy window $\bar{E} \pm \Delta E/2$, where all the energy eigenstates are weighted equally.

$$\overline{\langle \hat{A}(t) \rangle} = \langle \hat{A} \rangle_{MC} \quad (2.5)$$

The ETH can thus be viewed as the equivalence between the diagonal and the microcanonical ensemble. The latter depends only on the energy and, in contrast with the diagonal ensemble, it is completely independent of the initial state $|\psi_i\rangle$. We can say that, when ETH holds, the system will reach an equilibrium thermal state that is the one predicted by the microcanonical ensemble, losing memory of the initial conditions, except for the information about global conserved quantities such as particle number or energy. More precisely all the details of the initial state are inaccessible to local measures and remains hidden in the system.

It must be noticed that, since the $A_{\alpha,\alpha}$ are almost constant in energy, the ETH implies that the expectation value of the observable \hat{A} in a single energy eigenstate is equal to the value predicted by a microcanonical ensemble constructed at the same energy scale.

A typical measure of the entanglement between two subsystems is the von Neumann entropy. If we partition it into a subsystem A and its ‘environment’ B , with $B \gg A$, for a given eigenstate $|\alpha\rangle$, we can calculate the reduced density matrix of A tracing out the degrees of freedom of B .

$$\rho_A^\alpha = \text{Tr}_B |\alpha\rangle \langle \alpha| \quad (2.6)$$

Then the von Neumann entropy (or entanglement entropy) of the bipartition for the eigenstate $|\alpha\rangle$ is defined as

$$S_A = -\text{Tr}_A (\rho_A^\alpha \log_2 \rho_A^\alpha) \quad (2.7)$$

For an eigenstates that fulfill the ETH, the von Neumann entanglement entropy of the region A coincides with the thermal entropy, which is extensive with respect to the system size L [19, 109–111], i.e. they satisfy a *volume-law* for the entanglement entropy.

Many-body eigenstates of a localized system do not obey the ETH. In particular they do not show a volume law for the entanglement entropy,

that grows instead linearly with the size of the boundary between the two subsystems; and for a one-dimensional localized system, it remain constant [18, 26]. Such an *area-law* scaling for the entanglement entropy in the excited states at finite energy is a signature of the MBL and has been the subject of several studies [18, 19, 23, 26, 109–118].

Also the standard deviation of the sample-to-sample fluctuations σ_S of the entanglement entropy (i.e. induced by averaging over different disorder realizations) displays a peculiar behavior at the transition between the two different regimes. In the ETH phase the entanglement entropy depends only on the energy, and its standard deviation goes to zero in thermodynamic limit, whereas in the MBL regime the area-law for the entanglement entropy leads to a constant σ_S [26, 27, 119–121]. At the transition the variance is expected to diverge with the size of the system, because a small variation in the disorder realization introduces a change in the energy of the system that can lead both to localized and ergodic states.

In the same spirit of the entanglement entropy, the particle-number fluctuations of a subsystem are supposed to display a change from a volume-law to an area-law upon crossing the ETH/MBL transition [26, 27, 121].

The spreading of the entanglement after a sudden quench is another key feature for discerning between MBL and other regimes. For integrable system it as been shown that the entanglement entropy of a subsystem $S_l(t)$ of size l , grows linearly in time, as $S_l(t) \sim t$ [83, 122], before saturating to a constant proportional to the system size. This is due to finite velocity of the excitations that are created following the quench. These excitations are carried by couples of quasiparticles moving with opposite momenta and opposite finite group velocities. If we now divide the system in two halves, the rate of quasiparticles that cross the boundary between the two subsystems is constant and, as a consequence, the entanglement entropy between the two regions grows linearly in time. This prediction has been also confirmed for non-integrable system [123] where, although the energy transport is diffusive the entanglement entropy spreads ballistically. This is contrast with what has been proved for the MBL phase where, if the initial state before the quench is non-entangled (i.e. a product state), the entanglement grows logarithmically in time, as $S_l(t) \sim \log(t)$ [34, 124]. This effect can be explained by a dephasing mechanism due to interactions between localized particles [114, 115, 125] Some recent works [126, 127] have also revealed the presence of an intermediate delocalized regime where the entanglement has a sub-ballistic growth law, $S_l(t) \sim t^{1/z}$ were the dynamical exponent z diverges when approaching the transition to the MBL phase.

The knowledge we have about the MBL is increasing constantly, but a complete theory is still far from being constructed and several open questions remain. One of those revolves around the issue of whether MBL can

occur also in translationally invariant system, i.e. in the absence of any kind of disorder, assuming that the randomness in the initial state of the system would be enough to localize the system. This is a strongly debated question and many related types of models have been considered [128–131].

Another important open question is about the nature of the localization/delocalization transition, and the possible breaking of ergodicity in the delocalized regime close to the transition [25, 132–134].

2.2 Hamiltonian and ground-state properties

We consider now the natural extension of the Aubry-André model (1.1) to interactions: a one-dimensional model of spinless interacting fermions moving in a quasiperiodic potential.

This model has been recently studied in many works [135–143] from both a static and dynamic point of view. In particular in [143] a first attempt of studying the ground-state phase diagram was reported. Related models (as, for example, interacting bosons in a quasiperiodic potential or interacting fermions in a pure random potential) has been theoretically studied in the last years [23, 27, 28, 34, 99, 127, 142, 144–151]. Recently MBL has been experimentally observed in a one-dimensional system of ultra-cold interacting fermions with spin in a quasiperiodic disordered lattice potential [30].

The Hamiltonian of the model, for a chain with L sites and open boundary conditions, is defined in the following way:

$$\mathcal{H}^{int} = \sum_{i=1}^{L-1} \left[-j \left(c_i^\dagger c_{i+1} + c_{i+1}^\dagger c_i \right) + V n_i n_{i+1} \right] + \sum_{i=1}^L h_i n_i \quad (2.8)$$

$$h_i = \Delta \cos(2\pi(\alpha i + \phi)) \quad (2.9)$$

We use here the same notation of (1.1), with the addition of the interaction term which intensity is ruled by V . We will set from now on $j = 1$. In contrast to Ch. 1, we take a different choice for the incommensurate wave number setting $\alpha = 532/738 \approx 0.721$ as implemented in a recent experimental setup[30].

Since the Hamiltonian (2.8) commutes with the total number of particle N_{tot}

$$N_{tot} = \sum_{i=1}^L n_i \quad [\mathcal{H}^{int}, N_{tot}] = 0 \quad (2.10)$$

in the following we will restrict our attention to the half filling sector $n = N_{tot}/L = 0.5$ of the Hamiltonian.

The Hamiltonian (2.8) is not exactly solvable because of the presence of

both the quartic interaction term and the quasiperiodic potential. We will then start the analysis of the ground-state properties of the model from the two limits $V = 0$ and $\Delta = 0$ where exact results are available.

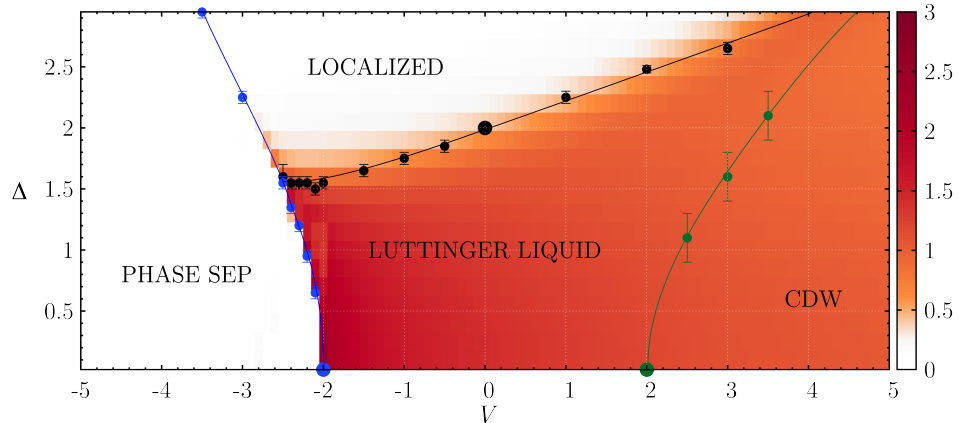


Figure 2.1: Ground state phase diagram of the model. The contour plot shows the behavior of the half-chain entanglement entropy $S_{L/2}$ for a single realization of the disorder of a chain with $L = 72$ sites. Data obtained from both DMRG (contour plot) and QMC simulation (dots with error bars) are in good agreement except for both the PS-LOC and the LL-CDW transitions that are not captured by the entanglement entropy.

In the noninteracting case (vertical axis at $V = 0$ in Fig. 2.1) the Hamiltonian (2.8) reduces to the Aubry-André model (1.1). As discussed in the previous Ch. 1, for $\Delta = 2$ this model has an energy independent transition from and extended to a *localized phase* (LOC) (big black dot in Fig. 2.1). Above this value all the eigenstates of the Hamiltonian are localized, with a localization length $l_{loc} = 1/\log(\Delta/2)$.

In the opposite limit where the quasiperiodic potential is set to zero, the resulting model of interacting fermions can be mapped on a spin $1/2$ XXZ [152, 153] model by a Jordan Wigner transformation [80]. This model is integrable via Bethe Ansatz [153] and its ground-state phase diagram, corresponding in Fig. 2.1 to the $\Delta = 0$ axis, is composed by two gapped phases for $|V| \geq 2$ separated by a gapless critical phase in the middle for $|V| \leq 2$. In the language of fermions the two gapped phases corresponds to a *phase separation* (PS) for attractive interactions where particles in the classical limit $V \rightarrow \infty$ segregates on one half of the chain. In the other gapped regime where the interaction is repulsive, particles tends to maximize their distance crystallizing in a *charge density wave* (CDW). In the gapless phase particles are delocalized and the long-wavelength properties of this phase are described by a Luttinger liquid theory (LL) with correlation functions that decay as a power law, in contrast with the two other regimes where

they exhibit and exponential decay.

As we commented before, the Hamiltonian (2.8) is not exactly solvable and we thus studied numerically the ground-state phase diagram away from the two axes $\Delta = 0$ and $V = 0$. We performed numerical simulations using two different methods: the Density Matrix Renormalization Group (DMRG) [154–158] and the Quantum Monte Carlo (QMC) [159]. The main results obtained with both methods are collected in Fig. 2.1. In order to perform the QMC simulation and avoid the sign problem, we exploit the correspondence between bosons in the hard core regime, where double occupations are highly suppressed, and fermions. We therefore perform the QMC simulation on the equivalent bosonic Hamiltonian of (2.8), with strong repulsive on-site interaction varying the interaction between nearest neighbors [99, 145] and we study the changing in the asymptotic decaying of the correlation $g_1(r) = \langle b_0^\dagger b_r \rangle$ where b_i^\dagger, b_j are the bosonic creation and annihilation operators. This correlation function decays exponentially in all the phases of the system (LOC, PS, CDW), with the exception of the LL regime where it shows a power-law decay. Through this change in the asymptotic behavior of the $g_1(r)$ we can therefore estimate all the transitions in phase diagram except the PS-LOC transition where in both the regimes the $g_1(r)$ function exponentially decaying. In this case we locate the transition by observing the appearance of droplets in the density profile of the ground-state.

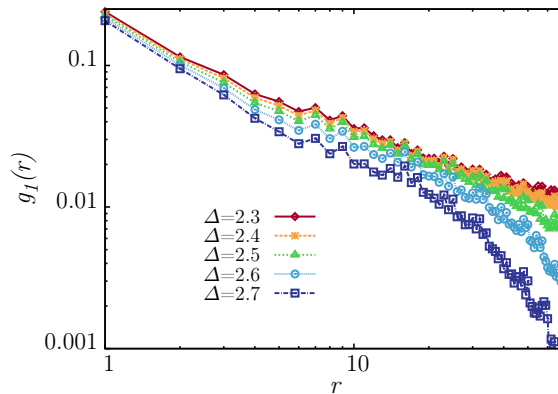


Figure 2.2: Behavior of the correlation $g_1(r)$ as a function of the distance r for $V=2$ and various values of the quasiperiodic strength Δ on a chain with $L = 160$ sites. For $\Delta=2.5$ we can observe a transition between power law to exponential in the long distance decaying.

In Fig. 2.2 we show the results obtained from a single realization of the disorder in a chain with $L = 160$ sites for $V = 2$ as a function of the disorder strength Δ . Both for QMC and for the DMRG simulations, we do not perform a proper disorder-averaging and we assume that the system sizes are

we can reach are big enough to determinate a self-averaging in the observable we study.

Given that periodic boundary conditions are used in the QMC calculation, the $g_1(r)$ function is averaged over all the translation of the reference site along the chain.

The change in the decaying behavior from exponential to power law is evident, and allows us to locate the transition from an extended to a localized regime at the critical value of the quasiperiodic potential $\Delta = 2.5 \pm 0.1$. We performed the same analysis to reconstruct the boundary between the LL and the LOC regime as well as the boundaries for the LL-CDW and PS-LL transitions (respectively black, green and blue line in Fig. 2.1). We also analyzed the half-chain entanglement entropy of the ground-state, as defined in (2.7).

Data for entanglement entropy in Fig. 2.1 are obtained performing DMRG simulation from a single realization of the disorder on chain with $L = 72$ sites. In the LOC and in the PS regimes the entanglement entropy is strongly suppressed since both the regimes are dominated by the diagonal part of the Hamiltonian and the corresponding ground state is closed to a Fock state when $V, \Delta \gg 1$. In the LL regime, where particles are delocalized the entropy is enhanced and, on the half chain, it is expected to diverge as $S(L/2) \sim \log_2(L/2)$. In the CDW phase the ground-state is a linear combination of the two states composed by alternating void and occupied sites and the entanglement entropy of any bipartition is therefore $\log_2(2) = 1$ for $V \gg 1$. While the transitions between LL and LOC phases and between LL and PS regime are clearly marked by the entanglement, it is not possible to observe the PS to LOC and the LL to CDW wave transition using only the entanglement entropy since in both side in the first case both phases are weakly entangled while in the second case the logarithmic growth of entanglement in the LL makes our system size insufficient to observe a drastic change.

We will now derive another feature of the Hamiltonian that allows us to relate its properties for different values of the parameters.

The most excited state of \mathcal{H} is the ground state of $-\mathcal{H}$. The canonical gauge transformation (GT) $c_i \rightarrow (-1)^i c_i$ allows us to change the sign of the hopping term $j \rightarrow -j$ freely. Moreover, on average over the phase (PA) ϕ the sign of Δ becomes arbitrary.

$$\begin{aligned} \mathcal{H}^{int}(j, V, \Delta) = \\ -\mathcal{H}^{int}(-j, -V, -\Delta) \xrightarrow{GT} -\mathcal{H}^{int}(j, -V, -\Delta) \xrightarrow{PA} -\mathcal{H}^{int}(j, -V, \Delta) \end{aligned} \quad (2.11)$$

We can therefore identify the most excited state of $\mathcal{H}^{int}(j, V, \Delta)$ with the ground state of $\mathcal{H}^{int}(j, -V, \Delta)$, and the phase diagram we reconstruct for both positive and negative V informs us on the behavior of the ground state as well as the most excited state of the Hamiltonian. This relation suggests

us the first step for studying the localization properties of excited states. We focus now on the two lines $V = \pm 2$ of the phase diagram. As already discussed, we estimated the transition in the ground-state for $V = 2$ at the critical value of the disorder strength

$$\Delta_c^{GS}(V = 2) = 2.5 \pm 0.1 \quad (2.12)$$

that is in good agreement with the results we obtained via DMRG simulation for the half-chain entanglement entropy. In the same spirit we obtain the critical value of the disorder for $V = -2$ corresponding to the critical value for the most excited state of $\mathcal{H}^{int}(t, V, \Delta)$:

$$\Delta_c^{Emax}(V = 2) \equiv \Delta_c^{GS}(V = -2) = 1.5 \pm 0.1 \quad (2.13)$$

The localization transition for $V = 2$ takes therefore place at two different critical values of the disorder in the ground-state and in the most excited state. This asymmetry alone already suggests that for $1.5 \leq \Delta \leq 2.5$ there should be a transition in energy between localized and extended states in the spectrum, i.e. a many-body mobility edge (MBME).

2.3 Properties of the spectrum

The mobility edge is a really particular transition that takes place between localized and extended regions of the spectrum at a finite energy [26, 120, 121, 142, 160]. In order to detect this transition it is necessary to analyze the properties of all the excited states of the Hamiltonian. This is a peculiar transition, as it is not expected to lead to visible signatures in the equilibrium thermodynamics of the system, but rather in the out-of-equilibrium dynamics.

In this section we will analyze the properties of the *level statistic*, in sec. 2.3.1, and of the *entanglement entropy*, in sec. 2.3.2, for different slices of the spectrum and we will provide evidence for the existence of a mobility edge in the Hamiltonian (2.8).

2.3.1 Levels statistics

One of the ways to characterize the localization-delocalization transition in the spectrum goes through the study of the spectral statistics of adjacent levels in the many-body Hamiltonian. This idea, stems from random matrix theory [161], it has been introduced to study disordered systems at the single-particle level [162–164] and later exploited extensively to investigate many-body systems [22, 24–26, 121, 138, 148, 165–167].

Oganesyan and Huse [22] where the first to study the level statistics of the energy spectrum in a system of interacting fermions in a random potential. They discovered that the statistics exhibits a crossover between Poissonian distribution of level spacing, and a distribution consistent with the Gaussian orthogonal ensemble of random matrices (also-called Wigner's surmise) [168, 169].

Deep in the localized regime the eigenstates are localized in the many-body Fock space of localized single particle orbitals. Thus for a large enough system, namely in the thermodynamic limit, different states closed in energy have exponentially small overlap in Fock space since they differs by large number of particles rearrangement. The eigenstates then do not interact with each other and do not have any level repulsion and the level statistics is simply Poissonian as in the case of integrable models.

On the other hand, in the fully delocalized regime the level statistics is also described by random matrix theory, namely by the Gaussian orthogonal ensemble (GOE) [170] characterized by level repulsion. What happens exactly at the critical point is still far from being understood but proposals exist for the interpolation between the two regimes [25, 171].

For a specific realization of the disorder, once we know the two limits of the band E_{min} and E_{max} , we rescale every energy levels as follows

$$0 \leq \epsilon_n \equiv \frac{E_n - E_{min}}{E_{max} - E_{min}} \leq 1 \quad (2.14)$$

This allows us to compare different disorder realizations, since E_{min} and E_{max} are in general dependent on the phase of the quasiperiodic potential. After sorting the spectrum in ascending order, we define then the adjacent energy gap δ_n as the difference between two adjacent eigenstates

$$\delta_n = \epsilon_n - \epsilon_{n-1} \quad \delta_n \geq 0 \quad (2.15)$$

The adjacent gap ratio is then defined as follows

$$r_n = \frac{\min(\delta_n, \delta_{n+1})}{\max(\delta_n, \delta_{n+1})} \quad 0 \leq r_n \leq 1 \quad (2.16)$$

For localized spectrum, the Poisson probability distribution $P_{Poiiss.}(r)$ and its mean value $\langle r_n \rangle_{Poiiss.}$ are then

$$P_{Poiiss.}(r) = \frac{2}{(1+r)^2} \quad \langle r_n \rangle_{Poiiss.} = 2 \ln 2 - 1 \cong 0.386 \quad (2.17)$$

In the opposite regime, the mean value of the distribution $\langle r_n \rangle_{GOE}$ can be

calculated numerically using large GOE random matrices [22, 26]

$$\langle r_n \rangle_{GOE} = 0.5295 \pm 0.0006 \quad (2.18)$$

To each energy level ϵ_n (except the first and the last one) thus corresponds an adjacent gap ratio r_n that depends not only on the index n but also on the size of system L , on the particular realization of the potential given by the phase ϕ and on the strength of the quasiperiodic potential Δ . Average over the phase of the quasiperiodic potential and over finite windows of the energy spectrum allows to minimize finite-size effects and to have sufficient statistic at any given energy. For a certain value of the energy ϵ we consider the set $\{\epsilon_n\}_\epsilon$ composed by the energy levels belonging to the interval $\epsilon \pm 0.05$. We then first average the adjacent gap ratio over this energy window, and after that over different realizations of the quasiperiodic potential.

$$\langle r_n(\phi, \Delta) \rangle_\epsilon = r_\epsilon(\phi, \Delta) \quad \langle r_\epsilon(\phi, \Delta) \rangle_\phi = r_\epsilon(\Delta) \equiv r(\epsilon, \Delta) \quad (2.19)$$

Since the tails of the spectrum display a very low density of states, we limit our attention to the energy window $\epsilon \in [0.1, 0.9]$. The above procedure gives us in the end an energy-resolved adjacent gap ratio $r(\epsilon, \Delta)$ that, for a fixed chain length L , depends only on ϵ and Δ .

The method we just introduced requires the full diagonalization of the Hamiltonian, i.e. of a matrix that grows exponentially in the system size. For a model of spinless fermions in a chain of L sites, i.e. for the Hamiltonian (2.8), the dimension of the subspace with N particles is the binomial coefficient $\binom{L}{N}$. The level statistics analysis has been so far applied to the full spectrum in chains at half filling, $N = L/2$, with sizes up to 18 sites in two-leg ladder [121], or even 22 sites [26] but limiting the diagonalization to some slices of the spectrum [172]. Since the available sizes are really small, a finite-size scaling analysis is absolutely necessary to identify the transition. We analyzed the level spectroscopy in the model (2.8) setting $V=2$ and varying Δ in the window $\Delta \in [1, 5]$ for different system sizes $L = 11, 12, 13, 14, 15$. We average first over the full spectrum Fig. 2.3a and then over different slices $\epsilon = \epsilon^* \pm 0.05$ Fig. 2.4a/b. The results we show are obtained by averaging over 1200, 600, 400, 300, 200 different realizations of the potential for $L = 11 \dots 15$ respectively. Since it is not possible to keep the density of particle constant to half filling for both even and odd system sizes L , we consider $n = N/L = 1/2$ for even L , and $N = L/2 - 1$ for odd L . To every values of $r(\epsilon, \Delta)$ we associate a statistical uncertainty δr originating from by the disorder averaging over R different realizations, that is equal to

$$\delta r = \pm \sqrt{\frac{\langle r(\epsilon, \Delta)^2 \rangle - \langle r(\epsilon, \Delta) \rangle^2}{R - 1}} \quad (2.20)$$

When error bars are not shown in Fig. 2.3a and in Fig. 2.4, they are smaller than the size of the symbol used in the plot.

A further aspect we want to stress out are the boundary conditions we used in the simulation. We initially performed simulations imposing open boundary conditions as in the Hamiltonian (2.8), but we immediately noticed that such boundary conditions lead to too strong finite-size effects. We then turned to “*mixed boundary condition*”, i.e. we closed the link between the last and the first site of the chain adding the term $-t(c_L^\dagger c_1 + c_1^\dagger c_L) + V n_1 n_L$ to the Hamiltonian and leaving unchanged the chemical potential. We notice that, due to the incommensurability between the quasiperiodic potential and the chain length, the potential has an artificial jump between site 1 and L . This aspect could be fixed by seeking rational approximations of α in the form p/L with p integer, but this in turn leads to very regular potential (due to the small values of L) which are very far from the original one.

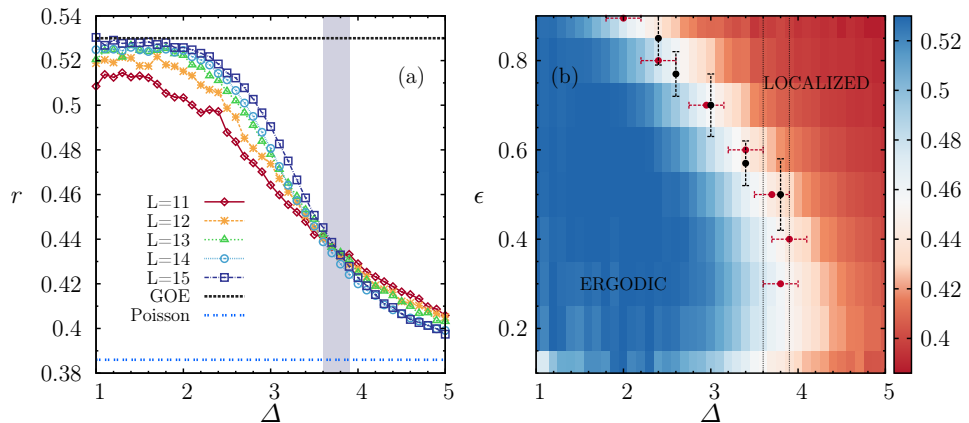


Figure 2.3: Panel (a): Scaling of the adjacent gap ratio averaged over the whole spectrum as a function of quasiperiodic potential strength Δ at the point $V = 2$ for different sizes $L = 11, 12, 13, 14, 15$. The value of Δ where the whole spectrum is localized is estimated $\Delta_{FL} = 3.75 \pm 0.15$. Panel (b): Contour plot of the energy-resolved adjacent gap ratio as a function of energy ϵ and intensity of the quasiperiodic potential Δ for $L = 15$. Black and red symbols shows the value (with error bars) for the MBL transition obtained from finite-size scaling 2.4. The region between the two vertical dotted lines shows the transition to a full localized spectrum.

Fig. 2.3a shows the adjacent gap ratio as a function of the quasiperiodic potential Δ strength for different sizes, averaged over the whole spectrum. Here we can see that in both cases for low and large enough Δ we recover an average $\langle r \rangle$ compatible with Poissonian and GOE statistics respectively. The crossover between the two limits becomes more and more sharp upon

increasing the system size, and we can estimate the critical value of Δ looking at the crossing between the lines corresponding to different L (shaded area in the plot). We can then estimate that the whole spectrum becomes localized for $\Delta \geq 3.75 \pm 0.15$ as shown in Fig. 2.3b.

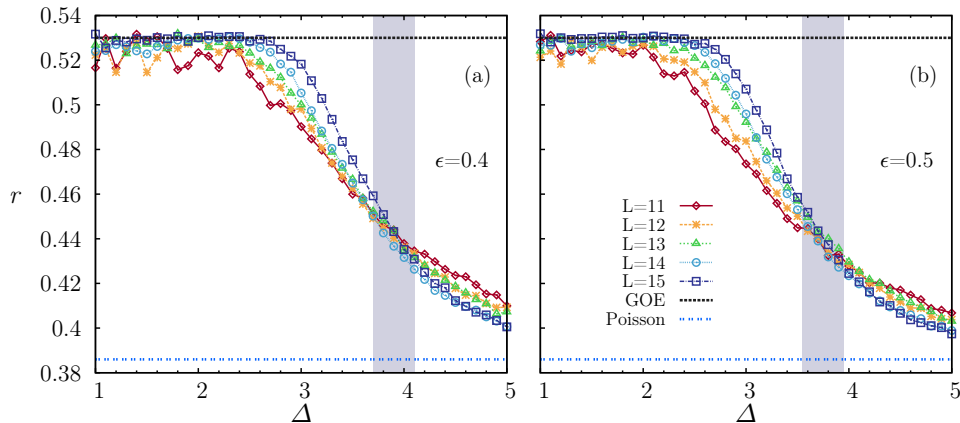


Figure 2.4: Scaling of the adjacent gap ratio of the energy-resolved adjacent gap ratio as a function of the quasiperiodic potential Δ strength at the point $V = 2$ for different sizes $L = 11, 12, 13, 14, 15$ at the energy $\epsilon = 0.4$ in panel (a) and $\epsilon = 0.5$ in panel (b). The critical values of Δ where occurs the MBL transition, (shaded area in the plots), are reported in Fig. 2.3.

We then move to the analysis of the energy-resolved adjacent gap ratio $r(\epsilon, \Delta)$, keeping ϵ fixed and changing Δ to obtain the critical value $\Delta_c(\epsilon)$ (black symbols in Fig. 2.3 b). In Fig. 2.4 we show the results as a function of Δ in the two energy windows ($\epsilon \in 0.4 \pm 0.05$) in panel (a) and ($\epsilon \in 0.5 \pm 0.05$) in panel (b) and the two critical values of $\Delta^{crit}(\epsilon)$ that we extrapolated (shaded area in the plots). We performed the same analysis for different values of ϵ (upon varying Δ) as well as by varying ϵ at fixed Δ , leading to the estimates of the ergodic/localizes boundary, shown in Fig. 2.3b as red and black dots respectively.

2.3.2 Entropy and fluctuations

Another tool that allows us to study the spectrum is the entanglement between two partitions of the system. This quantity shows completely different behaviors in the ergodic and localized regimes and it is therefore a good indicator for detecting the MBL transition [18, 19, 23, 26, 109–118].

In the same spirit of section 2.3.1 we want to perform spectral and disorder averaging on S_A^n , defined in (2.7), for obtaining a good indicator of the transition. For a particular realization of the quasiperiodic potential and for a given every energy ϵ we consider all the energy level $\{\epsilon_n\}_\epsilon$ in the interval

$\epsilon \pm 0.05$, we then define an *average entanglement entropy* over these states. We finally average over different realizations of the disorder, obtaining the *energy resolved entropy* $S_A(\epsilon)$.

$$\langle S_A^n(\phi, \Delta) \rangle_{\{\epsilon_n\}_\epsilon} = S_A(\epsilon, \phi) \quad S_A(\epsilon) = \langle S_A(\epsilon, \phi) \rangle_\phi \quad (2.21)$$

We also calculate the standard deviation of the sample-to-sample fluctuations $\sigma_{S_A}(\epsilon)$ of the entanglement entropy [26, 27, 119–121]

$$\sigma_{S_A}(\epsilon) = \sqrt{\langle S_A(\epsilon)^2 \rangle_\phi - \langle S_A(\epsilon) \rangle_\phi^2} \quad (2.22)$$

Recalling the discussion in Sec. 2.1, for sufficiently low disorder in the extended regime all the excited states follow the Eigenstate Thermalization Hypothesis, and their reduced density matrices are equivalent to thermal density matrices of a system at high temperature. The entanglement entropy is therefore extensive and exhibits a *volume-law* scaling

$$\text{1D systems, Extended Phase} \quad \rightarrow \quad S \propto \alpha_s L \quad (2.23)$$

Moreover for a system that fulfills the ETH the entropy depends only on the energy, giving a $\sigma_{S_A}(\epsilon)$ that goes to zero in thermodynamic limit. The volume-law for highly excited states has been observed both for weakly disordered systems [26, 120] and for completely non random ones [173–175]. In the opposite limit, in the insulating phase, the many-body eigenstates are localized and well approximated by product states since they have small entanglement. The entanglement entropy of a subsystem thus scales as the surface area of the bipartition satisfying a so-called *area-law*. In the localized regime the area-law is valid not only for the ground-state but also for all the excited states.

$$\text{1D systems, Localized Phase} \quad \rightarrow \quad S \propto \text{const.} \quad (2.24)$$

This change in the scaling from area to volume-law allows us for detecting accurately the MBL phase transition.

The entropy has thus almost no fluctuations reflecting in a vanishing $\sigma_{S_A}(\epsilon)$ in the limit of large disorder as in the case of the ergodic regime. At the transition the entropy is strongly dependent on the disorder realization since a small variation in the phase of the quasiperiodic potential introduces a variation in energy and can lead to both a localized or an ergodic state. This strong fluctuations in the entropy for different disorder realization leads to a divergence of the $\sigma_{S_A}(\epsilon)$ upon increasing the size of the system at the MBL transition [120].

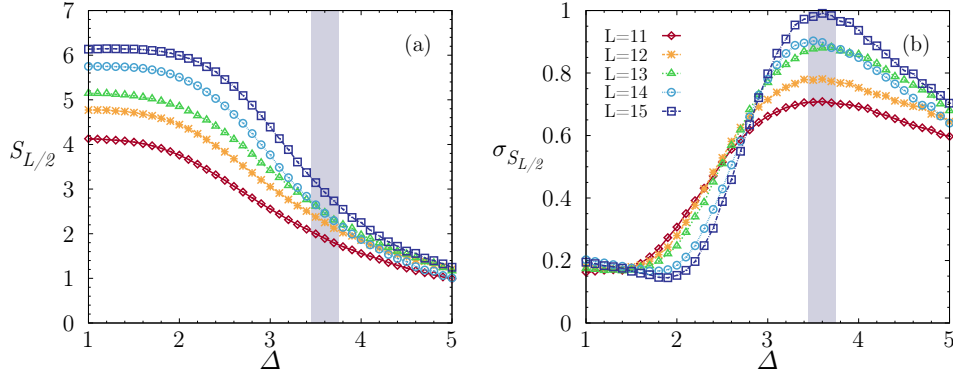


Figure 2.5: Entanglement entropy (a) and its standard deviation (b) as a function of the quasiperiodic potential Δ . Data are averaged in the energy window $\epsilon = 0.5 \pm 0.05$ and over the disorder ensemble. The MBL transition, the grey shade, is obtained by the maximum of the standard deviation of the entanglement entropy.

The results we show in Fig. 2.5 and Fig. 2.6 are obtained from the same set of simulations we analyzed in section 2.3.1. For even length of the chain we bipartite the system in two halves containing $L/2$ sites each, while for odd lengths the two partitions differ by one site (in the plots we will use the label $S_{L/2}$ also for chains the odd length). Again, as in section 2.3.1, since the tails of the spectrum have really low density of states, we restrict our in analysis in the energy interval $\epsilon \in [0.1, 0.9]$.

In Fig. 2.5a we show the numerical results for the entanglement entropy and its standard deviation as a function of the quasiperiodic potential Δ in the energy window $\epsilon = 0.5 \pm 0.05$. We see that the crossover from volume-law to area-law is clear. For weak disorder, i.e. in the thermal phase, we fit data with a volume-law scaling for the entanglement entropy finding a perfect agreement with previous literature [120].

$$S_{L/2}^{Th} \propto \alpha_S^{Th} \frac{L}{2} \quad \rightarrow \quad \alpha_S^{Th} = 1 \pm 0.01 \quad (2.25)$$

In the opposite regime for high disorder the entanglement entropy is almost insensitive to the system size, respecting the predicted area-law for the localized phase. The MBL transition is emphasized by the behavior of the standard deviation $\sigma_{S_{L/2}}$, in Fig. 2.5b, that shows a peak near $\Delta = 3.6$ that becoming sharper with increasing system size. We estimate the critical value of Δ where the MBL transition occurs, as shown in Fig. 2.5b and in Fig. 2.7, with the maximum of the $\sigma_{S_{L/2}}$.

We performed the same analysis for different energies (black symbols in Fig. 2.6b) and also keeping Δ fixed as a function of ϵ for obtaining the criti-

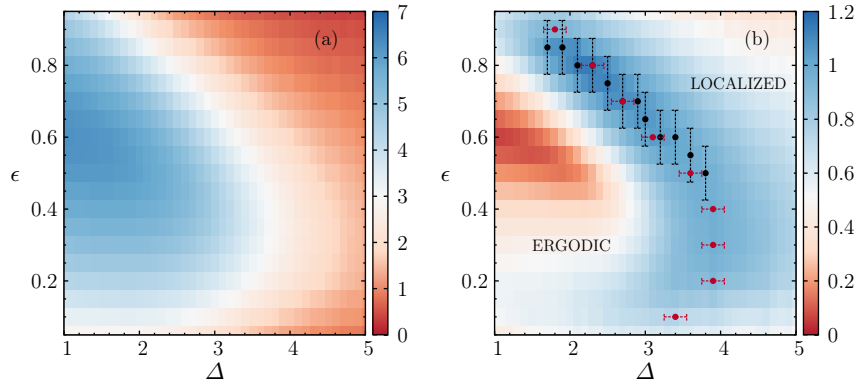


Figure 2.6: Contour plot of entanglement entropy **(a)** and its standard deviation **(b)** as a function of the quasiperiodic potential Δ and of the energy ϵ . Data are averaged in the energy window $\epsilon = \epsilon^* \pm 0.05$ and over the disorder ensemble. In panel **(b)** black and red symbols show the value (with error bars) for the MBL transition obtained from the maximum of the standard deviation of entropy Fig. 2.5.

cal value $\epsilon_c(\Delta)$ (red symbols in Fig. 2.6b). All the results obtained from the study of entanglement entropy are collected in Fig. 2.6b.

2.3.3 Evidences for mobility edge

We collect in Fig. 2.7 all the results of two previous sections where we studied the behavior of the level statistics (sec. 2.3.1) and entanglement (sec. 2.3.2).

The results obtained with the two indicators are well consistent within the error bars, and they clearly point towards the existence of a MBL transition between an ergodic extended regime and a localized one. This transition takes place at different values of the disorder for different values of the energy leading to a MBME (red line in Fig. 2.7). The critical values of the parameters where the transition occurs in the excited states are also consistent with the critical values found for the ground-state of $\mathcal{H}(V=2)$ and $\mathcal{H}(V=-2)$ $\Delta = 2.5 \pm 0.1$ and $\Delta = 1.5 \pm 0.1$, respectively, as it can be seen from the extrapolation done in Fig. 2.7.

In particular for purposes that will become clear in the next section, we focus on the case $\Delta = 2.5$ and $V = 2$, for which we identify the MBME to occur in the interval

$$0.72 \leq \epsilon^{ME}(\Delta=2.5) \leq 0.85 \quad (2.26)$$

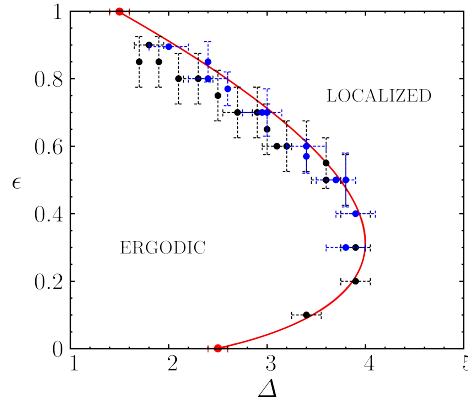


Figure 2.7: Spectral phase diagram for $V=2$. Blue and black symbols shows (with error bars) the critical values estimated via level statistics (Fig. 2.3, Fig. 2.4) and entanglement entropy (Fig. 2.5, Fig. 2.6) respectively. The line in red, interpolating the two transition in the groundstate of $H(V=2)$ and $H(V=-2)$ 2.1, is a guide to the eyes for the energy dependent MBL mobility edge from ergodic to localized regimes.

2.4 Mobility-edge spectroscopy via quench

The MBME can be observed studying the time evolution of a system driven out of equilibrium by a local (or global) quench. Let's say we prepare our system in the ground-state of the Hamiltonian \mathcal{H}_i and that we will then evolve it with a different Hamiltonian \mathcal{H}_f . The initial state is not, in general, an exact eigenstate of the final Hamiltonian and its time evolution will involve many excited states in some energy window that depends on the parameters of \mathcal{H}_i and \mathcal{H}_f . As we will show in this section, growing the quenching amplitude we can control the energy of the excited state of \mathcal{H}_f . Since the mobility edge separates ergodic and localized regions of the spectrum at a finite energy, the protocol we will propose can be a good candidate for detecting dynamically the transition. Moreover, this protocol is easily implementable in an experimental setup of ultracold-atoms [92, 94], and can, in principle, lead to the direct observation of the many-mobility edge.

2.4.1 Quench energy

Our quench protocol starts by preparing the system in the ground-state $|\psi_0^i\rangle$ of the Hamiltonian (2.8) for a particular choice of the parameters $\mathcal{H}_i \equiv \mathcal{H}^{int}(\phi, \Delta_i, V)$.

$$\mathcal{H}_i |\psi_0^i\rangle = E_{0,\phi}^i |\psi_0^i\rangle \quad (2.27)$$

From now on we will write the expectation value of some operator \mathcal{O} on the ground-state of the initial Hamiltonian $|\psi_0^i\rangle$ as:

$$\langle \psi_0^i | \mathcal{O} | \psi_0^i \rangle = \langle \mathcal{O} \rangle_0 \quad (2.28)$$

and quantities with the subscript A_ϕ as calculated for a particular realization of the quasiperiodic potential, i.e. not averaged over the phase.

We then proceed with our protocol performing the *quench*, i.e. evolving the state $|\psi_0^i\rangle$ with the Hamiltonian $\mathcal{H}_f \equiv \mathcal{H}^{int}(\phi, \Delta_f, V)$ obtained from (2.8) by another different choice of the parameters.

$$|\psi(t)\rangle = e^{-it\mathcal{H}_f} |\psi_0^i\rangle . \quad (2.29)$$

We also define the ground-state energy $E_{min,\phi}$ and the maximum excited energy E_{max} of the final Hamiltonian \mathcal{H}_f as:

$$E_{min,\phi} = \langle \psi_0^f | \mathcal{H}_f | \psi_0^f \rangle \quad E_{max,\phi} = \langle \psi_{max}^f | \mathcal{H}_f | \psi_{max}^f \rangle \quad (2.30)$$

where $|\psi_0^f\rangle$ is the ground-state and $|\psi_{max}^f\rangle$ is the maximum excited state of the Hamiltonian \mathcal{H}_f . The energy we inject into the system with the quench, and its uncertainty, are then defined as:

$$E_\phi = \langle \mathcal{H}_f \rangle_0 \quad \delta E_\phi = \sqrt{\langle \mathcal{H}_f^2 \rangle_0 - (\langle \mathcal{H}_f \rangle_0)^2} \quad (2.31)$$

In order to compare results obtained by different realizations of the quasiperiodic potential, we rescale the energies in the window $\epsilon \in [0, 1]$ and accordingly its uncertainty

$$0 \leq \epsilon_\phi = \frac{E_\phi - E_{min}}{E_{max} - E_{min}} \leq 1 \quad \delta \epsilon_\phi = \frac{\delta E_\phi}{E_{max} - E_{min}} \quad (2.32)$$

Finally we can average over different realization of the quasiperiodic potential obtaining the final values:

$$\epsilon = \langle \epsilon \rangle_\phi \quad \delta \epsilon = \langle \delta \epsilon \rangle_\phi \quad (2.33)$$

In principle we should consider also the uncertainty that comes from the disorder average. We neglected it since after numerical checks we observe that it is far smaller than the uncertainty $\delta\epsilon$ introduced by the quench.

If we consider a particular quench, let us say from Δ^i to Δ^f , the injected energy and its uncertainty indicates in which energy window $\epsilon(\Delta^i) \in [\epsilon - \delta\epsilon, \epsilon + \delta\epsilon]$ of the final Hamiltonian the dynamics takes place, in the sense that the eigenstates of \mathcal{H}_f in this energy window will have the largest overlap with the initial state and they will give the main contribution on the long-time behavior of the system.

In Fig. 2.8 we estimate numerically ϵ and $\delta\epsilon$ for $\Delta^f = 2.5$ as a function of Δ^i averaging over 1000 disorder realizations. This quantity is almost size-independent and can be considered as intensive once averaged over different realizations of the quasiperiodic potential. The injected energy ϵ vanishes as the quench amplitude $\delta\Delta = \Delta^f - \Delta^i$ approaches zero and increases, up to a maximal value near to unity, increasing $\delta\Delta$ whereas the uncertainty $\delta\epsilon$ is almost constant in a large window of different Δ^i values and, at least in the ETH regime, it should scale like $\sim L^{-1/2}$.

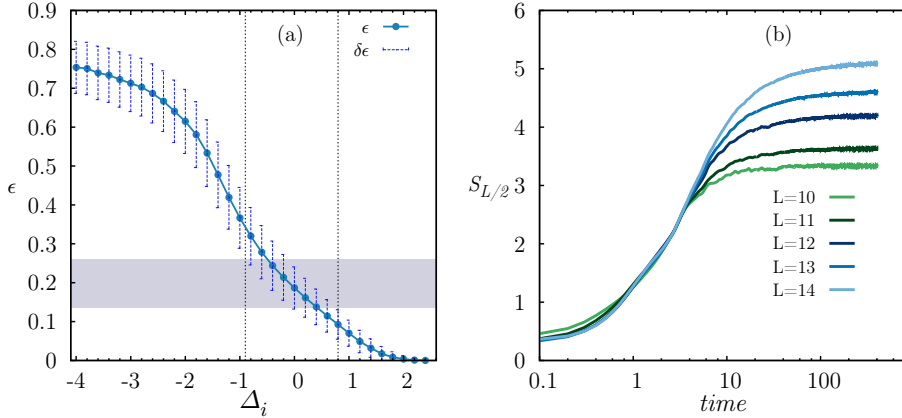


Figure 2.8: Panel (a): energy injected in the system with the quench protocol and its variance as a function of the initial value of the disorder Δ_i . The interaction strength is kept fixed to $V = -2$ and the final disorder is set to $\Delta_f = 2.5$. The gray shadow indicates the value, with uncertainties, where the mobility edge takes place for $V = -2$. Panel (b): time evolution of the entanglement entropy for the quench with $\Delta_i = -2.5$ and different system sizes. Data are averaged over several disorder realizations.

The numerical analysis in Fig. 2.8a thus gives us a relation between the starting point Δ^i of the quench and the energy window in the spectrum centered in $\epsilon(\Delta^i)$ we populated with the quench. We expect that for a certain quench starting point Δ^i the long-time behavior of certain quantities, such as entropy and bipartite density fluctuations, exhibit similar characteristics

of those calculated over the eigenstates in the energy window around $\epsilon(\Delta^i)$.

In particular we can relate the critical energy window $\epsilon^{ME} \in [0.15, 0.28]$, where the mobility edge takes place for $\Delta^f = 2.5$ and $V = -2$, and the amplitude of the quench $\delta\Delta^{ME}$ for which we select that energy window. Specifically we estimate that:

$$\epsilon^{ME} \in [1.5, 2.8] \quad \rightarrow \quad \Delta_i^{ME} \in [-0.5, 0.5] \quad (2.34)$$

2.4.2 Time-dependent Entropy and Density Fluctuations

Using our quench protocol, we study the time evolution of two bipartite quantities: the half-chain entanglement entropy and the bipartite density fluctuations F [26, 27]. The latter is defined as:

$$F = \langle \psi | (\hat{N}_{L/2})^2 | \psi \rangle - \langle \psi | \hat{N}_{L/2} | \psi \rangle^2 \quad \hat{N}_{L/2} = \sum_{i=1}^{L/2} \hat{n}_i \quad (2.35)$$

The bipartite density fluctuations have been studied in recent works in the context of MBL [26, 27, 121, 150, 176]. It has been numerically proved that, crossing the localization transition, their scaling changes from volume to area-law, showing a behavior similar to the entanglement entropy.

In particular Singh et al. [27] studied what happens if we evolve an initial product state with a Hamiltonian whose eigenstates are all extended or with a Hamiltonian with a full localized spectrum (as it could be for (2.8) for $\Delta > 3.75$ and $V = 2$). The long-time values ($t_\infty = 10^{16}$) of both the entanglement and the bipartite density fluctuations show an extensive behavior, when the evolving Hamiltonian is in the extended regime. In the opposite, localized regime the asymptotic entanglement entropy still shows a linear growth with the system size but, with a lower rate, the bipartite density fluctuations do not grow at all. Intuitively these considerations suggest us that, when the evolving Hamiltonian is fully localized, in the long-time dynamics there is still transport of *information*, while the *mass* transport is completely suppressed.

In a similar spirit, we perform several evolutions starting from the ground-state of the Hamiltonian (2.8) and varying the quasiperiodic potential strength in the range $\Delta_i \in [-2.5, 2.25]$, and quenching it to the final value $\Delta_f = 2.5$ while keeping the interaction fixed to $V = -2$.

In Fig. 2.8b we show the results for the time evolution of the entanglement entropy after a quench from $\Delta_i = -2.5$ for different system sizes $L = 11, 12, 13, 14, 15$, until the time $t = 400$ and averaging respectively over

1000, 800, 600, 400, 200 different realizations of the quasiperiodic potential. We observe that, after an initial sub-diffusive regime [126, 127], the entanglement saturates to a finite value $S_{L/2,\infty}$ that, for this specific quench, grows linearly with the system size. We noticed that the bipartite density fluctuations have a similar behavior. Interestingly we also find that, since the ground-state of (2.8) for $\Delta = -2.5$ has a really low entanglement, these results are in good agreement with those obtained in [27].

Here we do not observe any logarithmic growth of the entanglement because the Hamiltonian that rules the time evolution is not completely localized since it has a MBME in the spectrum. For quenches starting from larger values of Δ_i the time evolution of the entanglement entropy is really different from what shown in Fig. 2.8b, since the initial state is characterized by a bigger entropy comparable, in some cases, with its long-time saturation value.

We then analyze the long-time values of the two quantities $S_{L/2}$ and F . Simulations are performed on the same sizes and averaged over the same number of realization of the example in Fig. 2.8b. In the following we will indicate the long-time expectation values A_∞ of some operator A as its expectation value averaged in the time window $\Delta t = [350, 400]$

$$A_\infty \equiv \overline{\langle \psi(t) | A | \psi(t) \rangle}_{\Delta t} \quad (2.36)$$

In Fig. 2.9 and Fig. 2.10 we show the saturation values $S_{L/2,\infty}$ and F_∞ as a function of the initial value of the quasiperiodic potential Δ_i and of the injected energy ϵ .

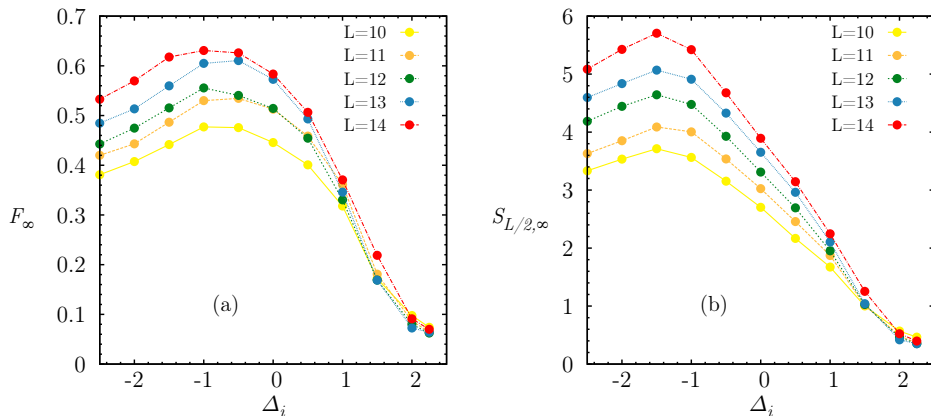


Figure 2.9: The long-time value of the density fluctuation, in panel (a), and of the half-chain entanglement entropy, in panel (b), as a function of Δ_i . Increasing the width of the quench both the quantities move from an intensive to extensive behavior.

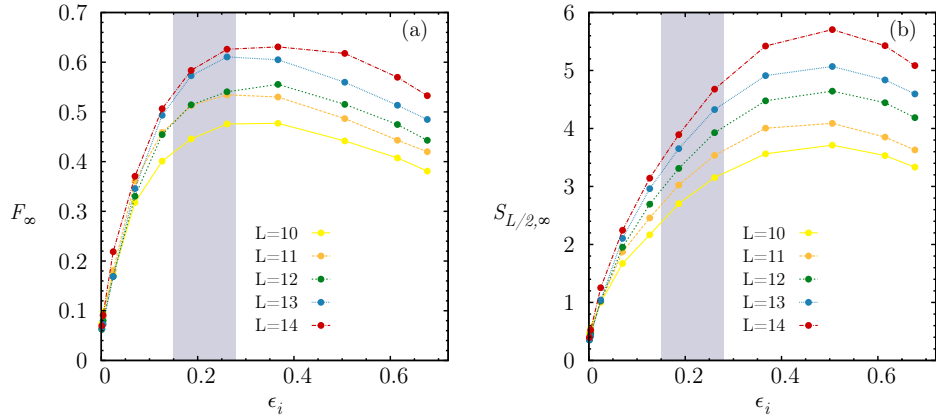


Figure 2.10: The long-time value of the density fluctuation, in panel (a), and of the half-chain entanglement entropy, in panel (b), as a function of ϵ . Exceeding the energy of the mobility edge, the grey shadow, both the quantities move from an intensive to extensive behavior.

We can observe that the behavior of both quantities is really peculiar, and that it changes quantitatively upon varying the quench amplitude. In fact for small values of $\Delta_f - \Delta_i$ both the entropy and the density fluctuations are almost independent of the system size L . This is contrast with the opposite large-quench regime where, for larger $\Delta_f - \Delta_i$, both the $S_{L/2, \infty}$ and F_∞ become extensive.

In Fig. 2.10 we plot the long-time values $S_{L/2, \infty}$ and F_∞ as a function of the injected energy and we show the MBME with a shadowed region. We can clearly notice, in Fig. 2.10a, how the MBME separates the intensive from extensive regime for the density fluctuations, which also display a maximum at the MBME as already observed in Ref. [27, 121]. The crossover is more gradual in the scaling of the entanglement entropy, which also for intermediate quenches shows a volume-law but characterized by a smaller growth-coefficient.

In order to get a more quantitative on the evolution of our results as a function of the quench amplitude, we perform a fit of the long-time values of the entanglement entropy $S_{L/2, \infty}$ and density fluctuations F_∞ using the following formulas:

$$S_{L/2, \infty} \propto \alpha_S \frac{L}{2} \quad F_\infty \propto \alpha_F \frac{L}{2} \quad (2.37)$$

We show the results for the coefficients α_S and α_F in Fig. 2.11 as a function of both Δ_i and ϵ .

Both α_S and α_F display the same trend: they start from a value close to

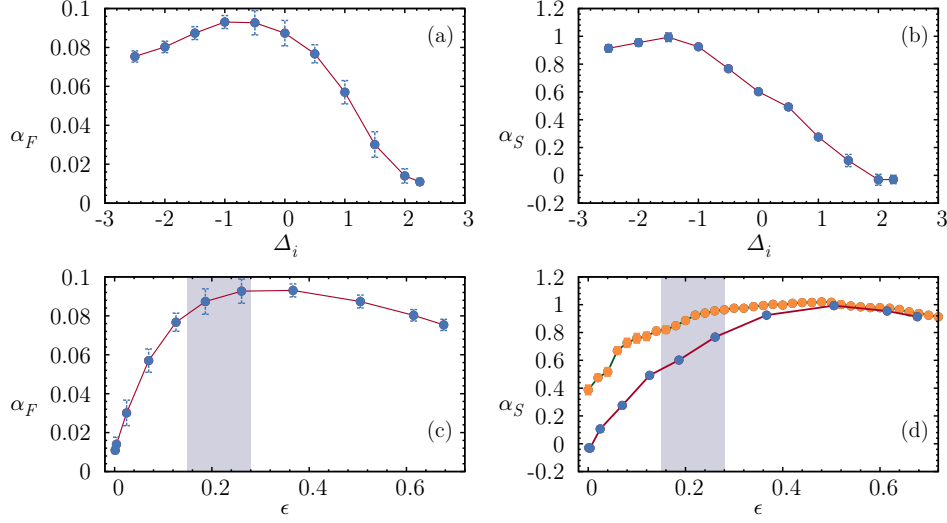


Figure 2.11: Coefficients of the linear fit, as in (2.37), performed for the long-time values of the entanglement entropy $S_{L/2,\infty}$ and of the density fluctuations F_∞ . In panel (d) we also show the coefficient α_S^{TH} obtained from fitting the Boltzmann thermal entropy S_B .

zero for small quenches (and small ϵ); they grow by increasing the amplitude of the quench; they reach a maximum for intermediate quenches (around $\epsilon \simeq 0.5$) and they slightly decrease for even larger quenches. Interestingly the maximum value for α_S is equal to 1, consistent with the value of the entropy density, (2.25), for a thermal state at infinite temperature.

We can obtain further insight by comparing the results of the quench dynamics with the microcanonical Boltzmann entropy as a function of energy. Making use of the exact diagonalization results presented in Sec. 2.3 for any energy ϵ we calculate the logarithm of the number of states N_ϵ in the energy window $[\epsilon - 0.05, \epsilon + 0.05]$ for each realization of the disorder; and then we average over different realizations, to obtain the microcanonical equilibrium entropy:

$$S_{MC}(\epsilon, \phi) = \log_2(N_\epsilon) \quad \rightarrow \quad S_{MC}(\epsilon) = \langle S_{MC}(\epsilon, \phi) \rangle_\phi . \quad (2.38)$$

We performed this calculation for different sizes of the system and we then fit the results in order to extract the equilibrium entropy density $s_{MC}(\epsilon)$

$$S_B(\epsilon) \propto s_{MC}(\epsilon) \frac{L}{2} \quad (2.39)$$

Panel (d) of Fig. 2.11, compares the entanglement entropy density obtained from the stationary regime following a quench with energy injection ϵ and

the microcanonical entropy density.

The equivalence between the two entropy densities implies that the ETH regime is reached for sufficiently large quenches, whereas the MBL is manifested in the case of small quenches: namely even if the entanglement entropy becomes extensive, the entropy density is well below its thermal value. This is a clear signature for the MBL transition, and it provides evidence that our spectroscopy protocol detects the presence of a MBME in the spectrum making use of controlled quench dynamics.

2.5 Conclusions

In this Chapter we analyzed a generalization of the Aubry-André model to interacting fermions from different point of view. We described numerically its phase diagram at half filling as a function of quasi-disorder and interaction, showing the existence a localized phase (LOC) and other three different regimes: LL, CDW and PS. Especially we estimate for a particular value of the interaction $V = 2$ the LL-LOC transition to occur at $\Delta = 2.5 \pm 0.1$ and $\Delta = 1.5 \pm 0.1$ respectively in the ground and in the most excited state of the Hamiltonian.

Motivated by this asymmetry in the two transitions, we then studied the properties of the excited state of the Hamiltonian looking for a many-body mobility edge in the spectrum, i.e. an energy threshold that separates localized from ergodic states. Collecting results from the level statistics of adjacent energy gap, the entanglement entropy and its variation we provide clear evidences for the existence of a many-mobility edge in the spectrum. In particular we estimate the many-mobility edge to take place for $V = 2$ and $\Delta = 2.5$ in the energy density window $[0.72, 0.85]$.

Finally we propose a method, and we provide numerical results of its validity, for detecting the mobility edge via quench-spectroscopy, particularly interesting because it can be easily implemented in an experimental setup of ultracold atoms.

3

Bound states and expansion dynamics of bosons on a one-dimensional lattice

“A sam cum in trii su onna scrana e un c'al spénz par salir”

— Detto popolare

We derive in the first Sec.3.1 the exact solution of the two-bosons problem for the Hamiltonian (3.1) on a finite lattice with periodic boundary conditions. We find scattering and bound-state eigenfunctions for both attractive and repulsive interactions. We then analyze the effects of bound states in the dynamical evolution of the system, when the initial state is not an eigenstate of the Hamiltonian. We consider two classes of initial conditions: a) *product states*, corresponding to bosons with well defined initial positions in real space, and b) *entangled states*, corresponding to the ground states of a non interacting Bose-Hubbard Hamiltonian, in an open box of size l . We collect some results about the expansion of a single boson on a lattice in Sec.3.4. In Sec. 3.5 we draw our conclusions. In Appendices 3.A and 3.B we give details respectively on the formulas for the expansion velocities in the non-interacting case and on the $U \leftrightarrow -U$ inversion theorem, as formulated in Ref. [177].

3.1 The two-boson problem on a lattice: exact results

We study the expansion dynamics of two bosons on a lattice as ruled by the Hamiltonian of the well know Bose-Hubbard model [178]:

$$\mathcal{H}(U) = -J \sum_{j=-L/2}^{L/2} \left(b_j^\dagger b_{j+1} + b_{j+1}^\dagger b_j \right) + \frac{U}{2} \sum_{j=-L/2}^{L/2} \hat{n}_j (\hat{n}_j - 1) \quad (3.1)$$

where $\{b_j^\dagger, b_j\}$ is a set of bosonic creation and annihilation operator, J and U are respectively the hopping and the on-site interaction coefficients and $\hat{n}_j = b_j^\dagger b_j$ is the number operator. In the following we will fix the size of the

system to $L + 1$, with L even.

Despite the non-integrability of the Hamiltonian (3.1) [179], it is possible to solve the Schrödinger equation for two particles exactly thanks to the separation of center-of-mass and relative coordinates. This method is a kind of simplification of the Bethe ansatz technique and was exploited by Valiente and Petrosyan, for studying the system in the thermodynamic limit, in two previous works [180, 181].

A general eigenstate of \mathcal{H} takes the form

$$|\phi\rangle = \sum_{j,k=-L/2}^{L/2} \phi_{jk} b_j^\dagger b_k^\dagger |0\rangle \quad (3.2)$$

where the coefficients ϕ_{jk} are symmetric under the exchange of j and k and properly normalized. Moreover, they have to satisfy, for every k and j the system of equations :

$$J(\phi_{j+1,k} + \phi_{j-1,k} + \phi_{j,k+1} + \phi_{j,k-1}) - (U\delta_{jk} - E)\phi_{jk} = 0 \quad (3.3)$$

Following the standard prescription of the Bethe Ansatz [182] we look for solutions with the following form:

$$\begin{aligned} \phi_{jk} &= \left[a_{12} e^{i(p_1 j + p_2 k)} + a_{21} e^{i(p_1 k + p_2 j)} \right] \vartheta(j - k) + \\ &+ \left[a_{12} e^{i(p_1 k + p_2 j)} + a_{21} e^{i(p_1 j + p_2 k)} \right] \vartheta(k - j) \end{aligned} \quad (3.4)$$

where $\vartheta(\cdot)$ is the Heavyside function defined in the origin as $\vartheta(0) = 1/2$. We now rewrite the eigenfunctions (3.4) in the following way

$$\phi_{jk} = e^{iPX} \left(a_{12} e^{ip|x|} + a_{21} e^{-ip|x|} \right) \quad (3.5)$$

where we have defined the center-of-mass and relative coordinates of the two particles by

$$X = \frac{j+k}{2} \quad x = j - k \quad (3.6)$$

and their corresponding momenta by

$$P = p_1 + p_2 \quad p = \frac{p_1 - p_2}{2} \quad (3.7)$$

Imposing (3.5) to be a solution of (3.3) we find that the energies E of the

eigenfunctions are given by:

$$E = -2J (\cos p_1 + \cos p_2) = -4J \cos \frac{P}{2} \cos p \quad (3.8)$$

By now imposing periodic boundary conditions ($\phi_{j,-L/2} = \phi_{j,L/2+1}$), we can fix the values of the relative and center of mass momenta P and p , which have to satisfy the two equations:

$$P_n = \frac{2\pi n}{L+1} \quad (3.9)$$

$$(-1)^n e^{ip(L+1)} = y(P_n, p) \quad (3.10)$$

where n as integer values in the set $n \in \{-L/2, \dots, L/2\}$ and the function $y(P, p)$ is defined by:

$$y(P, p) \equiv \frac{a_{21}}{a_{12}} = -\frac{U - 4iJ \cos \frac{P}{2} \sin p}{U + 4iJ \cos \frac{P}{2} \sin p} \quad (3.11)$$

This last equation must be solved numerically and for every different value of n gives us $L/2 + 1$ solutions giving a total of $(L/2 + 1)(L + 1)$ independent eigenstates.

While the values of P_n are for construction always reals, the solutions for the relative momentum p can be either real, leading to *scattering* eigenstates, or pure imaginary, leading to *bound* eigenstates. We will denote them with $|s\rangle$ and $|b\rangle$ respectively, with coefficients ϕ_{jk}^s, ϕ_{jk}^b and energies E_s and E_b .

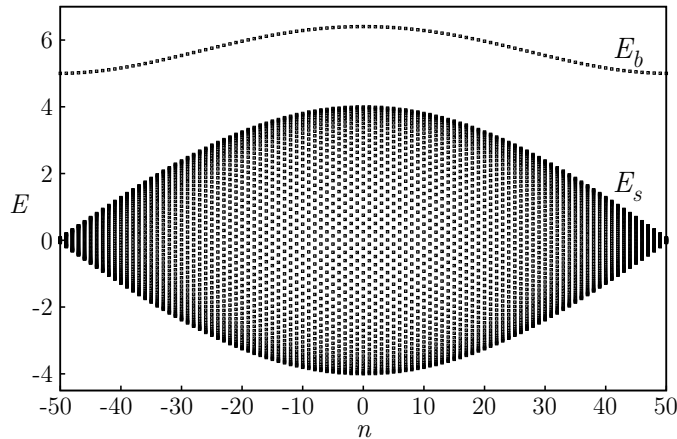


Figure 3.1: Energy spectrum of the 2 particle Bose-Hubbard model (3.1) on a chain with $L + 1 = 101$ sites and interaction $U = 5$.

In Fig. 3.1 we show the full energy spectrum for a chain with $L + 1 = 101$ and for an interaction $U = 5$. We can see that the scattering states form a band that becomes continuous in the thermodynamic limit. Moreover, the bound states persist even in presence of a repulsive potential but with energies that lie above the scattering band. It is easily seen from Eq. (3.10), that the whole spectrum is inverted by changing $U \rightarrow -U$. Therefore, in the attractive case, the bound states lie below the scattering ones, as expected. Let us observe that the energies of the bound states are shifted by changing U . In particular, if $|U| < 4J$, the bound states close to the boundaries of the Brillouin zone, have energies lower than the top of the scattering band. These results fit perfectly with those obtained by Valiente and Petrosyan with a different methods [180, 181].

We will now study the time evolution of the system with the following scheme. We choose the system to be, at $t = 0$, in the initial state

$$|\psi_0\rangle = \sum_{j,k=-L/2}^{L/2} \psi_{jk}^0 b_j^\dagger b_k^\dagger |0\rangle \quad (3.12)$$

completely determined by the coefficients ψ_{jk}^0 . The evolved state at a time t then will be given by

$$\begin{aligned} |\psi(t)\rangle &= e^{-it\mathcal{H}(U)} |0\rangle \\ &= \sum_s C_0^s e^{-itE_s} |s\rangle + \sum_b C_0^b e^{-itE_b} |b\rangle \end{aligned} \quad (3.13)$$

where

$$C_0^{s/b} = \langle s/b | \psi_0 \rangle = 2 \sum_{j,k=-L/2}^{L/2} \left(\phi_{jk}^{s/b} \right)^* \psi_{jk}^0 \quad (3.14)$$

We are interested in evaluating expectation values of observables on the evolved state. In particular, we focus on the density

$$\rho_j(t) = \frac{n_j(t)}{2} = \langle \psi(t) | \frac{\hat{n}_j}{2} | \psi(t) \rangle \quad (3.15)$$

and on the single and double occupations

$$s_j(t) = \langle \psi(t) | \hat{n}_j (2 - \hat{n}_j) | \psi(t) \rangle \quad (3.16)$$

$$d_j(t) = \langle \psi(t) | \frac{\hat{n}_j (\hat{n}_j - 1)}{2} | \psi(t) \rangle \quad (3.17)$$

To compute them we need the matrix elements of \hat{n}_j and \hat{n}_j^2 between the eigenstates of H , which are given, using the previous relations, by:

$$\langle \alpha | \hat{n}_j | \beta \rangle = 4 \sum_{k=-L/2}^{L/2} (\phi_{jk}^\alpha)^* \phi_{jk}^\beta \quad (3.18)$$

$$\langle \alpha | \hat{n}_j^2 | \beta \rangle = 4 (\phi_{jj}^\alpha)^* \phi_{jj}^\beta + \langle \alpha | \hat{n}_j | \beta \rangle \quad (3.19)$$

where α and β can stand for either s or b .

3.2 Dynamics of product states

In this Section, we will study the time evolution, ruled by the Hamiltonian (3.1), of two different initial types of state: *product* state in real space corresponding to two bosons on the central site of the chain:

$$|\psi_{PS}^1\rangle = \frac{1}{\sqrt{2}} (b_0^\dagger)^2 |0\rangle \quad (3.20)$$

or corresponding to a state with two bosons on two adjacent sites:

$$|\psi_{PS}^2\rangle = b_0^\dagger b_1^\dagger |0\rangle \quad (3.21)$$

The latter resembles the one reproduced experimentally in the work by Ronzheimer et al. [76], where product states of N bosons on N adjacent sites were considered.

In the following we will consider just non-negative values of $U \in [0, 31]$, since it was proven in Ref. [177] that for the initial product states and for the observables we are considering (3.15,3.16,3.17) the dynamics performed with $\mathcal{H}(U)$ or $\mathcal{H}(-U)$ is specular (see Appendix 3.B for a more precise discussion of this point).

We perform the numerical simulation on a system of length $L + 1 = 25$, evolved up to a final time $t = 4$ (from now on, we will measure time in units of the hopping rate J defined in (3.1) and set $\hbar = J = 1$). The results we presents are obtained using the exact formulas we explicitly calculate in the previous Sec. 3.1.

3.2.1 $|\psi_{PS}^2\rangle$: two bosons on adjacent sites

In this section we study the dynamical profiles of $\rho_j(t)$, $s_j(t)$ and $d_j(t)$ at different values of the interaction. starting from a states made by two bosons

on adjacent sites $|\psi_{PS}^2\rangle$. The behavior, as is showed in Fig. 3.2 turns out to be quite peculiar: increasing U , the density profile, displaying a typical free form for $U = 0$ and in the limit of large interactions whereas it changes for intermediate interactions. This is explained by the fact that, in the limit of large U also called *hard-core* limit [76], the interacting bosons become equivalent to free fermions [179]. The similarity between the density for zero and large interactions is possible just because the initial state is without double occupations. This will not be the case for the initial states in the following section $|\psi_{PS}^1\rangle$ where we will discover different phenomena.

While the single-occupation profile shows a similar behavior, the double-occupation one differs significantly. In fact in the large- U regime, as a sign of the fermionization of the dynamics double occupations are almost absent. Another interesting feature is that for intermediate values of the interaction (e.g. $U \simeq 5$) the double occupations of the central sites, that were completely suppressed for $t = 0$, are quite stable vanishing only at large times. This phenomenon is known as *quantum distillation* [75], and was experimentally observed for many particle wave functions, both in the case of spin-1/2 fermions [75, 77] and of bosons [76].

We analyze now the *expansion velocities*, defined as

$$v = \frac{d}{dt} \sqrt{R^2(t) - R^2(0)} \quad (3.22)$$

where $R^2(t)$ represents the time-dependent variance of the density distribution:

$$R^2(t) = \frac{a^2}{N} \sum_{j=-L/2}^{L/2} n_j(t) (j - j_0)^2 \quad (3.23)$$

In Fig. 3.3(a) we show with a contour plot the numerical results obtained for the expansion velocity $v(t, U)$ as a function of time and interactions. We notice that the initial velocity $v(t = 0)$ is independent of the interaction U and as can be seen in the inset is equal to the velocity of the free case (3.35) $v = \sqrt{2}$. Moreover, as also shown in the inset, for $U \neq 0$, some damped oscillations of v as a function of t appear, with a period $T(U)$ that decreases as U increases.

We move now to the study of the asymptotic expansion velocities $v_\infty(U)$. For large time at each U we estimate it by fitting $v(t)$ in the range of time $t \in [2, 4]$ with the following phenomenological formula that allows us to avoid spurious effects from the transient oscillatory region:

$$v(t) = v_\infty(U) + A(U) \cos\left(\frac{2\pi t}{T(U)} + \phi\right) / t^\eta \quad (3.24)$$

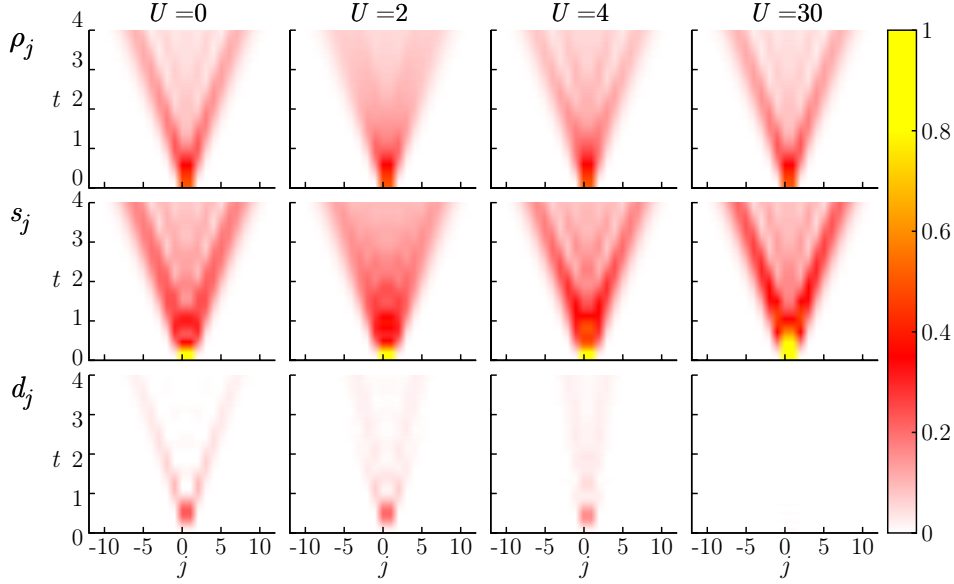


Figure 3.2: Dynamical profiles of density ρ_j (first row), single s_j (second row) and double d_j occupations (third row) for an initial product state $|\psi_{PS}^2\rangle$ for different values of the interactions $U = 0, 2, 4$ and 30 .

We plot the results obtained for $v_\infty(U)$ in Fig. 3.3(d) as a function of the interaction U . We found that our results for two particles model is very similar to the one observed in the many-body case [76]. In fact $v_\infty(U)$ approaches the free value $\sqrt{2}$ in the two limit cases $U = 0, +\infty$ (see Appendix 3.A for more details) and displays a minimum for an intermediate value $U \simeq 2$.

A recent work by Sorg et al. [183] studied the large- U behavior of the expansion velocity $v_\infty(U)$ for a many-body system and they show that, for an initial state with only single occupations and in the strong-repulsive regime, $v_\infty(U) \sim \sqrt{2} + a/U^2$, where a is a constant. We check this prediction fitting our numerical data and the result is shown in Fig. 3.3(d). We found an excellent agreement between numerics and the analytic prediction and we estimated the coefficient a of the fit as $a \simeq -3.80$

We also studied the period $T(U)$ and the amplitude $A(U)$ of the damped oscillations of $v(t)$. In the regime of strong interaction, $T(U \geq 5)$, they display a clean power-law behavior as showed in Figs. 3.3(b) and (c). We extrapolated the exponent of the power law decaying fitting data according to the formula $T(U)/A(U) = a_0/U^{a_1}$. For the period $T(U)$ we found a decays exponent very close to 1, $a_0 \simeq 6.41$ and $a_1 \simeq 1.01$, whereas for $A(U)$ we obtained the following values $a_0 \simeq 1.91$ and $a_1 \simeq 1.31$.

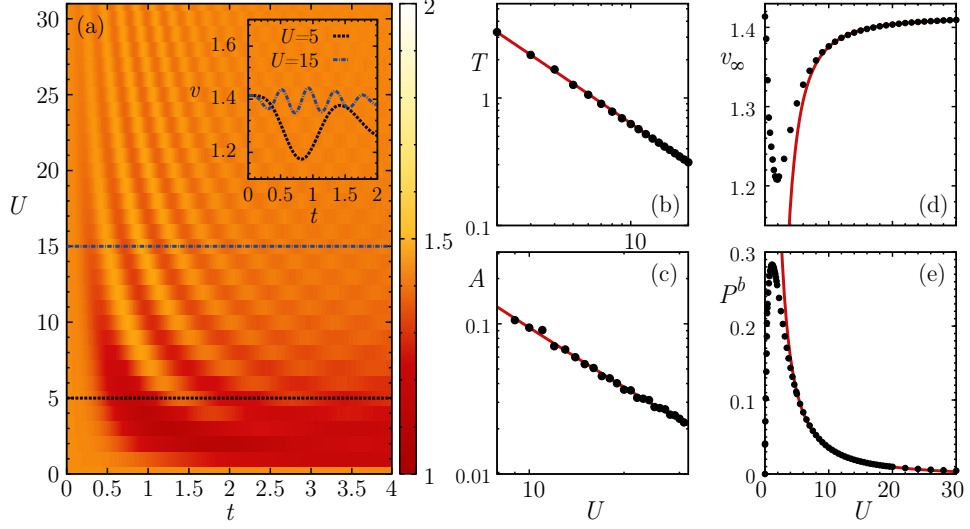


Figure 3.3: Features of the expansion velocity for an initial state $|\psi_{PS}^2\rangle$. Panel (a): expansion velocity $v(t, U)$ for $U \in [0, 31]$; inset: $v(t)$ for $U = 5$ and $U = 15$. Panels (b) and (c): large- U dependence of $T(U)$ and $A(U)$, as obtained by fitting $v(t, U)$ according to Eq. 3.24. Panel (d): asymptotic expansion velocity $v_\infty(U)$. Panel (e): projection $P^b(U)$ of the state $|\psi_{PS}^2\rangle$ on the bound states of (3.1).

We can get some more details of the asymptotic velocity behavior studying the role that bound states play during the dynamical evolution. We consider the projection of the wave functions on the subspace spanned by the bound states. This quantity is time independent by construction and is defined as:

$$P^b(t) = \sum_b |\langle b | \psi(t) \rangle|^2 \equiv P^b(0) = \sum_b |C_0^b|^2 \quad (3.25)$$

In panel (e) of Fig. 3.3 we show the numerical results obtained for the projection P^b as a function of the interaction U . We can see at a glance from a comparison between the panel (e) and (d) that the larger the projection P^b , the smaller the rate of expansion of the wave packet is. In fact when the projection of the wave function over the bound states is small, then the evolution is almost free-like, resulting in a fast expansion. In the opposite regime, when the initial state has a large projection, the expansion velocity decreases as particle where *captured* by bound states. We also fitted, with a really good agreement as can be seen in (In Fig. 3.3(e)), the large U tale of the projection with a power law decaying $P^b(U) = a_0/U^{a_1}$, obtaining $a_0 \simeq 1.33$, $a_1 \simeq 1.52$.

Despite the qualitative agreement between the shapes of v_∞ and P^b as functions of U , we noticed a quantitative displacement in the positions of the maximum of P^b with respect to the minimum of v_∞ . We argue that this effect can be explained by the difficulty that we have in extracting the true

value of v_∞ in the small- U regime from the numerical data (we remind that P^b is always an exact quantity).

3.2.2 $|\psi_{PS}^1\rangle$: two bosons on the same site

We now analyze the dynamics for an initial product state $|\psi_{PS}^1\rangle$ prepared with two bosons confined on the same site. The expansion of a generalization of this type of state to a many-body system, i.e. a Mott-insulator like state with double occupancy, was studied in Ref. [184]. In Fig. 3.4 we show the numerical results, obtained in the same way of the last section, for dynamical profiles of the density, single and double occupations. In this case although for small U the expansion is free-like this is no longer valid $U = +\infty$ where the mapping from hard-core bosons to free fermions can be applied because of double occupations in the initial state $|\psi_{PS}^1\rangle$ [76]. Comparing Fig. 3.4 with Fig. 3.2 we can notice that the role of double and single occupations is reversed. In fact starting from $|\psi_{PS}^2\rangle$ the double occupations are stable also for large U while the single occupations, zero at $t = 0$, are finite only in the small U regime.

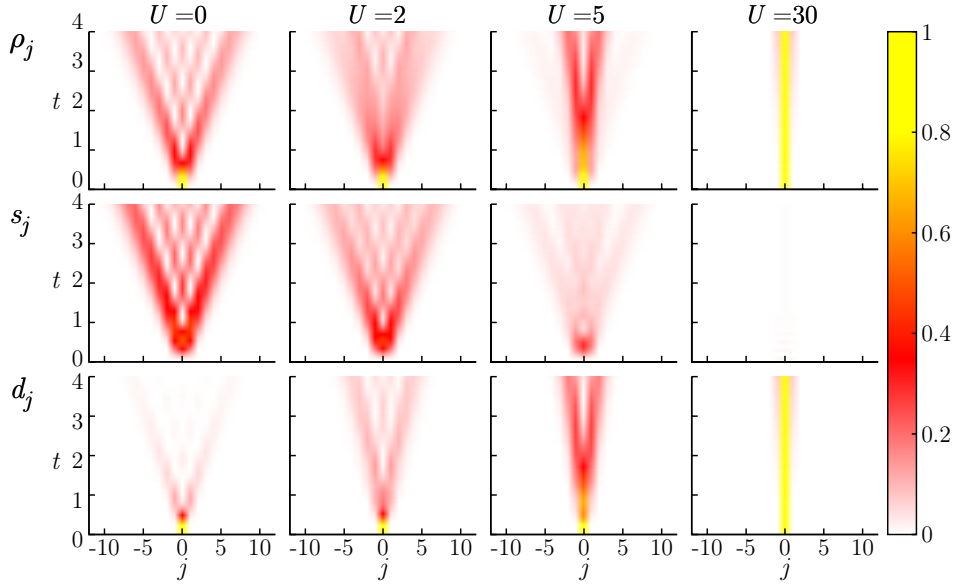


Figure 3.4: Dynamical profiles of density ρ_j (first row), single s_j (second row) and double d_j occupations (third row) for an initial product state $|\psi_{PS}^1\rangle$ for $U = 0, 2, 5$ and 30 .

In Fig. 3.5(a) we show with a contour plot the numerical results obtained for the expansion velocity $v(t,U)$ as a function of time and interactions.

As in the previous case, the initial velocity $v(t = 0)$ is independent of the interaction U and damped oscillations of v as a function of t appear, with

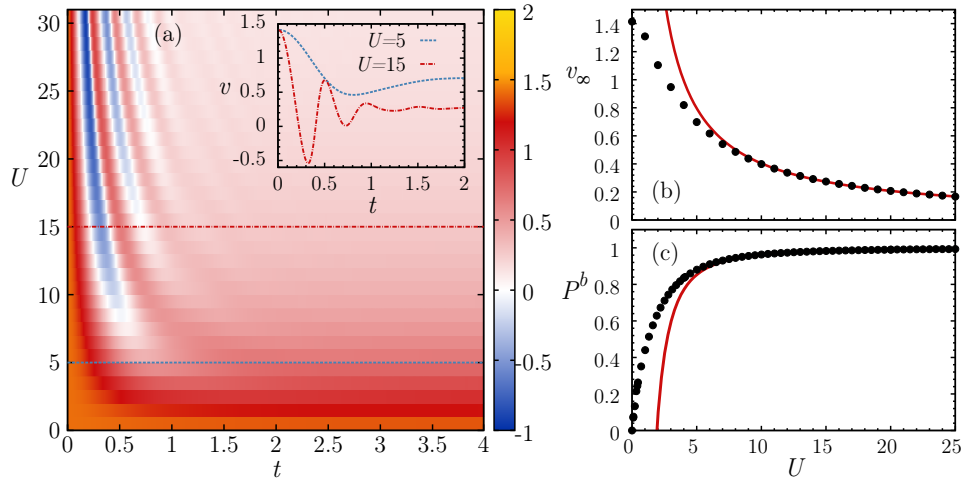


Figure 3.5: Features of the expansion velocity for an initial state $|\psi_{PS}^1\rangle$. Panel (a): expansion velocity $v(t, U)$ for $U \in [0, 31]$; inset: $v(t)$ for $U = 5$ and $U = 15$. Panel (b): asymptotic expansion velocity $v_\infty(U)$. Panel (c): projection $P^b(U)$ of the evolved state on the bound states of (3.1).

a period $T(U)$ that decreases as U increases. Moreover, we found that for large U and early times the velocity periodically assumes negative values, signaling a “breathing” behavior of the wave packet at these times.

We then turn to the study of the asymptotic velocity $v_\infty(U)$. We noticed that in this case that oscillations are highly suppressed and the long time velocity is almost flat. We therefore fits $v(t, U)$ in the interval $t \in [3, 4]$ with a constant and the results are plotted in Fig. 3.5(b). We observe that v as a function of U presents a decreases monotonically for all the considered values of the interaction and that in this case, the large- U values of v are well fitted by a power law. We fit data according to the equation $v_\infty(U) \sim a_0/U^{a_1}$, giving $a_0 \simeq 3.84$, $a_1 \simeq 0.97$ and we found a perfect agreement as shown in Fig. 3.5b.

Even in this case we found that large velocity and free expansion correspond to a small projection of the wave function on the bound states, and vice versa, illustrating the importance of the bound states even in this situation. Moreover, for large U , the projection on the bound states is shown to saturate to 1 as $1 + 1/U^2$. We perform a fit according to the power law $P^b(U) = 1 + a/U^2$, founding $a \simeq -3.67$ and we show it in Fig. 3.5(c).

3.3 Dynamics of entangled states

In this section, we consider a different kind of initial states, that we call *entangled*, since they are not a direct product in real space, but are obtained putting the two non interacting particle in the ground state of an open box

of length l .

$$|\psi_{ES}^l\rangle = \frac{1}{\sqrt{2}} (\tilde{b}_1^\dagger)^2 |0\rangle \quad (3.26)$$

where, \tilde{b}_1^\dagger represents the creation operator for particle of minimum momentum [185]. Generalization of this type of states were also considered in a recent work by Vidmar et al. [186]. The numerical results we will present in the following are obtained using the exact methods we discussed in Secs. 3.1.

We start our analysis with the free case: as in the product cases of Sec.3.2, the free evolution separates into two beams. This particular behavior is explicitly studied in Sec.3.4 where we will show that this effect is due solely to the lattice. This phenomenon disappears if the size of the initial wave packet is much larger than the lattice spacing, when particles stop to feel the discrete nature of the system.

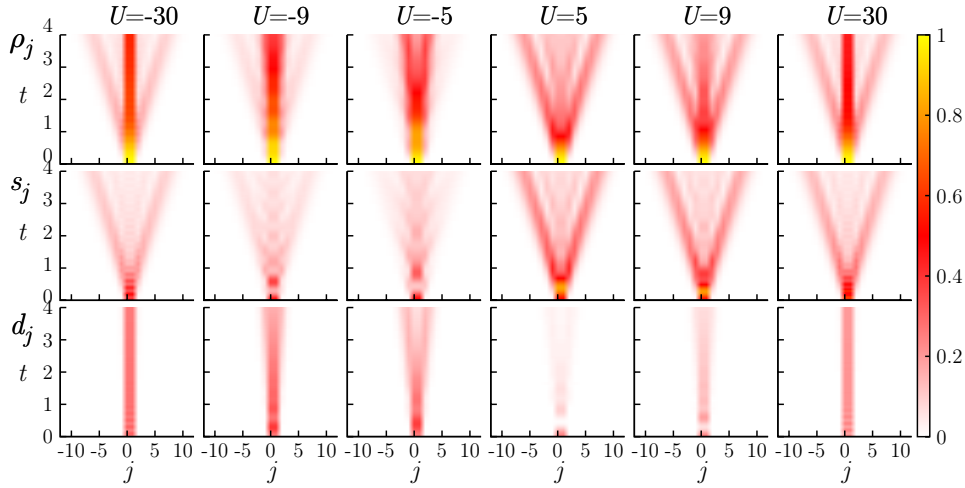


Figure 3.6: Dynamical profiles of density ρ_j (first row), single s_j (second row) and double d_j occupations (third row) for an initial entangled state $|\psi_{ES}^2\rangle$ for $U = -30, -9, -5, 5, 9$ and 30 .

We studied the expansion velocity of the two particle varying the size l of the initial confinement. Although the time dependence of v in the free case is trivial since $v(t)$ is constant we found that increasing l , the expansion velocity decreases with a power law $\sim l^{-1}$. This is also the behavior one would have in the continuum case for a Gaussian wave packet 3.29, where $v \sim \sigma^{-1}$. The l -dependence of the expansion velocity for $11 \leq l \leq 31$ and $L + 1 = 51$, is also shown in Fig. 3.7b.

We then move to the study of the interacting system, where $U \neq 0$. It must be pointed out that the entangled states are characterized by a non zero value of both s_j^0 and d_j^0 , therefore they do no longer satisfies the conditions

for the validity of the $U \leftrightarrow -U$ theorem (see Appendix 3.B) and we have to perform different calculations for positive and negative U .

In Fig. 3.6 we show the numerical results, in the case $l = 2$, for the profiles of density, single and double occupations for different values of the interaction $U \in [-31, 31]$. We performed similar analysis also for the cases $l = 3, 4$ but they display almost only quantitative differences. Whereas mathematical equality between the large-positive and large-negative U regimes does not exist, the profiles are very similar to each other, while differences appears for intermediate values of $|U|$. Interestingly whereas for small negative U 's, the behavior is similar to the large $|U|$'s ones, for small positive U 's it is more similar to the free ones. In order to have more insights we will analyze the projection of the wave function on the bound states, $P^b(U)$ (Eq. 3.25) and the expansion velocities.

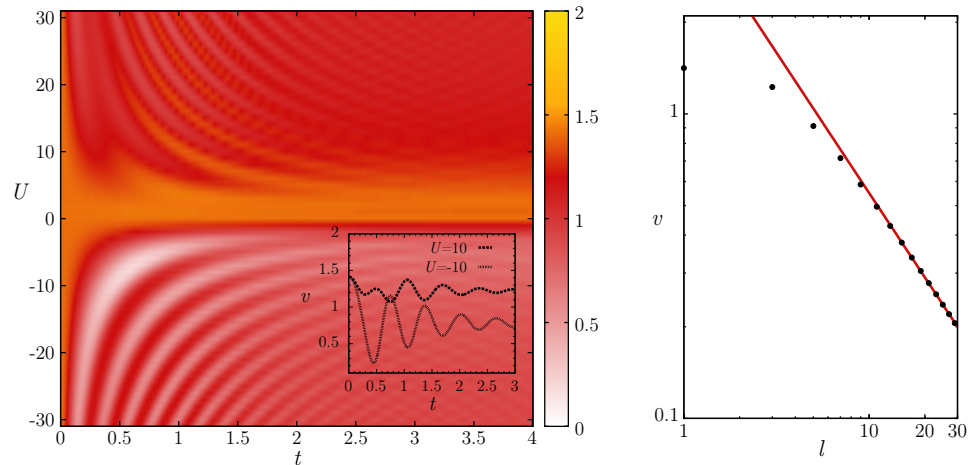


Figure 3.7: Panel (a): expansion velocity $v(t, U)$ for an initial entangled state $|\psi_{ES}^2\rangle$ and $U \in [-31, 31]$; inset: $v(t)$ for $U = \pm 10$. Panel (b): expansion velocity of an entangled wave packet in the non-interacting case as a function of the initial confinement length $11 \leq l \leq 31$, with a total system size $L+1 = 51$. The black dots are the numerical data, while the red solid line is the best fit for large l , performed with the formula $y = a_0/x^{a_1}$, resulting in $a_0 \simeq 4.37$, $a_1 \simeq 0.91$. The plot is in log-log scale.

We then move to the analysis of velocities and projection of the wave function on the bound states. In Fig. 3.7a we show in a contour plot the numerical results for the expansion velocities as a function of time t and interaction U for an initial box size of $l = 2$. For different sizes $l = 4, 5$ we observed a similar oscillating behavior for short time and then a saturation to certain value $v_\infty(U)$.

For the entangled states we had to perform a different fitting procedure. For $l = 4$ and for negative U 's of $l = 3$ the oscillation are highly suppressed and

we can fit data just with a constant. In the other cases we use for the fit a 9-parameters phenomenological formula in order to extract $v_\infty(U)$.

$$v(t) = v_\infty(U) + A_1 \cos\left(\frac{2\pi t}{T_1} + \phi_1\right)/t^{\eta_1} + A_2 \cos\left(\frac{2\pi t}{T_2} + \phi_2\right)/t^{\eta_2} \quad (3.27)$$

The fit results of $v_\infty(U)$ for $l = 2, 3$ and 4 are shown in the first row of Fig. 3.8b:

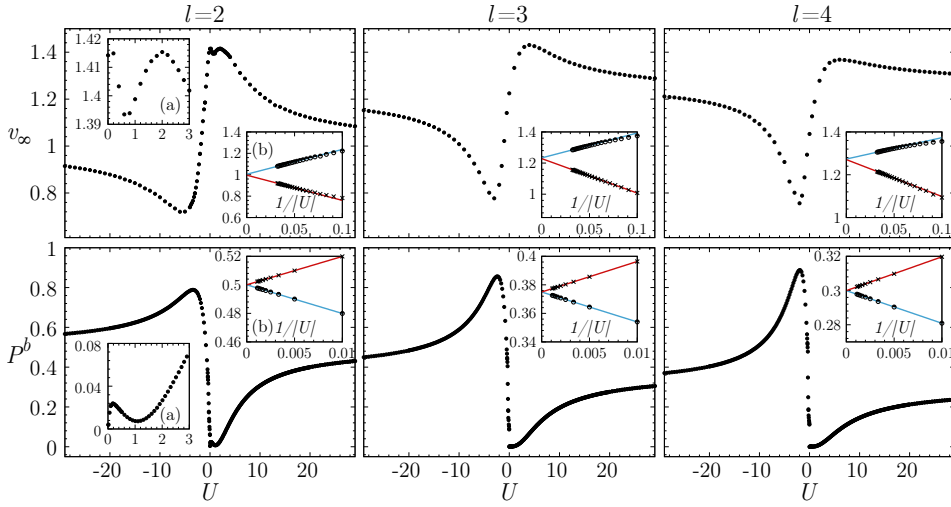


Figure 3.8: (Color online) First row: asymptotic expansion velocities as functions of $U \in [-31, 31]$ for initial entangled states with $l = 2, 3$ and 4 . Second row: projection of the wave function over the bound states as a function of $U \in [-31, 31]$ for initial entangled states with $l = 2, 3$ and 4 . Insets (a) of the $l = 2$ data: magnification of the regions $U \in [0, 3]$; remaining insets: best fits of the large- $|U|$ data with power laws $a_0 + a_1/|U|$ (circles/crosses: numerical data with $U > / < 0$; red/light-blue solid line: best fit for $U > / < 0$). Results of the best fits (in any case the a_0 for the positive and negative U 's coincide to the second digit): first row: left panel: $a_0 \simeq 1.00$; central panel: $a_0 \simeq 1.23$; right panel: $a_0 \simeq 1.27$; second row: left panel: $a_0 \simeq 0.50$; central panel: $a_0 \simeq 0.37$; right panel: $a_0 \simeq 0.30$.

In all of the three situations, $l = 2, 3, 4$, an absolute maximum and an absolute minimum are present when the absolute value of the interaction is small. Moving to large interaction, both attractive in repulsive, the velocities are monotonic and approach the same asymptotic values for $U \rightarrow \pm\infty$. We estimate them using a simple power law $v_\infty(U) \sim a + b/U$, as shown in the insets of the first row in Fig. 3.8.

this fact can be easily understood by looking at the occupation profiles in Fig. 3.6, showing that both for negative and positive U the evolution is dominated by the coherent propagation of double occupations.

In the second row of Fig. 3.8 we plot the projection $P^b(U)$, defined in (3.25). Also for entangled states we found that at larger velocities correspond smaller P^b , and vice versa, highlighting the direct correspondence between velocities and projection on the bound states. This general property is confirmed by the asymptotic values of P^b , estimated in analogy with the velocity using a simple power law, that coincide for $U \rightarrow \pm\infty$ (insets of the second row in Fig. 3.8).

3.4 Effect of the lattice on the expansion dynamics

As already emphasized, one of the most remarkable aspects related to the expansion of quantum matter on a lattice is the appearance of two quasi-coherent beams, departing from the centre of the initial wave packet with at the same time a depletion in the center of the system. This effect is in contrast with what happens in the continuum. In this second situation, only for a free model, a Gaussian wave-packet will have the same shape during all the evolution, with a spread $\sigma(t)$ that grows with time [187]. Such beams have been recently observed theoretically and experimentally, both for bosons [76, 78, 186] and for fermions [186, 188] in lattice systems and seem to be absent for continuum models [177]. The effects of the discreteness induced by the lattice have already been stressed by Rigol et al. [78, 79], who argued that the most populated states in the diffusion process are at a certain value of the momentum p_0 , depending on the mean value of the energy $\langle H \rangle$ (with $p_0 = \pm\pi/2$ when $\langle H \rangle = 0$). This argument supports the fact that the two-beam effect is almost insensible on the choice of the initial state.

We start analyzing the continuum case, where the spatial coordinate $x \in \mathbb{R}$ [187]. If we start with a Gaussian wave packet of standard deviation σ , the particle density will have at any time a Gaussian shape

$$\rho(x, t) = \frac{1}{\sigma(t)\sqrt{\pi}} e^{-\frac{x^2}{\sigma^2(t)}} \quad (3.28)$$

with a time-dependent variance:

$$\sigma^2(t) = \sigma^2 + \left(\frac{\hbar t}{m\sigma} \right)^2 \quad (3.29)$$

In Fig. 3.9(a) we show the spreading of a gaussian wave packet in continuum system, for $\sigma = 0.1$. Here we set $m = \hbar = 1$, space is measured in units of σ and time in units of $m\sigma^2/\hbar = \sigma^2$.

In the other hand we can study an infinite lattice. We define the single

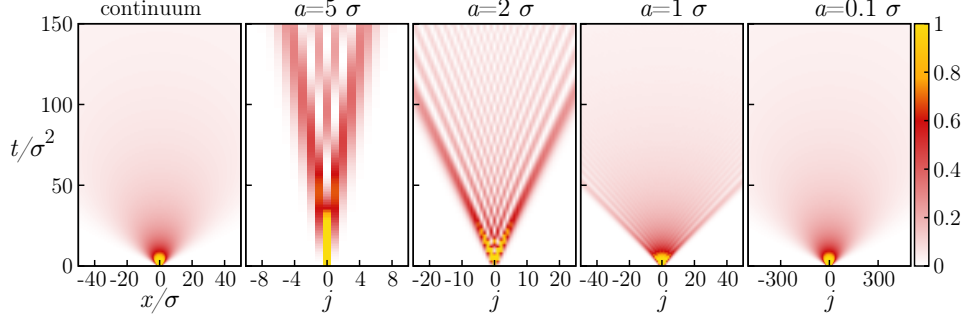


Figure 3.9: Expansion of a Gaussian wave packet with $\sigma = 0.1$ in the continuum (a) and in the lattice, with lattice spacing $a = 5\sigma$ (b), 2σ (c), σ (d) and 0.1σ (e). We restricted the plot to the region $x/\sigma, ja \in [-50, 50]$.

particle Hamiltonian as

$$\mathcal{H} = -\frac{\hbar^2}{2ma^2} \sum_{j \in \mathbb{Z}} \left(b_j^\dagger b_{j+1} + b_{j+1}^\dagger b_j \right) \quad (3.30)$$

where the constant in front is chosen to ensure the correct continuum limit. We can calculate easily all the eigenstates and their energy obtaining:

$$|p\rangle = \sqrt{\frac{a}{2\pi}} \sum_{j \in \mathbb{Z}} e^{ipja} b_j^\dagger |0\rangle \quad E(p) = -\frac{\hbar^2}{ma^2} \cos(pa) \quad (3.31)$$

Miming the model in the continuum, we choose an initial state with a normalized Gaussian profile:

$$|\psi(0)\rangle = A_{\sigma,a} \sum_{j \in \mathbb{Z}} e^{-\frac{j^2 a^2}{2\sigma^2}} b_j^\dagger |0\rangle \quad (3.32)$$

where $A_{\sigma,a} = \left[\theta_3 \left(0, e^{-\frac{a^2}{\sigma^2}} \right) \right]^{-1/2}$ and $\theta_3(z, q)$ is the third elliptic theta function that can be found in [189]. We can now obtain with some straightforward calculations the final equation:

$$|\psi(t)\rangle = \sum_{j \in \mathbb{Z}} \psi_j(t) b_j^\dagger |0\rangle \quad (3.33)$$

with

$$\psi_j(t) = \frac{\int_{-\pi}^{\pi} dp \theta_3 \left(-\frac{p}{2}, e^{-\frac{a^2}{2\sigma^2}} \right) e^{i \frac{\hbar t}{ma^2} \cos p} e^{ijp}}{2\pi \sqrt{\theta_3 \left(0, e^{-\frac{a^2}{\sigma^2}} \right)}} \quad (3.34)$$

In order to compare it with the continuum case we can compute the density as $n_j(t) = |\psi_j(t)|^2 / a$. In the last equation we put the lattice spacing in the denominator in order to recover the correct dimension, for comparing the results with the continuum case.

In Fig. 3.9(b)-(e) we show the numerical results for $\sigma = 0.1$ and for various decreasing values of the lattice spacing a miming a kind of continuum limit. While for large value of the lattice spacing a the two beams are clearly presents once we decrease the value of a at fixed σ , the profile density becomes similar to that in the continuum. This is also confirmed if we compare the two plots in the continuum and for $a = 0.1\sigma$: the difference between the values of the density is 10^{-3} or less.

Concluding, we have shown that the two quasi-coherent beams, departing from the centre of the initial wave packet, are present also in the single-particle case and are purely a consequence of discrete lattice where the particles move.

3.5 Conclusions

In this chapter we studied the dynamical effects of bosonic pairs in a 1D lattice, which may be coupled in bound states by short range interactions, both in the attractive and repulsive case. In the latter situation, the bound states originate from the discrete structure of the linear-combination-of-atomic-orbitals lattice. By means of the Bethe Ansatz we identified the bound states effects unambiguously and how the two-particles state evolves in time, depending on its initial projection on the bound states themselves. Starting the expansion from different initial states we found that in all the cases the larger the initial projection on the bound states, the larger the double occupation probability, and the smaller the expansion velocity. This provides a quantitative support to the importance of the bound pair states. Moreover, we discussed the role of the lattice in the shape of the evolved wave function, showing that it is the responsible of the separation of the evolved packet in two wave fronts propagating in opposite directions.

Appendices

3.A Expansion velocities for product states in the non-interacting case

In this Appendix we explicitly calculate the expansion velocity in the non-interacting case as defined by Eq. 3.22. We will find that the result is [76]

$$v = \frac{\sqrt{2}Ja}{\hbar} \quad (3.35)$$

In the following we set $\hbar = a = J = 1$.

Since we are in the non-interacting case, we can just consider one-particle wave packets that we assume to have initially the generic form

$$|\psi^0\rangle = \frac{1}{\sqrt{L+1}} \sum_p c_p \tilde{b}_p^\dagger |0\rangle \quad (3.36)$$

being \tilde{b}_p^\dagger the Fourier transform of b_j^\dagger . The density profile $n_j(t)$ can be written as a Fourier transform, in the $L \rightarrow \infty$ limit:

$$n_j(t) = \frac{1}{2\pi} \int_{-\pi}^{\pi} dq e^{-iqj} f_q(t) \quad (3.37)$$

where

$$f_q(t) = \frac{1}{2\pi} \int_{-\pi}^{\pi} dp c_p^* c_{p+q} e^{i[\epsilon(p+q) - \epsilon(p)]t} f_p(t) \quad (3.38)$$

$\epsilon(p)$ being the one-particle energies.

Let the initial wave packet be centered around the central site $j = 0$. Then, as in standard probability theory, the second moment of the occupation distribution, i.e., $R^2(t)$ (see (3.23)), can be computed from the generating function $f_q(t) = f(q, t)$ by the relation

$$R^2(t) = -\frac{\partial^2 f(q, t)}{\partial q^2} \quad (3.39)$$

When we take the initial state corresponding to one particle in the central

site $j = 0$, i.e. $c_p = 1$, it is easy to see that

$$R^2(t) = 2J^2t^2 \quad (3.40)$$

implying Eq. (3.35), as a consequence of the definition (3.22).

3.B $U \leftrightarrow -U$ inversion theorem

In this Appendix, we state the theorem, first proven in Ref. [177] (see also Refs. [190, 191]), ensuring the invariance of the dynamical expectation values of certain operators for a Hubbard-like Hamiltonian and a proper initial wave packet. We then prove that entangled states, as defined in Sec. 3.3, do not satisfy the hypothesis of the theorem.

Before stating it, we have to define the time-reversal operator \hat{R}_t as

$$\hat{R}_t e^{-it\hat{H}} \hat{R}_t^\dagger = e^{it\hat{H}} \quad (3.41)$$

and the π -boost operator \hat{B}_π as

$$\hat{B}_\pi b_j \hat{B}_\pi = e^{i\pi j} b_j \quad (3.42)$$

The theorem then states that if an observable quantity \hat{O} is invariant under the actions of the above defined operators, and the state at the initial time of evolution $|\psi^0\rangle$ is time-reversal invariant and just acquires a phase under the action of \hat{B}_π , then $\langle\psi(t)|\hat{O}|\psi(t)\rangle$ is the same if the time evolution is ruled by a Bose-Hubbard Hamiltonian with $\pm U$. The proof was carried out for the fermionic Hubbard Hamiltonian, but it can be trivially extended to the bosonic case.

It was proven in Ref. [177] that the product states we consider in Sec. 3.2 satisfy the hypothesis of the theorem; on the contrary, the entangled states of Sec. 3.3 do not. Indeed,

$$\begin{aligned} \hat{B}_\pi |\psi^0\rangle &= \hat{B}_\pi \frac{1}{\sqrt{2}} \left(\tilde{b}_1^\dagger\right)^2 |0\rangle = \\ &= \frac{1}{\sqrt{2}} \left[\sqrt{\frac{2}{l+1}} \sum_{j=1}^l \sin(p_1 j) \hat{B}_\pi b_j^\dagger \hat{B}_\pi \right]^2 |0\rangle = \\ &= \frac{1}{\sqrt{2}} \left[\sqrt{\frac{2}{l+1}} \sum_{j=1}^l (-1)^j \sin(p_1 j) b_j^\dagger \right]^2 |0\rangle \end{aligned} \quad (3.43)$$

that manifestly does not differ from $|\psi^0\rangle$ just by a phase factor. Therefore, in the entangled case, we must also consider negative U 's.

Dynamics of entanglement entropy crossing a quantum phase transition

“Presto e bene non stanno insieme”

— Detto popolare

In the first Sec. 4.1 we give a definition of entanglement entropy and entanglement spectrum and we present the model, its phases and the implementation of the dynamics. In Sec. 4.2 we describe the dynamics when letting the system go from the paramagnetic to the ferromagnetic phase by controlling the speed with which we change the magnetic field. We will examine the adiabatic regime, the sudden-quench situation and the cases with intermediate speeds. Then we will see, in Sec. 4.3 how these results are related to the so-called Kibble-Zurek mechanism [85–89], by looking both at the scaling of entanglement entropy and the so-called Schmidt gap [192–194] in the entanglement spectrum. We end with conclusions in the last Sec. 4.4, and with two Appendices, 4.A and 4.C, where we have reported technical details of the calculations.

4.1 The model

In this section we will study the dynamical evolution of the entanglement in the transverse field Ising model. This well known model [80–82] is described, for a chain of L sites with periodic boundary conditions (PBC), by the Hamiltonian:

$$H = -\frac{J}{2} \sum_{j=1}^L [\sigma_j^z \sigma_{j+1}^z + h \sigma_j^x] \quad (4.1)$$

here $\vec{\sigma}$ are the usual Pauli matrices, and $h = h(t)$ is a time-dependent magnetic field (see equation (4.2)). From now on we will set $\hbar = J = 1$.

This model is exactly solvable by a sequence of Jordan-Wigner, Fourier and Bogolyubov transformations. We will describe in details the method in

Appendix 4.A. The phase diagram of the model can be drawn as a function of the magnetic field h : it is composed by two phases, one *paramagnetic* ($h > 1$) and one *ferromagnetic* ($0 \leq h < 1$), separated by a quantum critical point $h = 1$. The negative part of the diagram is the mirror-reflected of the positive one, because of the \mathbb{Z}_2 symmetry under the canonical transformation $\sigma_j^x \rightarrow -\sigma_j^x$ [82]. At the critical point, for $h = 1$, the low-energy physics is described by a conformal field theory [195] with central charge $c = 1/2$ giving a correlation-length and dynamic critical exponents equal to $\nu = z = 1$ [196].

We will now introduce the dynamic in the Hamiltonian (4.1) by letting $h = h(t)$ change linearly in time, from an initial value h_i to a final one h_f :

$$h(t) = h_i + \text{sgn}(h_f - h_i) \frac{t}{\tau} \quad (4.2)$$

where τ is the time scale (the inverse of the velocity) of the ramping and $0 < t < t_f$, with $t_f = |h_f - h_i|\tau$. The dynamics of the model is also exactly accessible [197, 198], as we will describe in the following.

We are interested in the evolution of bipartite quantities moving from the paramagnetic $h_i > 1$ to the ferromagnetic regime $h_f < 1$. This setting, where one changes one of the parameters in system making it crossing a phase transition, is the natural frameworks for studying the Kibble-Zurek mechanism.

In the following we will study a chain with $L = 50$ sites (we discuss the of size-effects in Sec.4.3) and a ramping from $h_i = 1.4$ to $h_f = 0.4$.

In the following we will consider as bipartite quantities the entanglement entropy (see also Sec.2.3.2) and the entanglement spectrum [199]. We start considering a chain with L sites composed by two equal subsystems A and B , containing each $l = L/2$ adjacent sites. The reduced density matrix $\rho_A(t)$ of the subsystem A at a time t , is obtained evolving in time with the Hamiltonian (4.1) the pure density matrix of the ground state $|GS(t)\rangle$, and tracing out the degrees of freedom of other half B :

$$\rho_A(t) = \text{Tr}_B |GS(t)\rangle \langle GS(t)| \quad (4.3)$$

We can define the entanglement Hamiltonian \mathcal{H} of $\rho_A(t)$ as $\rho_A(t) = e^{-\mathcal{H}(t)}$. We will call its energy spectrum the entanglement spectrum (ES). From the eigenvalues of $\rho_A(t)$ we can also compute the von Neumann entropy of the subsystem

$$S_{L/2}(t) = -\text{Tr} \rho_A(t) \log_2 \rho_A(t) \quad (4.4)$$

The data we present in the following sections are obtained by a bipartition

of the system in two halves but we also checked that our main findings don't depend qualitatively on this particular choice.

We now move to study of the dynamics as ruled by the Hamiltonian (4.1). We follow the procedure of Ref.[200]. The Hamiltonian can be recast, after a Jordan-Wigner transformation (see appendix 4.A), in a fermionic language:

$$H = -\frac{1}{2} \sum_{j=1}^L \left[\left(c_{j+1}^\dagger c_j + c_{j+1} c_j + \text{h.c.} \right) - 2h c_j^\dagger c_j \right] - \frac{Lh}{2} \quad (4.5)$$

The time evolution of the system in Eq.(4.1) is described by the Heisenberg equation for the c operators:

$$i \frac{d}{dt} c_{j,H}(t) = [c_{j,H}(t), H_{j,H}(t)] \quad (4.6)$$

which can be rewritten as:

$$i \frac{d}{dt} c_{j,H}(t) = \sum_{k=1}^L \left[A_{jk}(t) c_{k,H}(t) + B_{jk}(t) c_{k,H}^\dagger(t) \right] \quad (4.7)$$

with

$$\begin{aligned} A_{jk}(t) &\equiv h(t) \delta_{jk} - \frac{1}{2} (\delta_{j,k+1} + \delta_{j+1,k} - \delta_{j1} \delta_{kL} - \delta_{jL} \delta_{k1}) \\ B_{jk}(t) &\equiv -\frac{1}{2} (\delta_{j+1,k} - \delta_{j,k+1} + \delta_{j1} \delta_{kL} - \delta_{jL} \delta_{k1}) \end{aligned} \quad (4.8)$$

In order to solve such an equation, we make the following ansatz, known as *time-dependent Bogolyubov transformation*:

$$c_{j,H}(t) \equiv \sum_{m=0}^{L-1} \left[u_{jm}(t) b_m + v_{jm}^*(t) b_m^\dagger \right] \quad (4.9)$$

with the initial conditions $u_{jm}(0) = u_{jm}$ and $v_{jm}(0) = v_{jm}$ given by the exact solution:

$$\begin{aligned} u_{jm} &\equiv \frac{1}{\sqrt{L}} e^{i(p_m j + \frac{\pi}{4})} u_m, \\ v_{jm} &\equiv \frac{1}{\sqrt{L}} e^{i(p_m j + \frac{\pi}{4})} v_m \end{aligned} \quad (4.10)$$

By putting the ansatz of Eq. (4.9) in the Heisenberg equation, we come to the set of linear coupled ODE's

$$\begin{aligned} i \frac{d}{dt} u_{jm}(t) &= \sum_{k=1}^L [A_{jk}(t) u_{km}(t) + B_{jk}(t) v_{km}(t)] \\ -i \frac{d}{dt} v_{jm}(t) &= \sum_{k=1}^L [B_{jk}(t) u_{km}(t) + A_{jk}(t) v_{km}(t)] \end{aligned} \quad (4.11)$$

Those equations, that can be solved by standard numerical techniques give us $c_j(t)$, it is then possible to construct the correlation matrices and to compute the entanglement spectrum as described in Appendix 4.C.

4.2 Entanglement Dynamics

In this section we will study in details the dynamics of the entanglement spectrum and of the entanglement entropy. Their main results are summarized in (Figs. 4.1 and 4.2). Studying we identify four regimes Since their time evolution in time have different behaviors depending varying the parameter τ we divided it in four regimes. An adiabatic regime with $\tau \sim 500$, a slow regime $\tau \geq 20$, a fast regime $1 \leq \tau \leq 20$ and a sudden one $\tau \leq 1$.

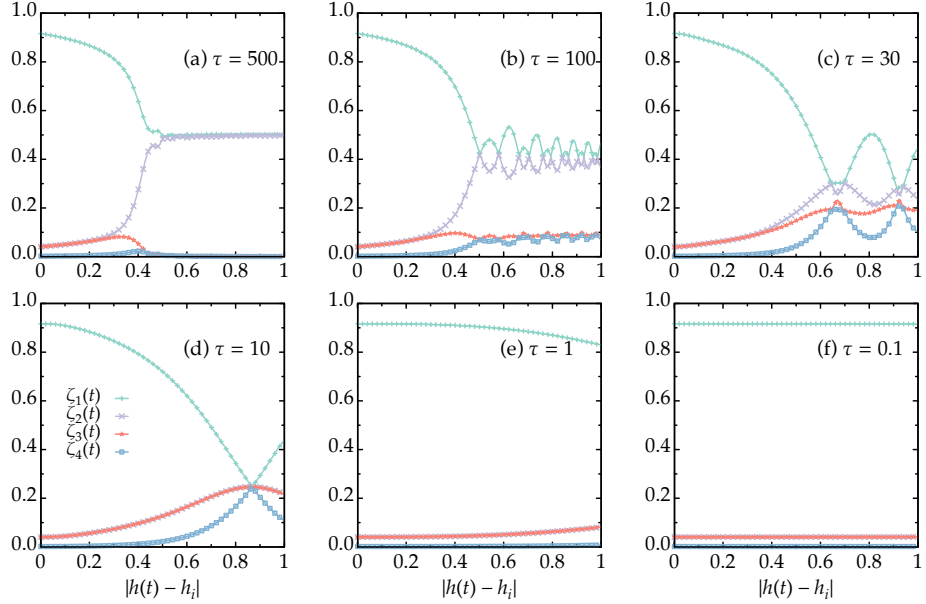


Figure 4.1: Dynamics of the first four eigenvalues of $\rho_A(t)$ for $L = 50$, $h_i = 1.4$ and $h_f = 0.4$. Different panels refer to different τ . In panels (d), (e) and (f) the red and green lines overlay.

4.2.1 Adiabatic and sudden regimes

We begin by considering very large values of τ , i.e., a quasi-adiabatic quench, see for example the curve at $\tau = 500$ of Fig. 4.2 and panel (a) of Fig. 4.1. We observe that during the evolution the entanglement entropy and the entanglement spectrum closely follow the *static* values, i.e., those obtained

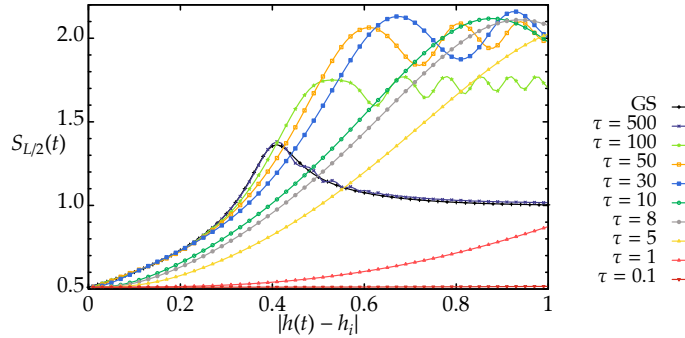


Figure 4.2: Dynamics of the entanglement entropy $S_{L/2}(t)$ for $L = 50$, $h_i = 1.4$, $h_f = 0.4$ for different values of τ .

from the ground state of the system at each value of $h(t)$, the only difference being represented by some small oscillations, that will be discussed in Sec.4.2.3. This behavior is expected from the adiabatic theorem[187] and as a consequence of the finite size of the system. In fact the energy gap closes as a function of the inverse size, remaining non-zero for any finite L , so that in this case it is always possible to reach the adiabatic limit provided τ is large enough (see also Sec.4.3). More precisely, as shown by Cincio et al. in Ref.[201], the probability of having an adiabatic evolution at size L is given by $P(\tau) = 1 - \exp(-2\pi^3\tau/L^2)$, so that the maximum rate ($\sim 1/\tau$) at which the evolution is adiabatic decays as $1/L^2$.

We then consider the opposite regime, with very small values of τ , i.e., very fast quenches (curve with $\tau = 0.1$ in Fig. 4.2) and panel (f) of Fig. 4.1. The entanglement entropy and the entanglement spectrum do not evolve at all, as expected from the adiabatic theorem, independently on the size of the system.

4.2.2 Fast sweeps

We consider now rampings that are slower than sudden ones, but much faster than adiabatic ones; we call them *fast sweeps*, and, for our system sizes, they correspond to $\tau = 1 \div 20$. For the sake of clarity, for both the entanglement entropy and the entanglement spectrum it is useful first to consider the faster regime $\tau \sim 1$ and then slower rampings $\tau \sim 10 \div 20$.

Starting from faster rampings (see curves with $\tau = 1$ and 5 in the main panel of Fig. 4.2), the entanglement entropy increases linearly in the region close to the phase transition: this behavior can be related to the results of Calabrese and Cardy [122] relative to a sudden quench to a conformal critical point where the entanglement entropy is predicted to grow linearly, with a slope related to the central charge of the underlying conformal field theory.

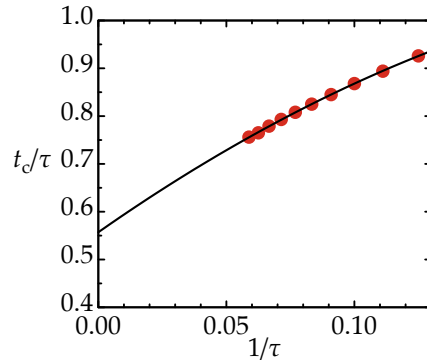


Figure 4.3: The plot shows the time at which the eigenvalues of the reduced density matrix cross as a function of $1/\tau$, for $8 < \tau < 17$. This time results to be always larger than the critical one, meaning that the oscillations start only after the system has reached the critical point. Red crosses: numerical data. Black line: fitting formula $a_0 + a_1/\tau + a_2/\tau^2$, giving $a_0 = 0.557$ (critical point: 0.4).

In our case the quench is not sudden but since the correlation length and relaxation time are large the system behaves as critical for a finite interval of h , and the same picture of the sudden quench can therefore be applied. The behavior of the entanglement spectrum is related to the one of the entanglement entropy and is shown in panel (e) of Fig. 4.1. In this regime of τ , the first eigenvalue decreases, while the remaining three increase: this results in a growth of the entanglement entropy that we observe [199]. Remarkably, the second and third eigenvalues of the reduced density matrix remain degenerate even during this kind of evolution: indeed, these eigenvalues correspond, at $t = 0$, to the eigenstates $|1\rangle$ and $|L/2\rangle$ (see Sec.4.B), and the time evolution, as shown by a perturbative analysis (that we are not going to report), does not break this degeneracy, at least for these values of τ .

The second regime is encountered by further increasing τ (see for example curves with $\tau = 8, 10$ and 30 in Fig. 4.2). In such cases, the entanglement entropy still presents a linear-growth region, which does not last to the end of the sweep, ending in an oscillatory region, in which the entanglement entropy alternates between maxima and minima, with variable frequency. This behavior has already been observed in a thermodynamic-limit study of the dynamics of entanglement entropy [202], and has been ascribed to the fact that the system ends up, after passing the critical point, in a superposition of excited states of the instantaneous Hamiltonian.

We now investigate the behavior of the entanglement spectrum in this regime. As shown in Fig. 4.1(d), the decreasing of the first eigenvalue and the growth of the remaining ones continues until they cross, all at the same point. Moreover, this crossing structure recurs also for later times in an almost periodic

pattern (not shown). This behavior is very peculiar, and we shall investigate it in detail. First of all, it must be noticed that the crossings correspond, as expected, to the maxima of entanglement entropy and that this oscillatory behavior starts only after the system has crossed the critical point. This fact is easily confirmed by plotting the crossing time t_{cr} as a function of τ : the result is shown in Fig. 4.3: the data can be fitted by a power-law $a_0 + a_1/\tau + a_2/\tau^2$ showing that, for $\tau \rightarrow \infty$, the crossing point converges with good precision to the critical point. Strictly speaking, we could not take the limit $\tau \rightarrow \infty$, since, for larger τ , the behavior of the system tends to become adiabatic; however, this extrapolation shows that the oscillations, also present for larger τ , always have the same nature; see Sec.4.2.3. We have also verified that the crossing time t_{cr} does not depend on the size of the system at fixed τ (not shown): this fact represents a further evidence of the fact that the physics, for these values of τ , coincides with the thermodynamic-limit one.

4.2.3 Slow sweeps

The last regime is observed for $\tau \gtrsim 20$. As Figure 4.1(c) shows, the second and the third eigenvalues of the entanglement spectrum begin to separate, making the crossing of $\zeta_1(t)$ and $\zeta_4(t)$ an avoided crossing. For larger values of τ , as shown in figure 4.1(b), this separation continues and the dynamical structure of the spectrum gets closer to the static one, i.e. the one of figure 4.1(a).

Moreover the crossings, occurring between the $\zeta_1(t)$ and $\zeta_2(t)$ and between $\zeta_3(t)$ and $\zeta_4(t)$, take place at the same times for the first and the second couple. On the other hand, the entanglement entropy, as shown in the main panel of Figure 4.2 (curve with $\tau = 100$), at the beginning of the evolution is practically coincident with the static one, and at a certain point begins to grow and to oscillate around a value smaller than the ones of section 4.2.2 and decreasing as τ increases. The behavior of the entanglement spectrum and the entanglement entropy can be ascribed to the approaching of the adiabatic regime. However, as already observed in section 4.2.1, the oscillation (now between the first and the second two eigenvalues) studied in section 4.2.2 survive as a sign of non-adiabaticity.

4.3 Kibble-Zurek Physics

In this section, we discuss the Kibble-Zurek scaling[85–88] of two quantities, i.e., the already considered entanglement entropy and the Schmidt gap[192–194], i.e., the difference between the two largest eigenvalues in the entanglement spectrum. A discussion of this mechanism for the XY -model may be found in Refs.[89, 203–205].

In its original formulation, the Kibble-Zurek mechanism is able, on the

basis of extremely simple approximations, to predict the scaling of the number of topological defects produced after the dynamical transition of a critical point. The key assumption underlying the mechanism is that the evolution can be divided, for suitable ramping velocities, into three parts: a first *adiabatic* one, where the wave function of the system coincides with the ground state of $H(t)$; a second *impulsive*, where the wave function of the system is practically frozen, due to the large relaxation time close to the critical point; a third adiabatic one, as the system is driven away from the critical point [89]. This division takes the name of *adiabatic-impulse-adiabatic* approximation [206, 207]. What plays a role in this kind of mechanism is the *correlation length* $\hat{\xi}$ at the times of passage between the different regimes, that can be seen to scale, for a linear quench of inverse velocity τ , as [87, 88]

$$\hat{\xi} \approx \tau^{\frac{\nu}{1+z\nu}} \quad (4.12)$$

being ν and z the critical exponents of the crossed quantum critical point [196].

4.3.1 Entanglement entropy

Any quantity that is directly related to the correlation length is suitable to a Kibble-Zurek analysis. In particular, close to a conformal critical point described by a conformal charge c , the entanglement entropy has been shown by Calabrese and Cardy to scale as [208]:

$$S = \frac{c}{6} \log_2 \xi + \text{const.} \quad (4.13)$$

We can easily see that the entanglement entropy after the quench scale as [202]

$$S = \frac{c\nu}{6(1+z\nu)} \log_2 \tau + \text{const.} \quad (4.14)$$

The prefactor of the logarithm would be $1/24$, since in the Ising case $\nu = z = 1$ and $c = 1/2$, but as the subsystem A has two boundaries we need to double the prefactor of the logarithm. So we expected the entropy to scale as [201, 208]

$$S_{L/2}(\tau) = \frac{1}{12} \log_2 \tau + \text{const.} \quad (4.15)$$

This clearly holds in the thermodynamic limit, where the gap is strictly closed at the critical point. For finite size systems we expect some deviations from the Kibble-Zurek behavior for large τ . We plot the results we obtain in Fig. 4.1: as expected, we observe a progressive breakdown of the Kibble-Zurek prediction lowering L . A few other remarks are in order: first,

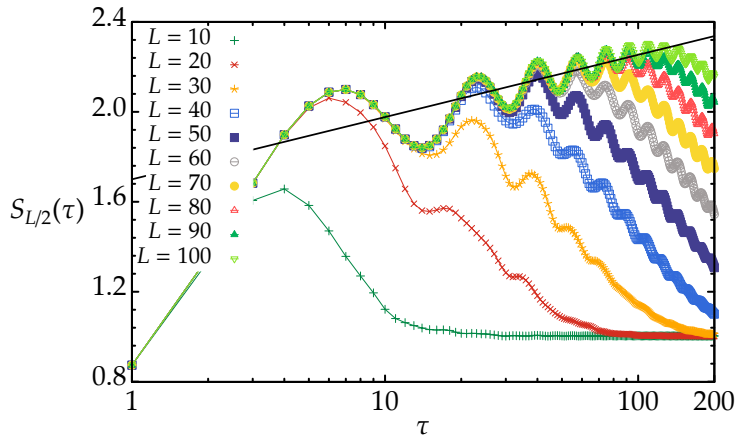


Figure 4.1: Entanglement entropy at the final instant of the evolution for $1 < \tau < 200$ at different system sizes ($10 \leq L \leq 100$, from top to bottom). The equation of the black line is $\text{const.} + (\log_2 \tau)/12$.

Eq. 4.13 has to be modified, since, because of its finite size, subsystem A possesses two boundaries; therefore, Eq. 4.13 is modified by doubling the prefactor of the logarithm[208] (see also Ref. [201]). Moreover, it is evident that the logarithmic behavior expected from the Kibble-Zurek mechanism is superimposed to an oscillating behavior, as already observed in Ref. [202]: it is clearly a reflex of the oscillating structure of the entanglement entropy as a function of time, studied in Sec. 4.2.2 and 4.2.3. Third, we observe that, for small values of τ , the curves at different sizes are practically coincident. This coincidence is lost for larger values of τ 's, depending on L : the velocities at which this coincidence is observed are the ones at which the physics is practically the one of the thermodynamic limit. For example, at $L = 50$, the physics is practically the thermodynamic limit one up to $\tau \approx 15$.

Finally, we note that, remarkably, the τ 's that correspond to the passage from the fast to the slow regime (the τ 's for which the crossing between the first and the fourth eigenvalue of the reduced density matrix begin to disappear), correspond to the breakdown of the Kibble-Zurek, or, equivalently, thermodynamic-limit physics. This fact could be verified by a direct thermodynamic-limit investigation (as, e.g., in Ref. [202]), and could represent, in principle, a very simple tool to check the equivalence between finite-size and thermodynamic-limit physics.

4.3.2 Schmidt gap

As already mentioned above, the Schmidt gap Δ_S is defined as the difference between the two highest eigenvalues of the reduced density matrix. It has been very recently shown [192, 193] to be related to the correlation length

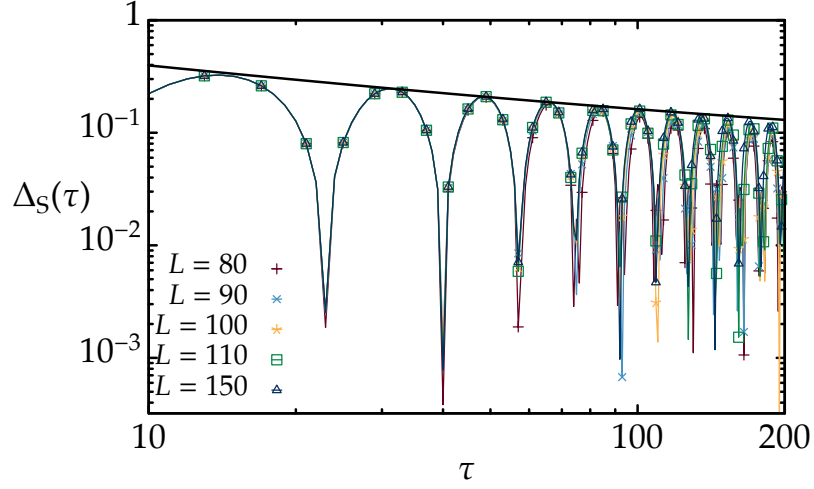


Figure 4.2: Schmidt gap at the final instant of the evolution for $10 < \tau < 200$ at different system sizes ($80 \leq L \leq 150$, from top to bottom). The equation of the black line is $\text{const.} + \tau^{-1/2}$.

i.e.,

$$\Delta_S \approx \xi^{-z} \quad (4.16)$$

From this relation we can obtain its Kibble-Zurek scaling

$$\Delta_S \approx \tau^{-\frac{z\nu}{1+z\nu}} \quad (4.17)$$

In Fig. 4.2 we present the data for the scaling of the Schmidt gap at the end of the ramping as a function of τ .

In Fig. 4.2 we show the numerical results for the scaling of the Schmidt gap at the end of the ramping as a function of τ . We fitted the maxima with the function $\Delta_S = \tau^{-1/2} + \text{const}$ that a surprisingly good agreement with data. For fixed L , the shape of each curve shows cusps as a function of τ . These non-analyticities correspond are a consequence of the crossing of the eigenvalues of the reduced density matrix. Thus, as for the entanglement entropy, we found also eq. (4.17) to be compatible with the numerical results.

4.4 Conclusions

In this chapter we have examined the dynamical evolution of the quantum Ising chain in a transverse magnetic field crossing a quantum phase transition. In particular we analyzed, during the dynamics, the behavior of both

the entanglement entropy and the entanglement spectrum, in particular in the case of a ramping from the paramagnetic to the ferromagnetic phase. For different values of the time scale τ we observed qualitatively different regimes: an adiabatic one (large τ) when the system evolves according to the instantaneous ground state, a sudden quench (small τ) when the system is essentially frozen to its initial state and an intermediate one. In the latter the entropy starts growing linearly in time and then displays oscillations in correspondence with the level crossing happening in the entanglement spectrum. The entanglement spectrum can be also used for studying both universal quantities (scaling exponents) and physical phenomena, such as the Kibble-Zurek mechanism, that may manifest during the evolution.

We may conclude that entanglement entropy and entanglement spectrum seem to be, for the dynamical evolution as in the static case, a powerful tool to investigate the physics of a closed quantum many body system crossing a phase transition at $T = 0$.

Appendices

4.A Exact solution of the Ising model

In this Appendix we show how to diagonalize the Hamiltonian in Eq. 4.1. We follow Ref.[82] quite closely.

By defining the raising and lowering operators $\sigma_j^\pm \equiv (\sigma_j^z \mp i\sigma_j^y)/2$, Eq. 4.1 reads:

$$H = -\frac{1}{2} \sum_{j=1}^L \left[(\sigma_j^+ \sigma_{j+1}^+ + \sigma_j^+ \sigma_{j+1}^- + \text{h.c.}) + 2h\sigma_j^+ \sigma_j^- \right] + \frac{Lh}{2} \quad (4.18)$$

Performing a Jordan-Wigner transformation by means of

$$\begin{aligned} c_j &\equiv \prod_{k=1}^{j-1} (2\sigma_k^+ \sigma_k^- - 1) \sigma_j^+ \\ c_j^\dagger &\equiv \sigma_j^- \prod_{k=1}^{j-1} (2\sigma_k^+ \sigma_k^- - 1) \end{aligned} \quad (4.19)$$

allows to rewrite the Hamiltonian Eq. 4.18 in fermionic form:

$$\begin{aligned} H &= -\frac{1}{2} \sum_{j=1}^{L-1} \left[c_{j+1}^\dagger c_j + c_{j+1} c_j + \text{h.c.} \right] + \\ &+ \frac{\alpha}{2} \left[c_1^\dagger c_L + c_1 c_L + \text{h.c.} \right] + h \sum_{j=1}^L c_j^\dagger c_j - \frac{Lh}{2} \end{aligned} \quad (4.20)$$

where $\alpha \equiv \prod_{j=1}^L (1 - 2c_j^\dagger c_j) = \prod_{j=1}^L \sigma_j^x$. It is easy to show that α commutes with H , and therefore it is a constant of motion; moreover, $\alpha^2 = 1$, so that $\alpha = \pm 1$. As it is manifest from its definition, the case $\alpha = \pm 1$ corresponds to the case in which in the chain has an even/odd number of down spins is present, and, in fermionic language, to a chain with antiperiodic/periodic boundary conditions (APBC/PBC) and an even/odd number of fermions. We choose to work in the sector of even parity in the number fermions, i.e. $\alpha = 1$, being, at finite size, the ground state of the model always in this sector. One ends up with

$$H = -\frac{1}{2} \sum_{j=1}^L \left[(c_{j+1}^\dagger c_j + c_{j+1} c_j + \text{h.c.}) - 2hc_j^\dagger c_j \right] - \frac{Lh}{2} \quad (4.21)$$

with fermions satisfying APBC. The diagonalization proceeds by means of a Fourier transform

$$c_j \equiv \frac{e^{i\pi/4}}{\sqrt{L}} \sum_{m=0}^{L-1} e^{ip_m j} d_m, \quad (4.22)$$

with $p_m \equiv 2\pi(m+1/2)/L$, in order to automatically implement the APBC. With some algebra, it is possible to show that the Hamiltonian takes the form

$$H = \frac{1}{2} \sum_{m=0}^{L-1} \left(d_m^\dagger, d_{L-m-1} \right) M_m \begin{pmatrix} d_m \\ d_{L-m-1}^\dagger \end{pmatrix} \quad (4.23)$$

with

$$M_m \equiv \begin{pmatrix} A_m & -B_m \\ -B_m & -A_m \end{pmatrix} \quad (4.24)$$

and

$$A_m \equiv h - \cos p_m, \quad B_m \equiv \sin p_m \quad (4.25)$$

that, remarkably, satisfy $A_{L-m-1} = A_m$, $B_{L-m-1} = -B_m$, i.e., the Hamiltonian decouples into the sum of L non-interacting modes, each one independently diagonalizable.

The last step of the procedure consists of a Bogolyubov transformation, which puts each M_m in diagonal form. The eigenvalues of each M_m are given by the two values $\pm E_m$, with

$$E_m = \sqrt{A_m^2 + B_m^2} \quad (4.26)$$

and the orthogonal transformation U_m making M_m diagonal, i.e., giving $U_m^\dagger M_m U_m = \text{diag}(E_m, -E_m)$, is given by

$$U_m \equiv \begin{pmatrix} u_m & v_m \\ -v_m & u_m \end{pmatrix} \quad (4.27)$$

where

$$u_m = \frac{-(-1)^m \frac{A_m + E_m}{B_m}}{\sqrt{1 + \left(\frac{A_m + E_m}{B_m}\right)^2}}, \quad v_m = \frac{-(-1)^m}{\sqrt{1 + \left(\frac{A_m + E_m}{B_m}\right)^2}} \quad (4.28)$$

satisfying $u_{L-m-1} = u_m$, $v_{L-m-1} = -v_m$. The diagonalizing operators are

$$\begin{pmatrix} b_m \\ b_{L-m-1}^\dagger \end{pmatrix} \equiv U_m \begin{pmatrix} d_m \\ d_{L-m-1}^\dagger \end{pmatrix} \quad (4.29)$$

and the orthogonality of U_m ensures their fermionic nature. The Hamiltonian takes, by means of the inverse of Eq. 4.29, the final form

$$H = \sum_{m=0}^{L-1} E_m \left(b_m^\dagger b_m - \frac{1}{2} \right) \quad (4.30)$$

and its ground state is, for $\alpha = 1$, the vacuum state $|GS\rangle$ such that $b_m |GS\rangle = 0$. Excited states, in the APBC sector, are obtained by applying couples of Bogolyubov creation operators on $|GS\rangle$.

4.B Initial structure of the entanglement spectrum

In this section we compute the reduced density matrix for the ground state of the Ising model (4.1) at $t = 0$ in the limit $h(0) = h \rightarrow \infty$. The ground state of the system is

$$|0\rangle = |\uparrow\rangle_1 |\uparrow\rangle_2 \cdots |\uparrow\rangle_L \quad (4.31)$$

where $|\uparrow\rangle_j$ and $|\downarrow\rangle_j$ are the eigenstates of σ_j^z .

This is not the exact ground state for $h \gg 1$, but, at first order in perturbation theory, it is easy to show that the latter is given by

$$|GS\rangle = \mathcal{N} \left[|0\rangle + \frac{1}{4h} \sum_{j=1}^L |j, j+1\rangle \right] \quad (4.32)$$

with

$$|j, j+1\rangle = |\uparrow\rangle_1 |\uparrow\rangle_2 \cdots |\downarrow\rangle_j |\downarrow\rangle_{j+1} \cdots |\uparrow\rangle_{L-1} |\uparrow\rangle_L \quad (4.33)$$

being the state where the spins at sites j and $j+1$ are flipped and $\mathcal{N} = \left(1 + \frac{L}{16h^2}\right)^{-\frac{1}{2}}$ is a normalization factor.

The zero-temperature density matrix of the system is given by $|GS\rangle \langle GS|$ and the reduced density matrix ρ_A of the half chain $A = \{1, \dots, L/2\}$ takes the form

$$\rho_A = (|0\rangle_A, |2p\rangle_A, |1\rangle_A, |L/2\rangle_A) \mathbb{R}_A \begin{pmatrix} {}_A \langle 0| \\ {}_A \langle 2p| \\ {}_A \langle 1| \\ {}_A \langle L/2| \end{pmatrix} \quad (4.34)$$

with

$$|0\rangle_A = |\uparrow\rangle_1 |\uparrow\rangle_2 \cdots |\uparrow\rangle_{L/2} \quad (4.35)$$

$$|2p\rangle_A = \left(\frac{L}{2} - 1\right)^{-\frac{1}{2}} \sum_{j=1}^{\frac{L}{2}-1} |j, j+1\rangle \quad (4.36)$$

$$|1\rangle_A = |\downarrow\rangle_1 |\uparrow\rangle_2 \cdots |\uparrow\rangle_L \quad (4.37)$$

$$|L/2\rangle_A = |\uparrow\rangle_1 |\uparrow\rangle_2 \cdots |\uparrow\rangle_{L/2-1} |\downarrow\rangle_{L/2} \quad (4.38)$$

and

$$\mathbb{R}_A = \mathcal{N}^2 \begin{pmatrix} 1 + \frac{\frac{L}{2}-1}{16h^2} & \frac{\sqrt{\frac{L}{2}-1}}{4h} & 0 & 0 \\ \frac{\sqrt{\frac{L}{2}-1}}{4h} & \frac{\frac{L}{2}-1}{16h^2} & 0 & 0 \\ 0 & 0 & \frac{1}{16h^2} & 0 \\ 0 & 0 & 0 & \frac{1}{16h^2} \end{pmatrix} \quad (4.39)$$

\mathbb{R}_A shows that $|1\rangle_A$ and $|L/2\rangle_A$ are degenerate eigenstates of ρ_A with eigenvalues

$$\zeta_{2,3} = \frac{1}{2\ell + 16h^2} \quad (4.40)$$

with $\ell = L/2$.

Diagonalizing the remaining block gives the others two eigenvalues

$$\zeta_{1,4} = \frac{(\ell - 1)/2 + 4h^2 \pm 2\sqrt{h^2(\ell + 4h^2 - 1)}}{\ell + 8h^2}. \quad (4.41)$$

For large enough h , the two eigenstates related to $\zeta_{1,4}$ are superpositions of $|0\rangle_A$ and $|2p\rangle_A$, one in which the paramagnetic state $|0\rangle_A$ dominates and the other in which $|2p\rangle_A$ dominates. A numerical analysis shows also that $\zeta_1 < \zeta_2 = \zeta_3 < \zeta_4$, for sufficiently high h .

4.C Bipartite quantities in free fermionic systems

In this Appendix we review to compute the entanglement entropy and the entanglement spectrum for free fermionic system.

As it is known from recent literature [209, 210] (see also Refs.[185, 211]), for fermionic biquadratic (static) Hamiltonians the density matrix can be obtained from correlation functions. In order to evaluate the time evolution of the entanglement entropy and spectrum we need a step forward, which is the introduction of Majorana fermions:

$$\bar{c}_{2m-1} = c_m^\dagger + c_m \quad (4.42)$$

$$\bar{c}_{2m} = i(c_m^\dagger - c_m) \quad (4.43)$$

which satisfy anticommutation rules $\{\bar{c}_r, \bar{c}_s\} = 2\delta_{rs}$. The correlation matrix of the Majorana fermions has the form:

$$\langle \bar{c}_r \bar{c}_s \rangle = \delta_{r,s} + i\Gamma_{rs} \quad (4.44)$$

where $r, s = 1, \dots, 2\ell$. The matrix Γ_{rs} is antisymmetric and its eigenvalues are purely imaginary $\pm i\nu_r$, $r = 1, \ell$. It can be shown that this matrix describes a set of uncorrelated (true) fermions $\{a_m\}$ satisfying:

$$\langle a_m a_n \rangle = 0, \quad \langle a_m^\dagger a_n \rangle = \delta_{mn} \frac{1 + \nu_n}{2}. \quad (4.45)$$

Each of the ℓ blocks is then in the state $\rho_j = p_j a_j^\dagger |0\rangle \langle 0| a_j + (1 - p_j) |0\rangle \langle 0|$, with $p_j = (1 + \nu_j)/2$ so that the entropy is the sum of the single-particle entropies, thus yielding for the reduced ℓ -site system:

$$S(\ell) = \sum_{j=1}^{\ell} H_2 \left(\frac{1 + \nu_j}{2} \right), \quad (4.46)$$

where $H_2(x) \equiv -x \log_2 x - (1-x) \log_2(1-x)$. The eigenvalues λ_j , $j = 1, \dots, 2^\ell$ of the reduced density matrix can in principle be found by taking properly chosen products of either p_j or $(1-p_j)$, with $j = 1, \dots, \ell$ [212].

The procedure described above works equally well for the time-dependent case, provided that the Majorana fermions are constructed using the time-evolved true fermions $c_{i,H}(t)$. In this way we can obtain the time-dependent entropy $S(\ell, t)$ and entanglement spectrum $\lambda_i(\ell, t)$.

Ringrazio i miei relatori sia di Bologna, prof.ssa Elisa Ercolessi e prof. Fabio Ortolani, che di Lione, prof. Tommaso Roskilde, per tutte le opportunità di crescita che mi sono state concesse e per la completa disponibilità che avete avuto nei miei confronti.

Ringrazio Luca e Davide per avere condiviso con me questi ultimi tre anni tra uffici sporchi, cene sociali, improperi e, a volte, fisica. C'è molto di più di voi in questa tesi che un solo ringraziamento.

Ringrazio Adam, Thibaud, Laurent, Irénée e Daniele per avermi accolto come una famiglia nel laboratorio di Lione.

Ringrazio tutti i miei amici, la mia famiglia, e tutte le persone che mi sono state vicine in questi tre anni pieni di peripezie.

Un ringraziamento speciale va Marina. Se in quest'ultimo anno non avessi avuto tu accanto non sarei qui adesso.

Grazie milleeee ad Elena, che anche se lei non lo sa, mi è sempre stata molto vicina facendomi sentire tranquillo. Grazie di cuore.

Bibliography

- [1] T. Kinoshita, T. Wenger, and D. S. Weiss, *Nature* **440**, 900 (2006).
- [2] A. A. Houck, H. E. Tureci, and J. Koch, *Nat Phys* **8**, 292 (2012).
- [3] R. Blatt and C. F. Roos, *Nat Phys* **8**, 277 (2012).
- [4] I. Bloch, J. Dalibard, and S. Nascimbene, *Nat Phys* **8**, 267 (2012).
- [5] J. I. Cirac and P. Zoller, *Nat Phys* **8**, 264 (2012).
- [6] A. Aspuru-Guzik and P. Walther, *Nat Phys* **8**, 285 (2012).
- [7] A. Trabesinger, *Nat Phys* **8**, 263 (2012).
- [8] A. Polkovnikov, K. Sengupta, A. Silva, and M. Vengalattore, *Rev. Mod. Phys.* **83**, 863 (2011).
- [9] J. M. Deutsch, *Phys. Rev. A* **43**, 2046 (1991).
- [10] M. Srednicki, *Phys. Rev. E* **50**, 888 (1994).
- [11] M. Rigol, V. Dunjko, and M. Olshanii, *Nature* **452**, 854 (2008).
- [12] A. C. idy, C. W. Clark, and M. Rigol, *Phys. Rev. Lett.* **106**, 140405 (2011).
- [13] J.-S. Caux and F. H. L. Essler, *Phys. Rev. Lett.* **110**, 257203 (2013).
- [14] P. W. Anderson, *Phys. Rev.* **109**, 1492 (1958).
- [15] G. Roati, C. D'Errico, L. Fallani, M. Fattori, C. Fort, M. Zaccanti, G. Modugno, M. Modugno, and M. Inguscio, *Nature* **453**, 895 (2008).
- [16] J. Billy, V. Josse, Z. Zuo, A. Bernard, B. Hambrecht, P. Lugan, D. Clement, L. Sanchez-Palencia, P. Bouyer, and A. Aspect, *Nature* **453**, 891 (2008).
- [17] L. Fleishman and P. W. Anderson, *Phys. Rev. B* **21**, 2366 (1980).
- [18] R. Nandkishore and D. A. Huse, *Annual Review of Condensed Matter Physics* **6**, 15 (2015), <http://dx.doi.org/10.1146/annurev-conmatphys-031214-014726> .

-
- [19] D. Basko, I. Aleiner, and B. Altshuler, *Annals of Physics* **321**, 1126 (2006).
- [20] B. L. Altshuler, Y. Gefen, A. Kamenev, and L. S. Levitov, *Phys. Rev. Lett.* **78**, 2803 (1997).
- [21] I. V. Gornyi, A. D. Mirlin, and D. G. Polyakov, *Phys. Rev. Lett.* **95**, 206603 (2005).
- [22] V. Oganesyan and D. A. Huse, *Phys. Rev. B* **75**, 155111 (2007).
- [23] M. Žnidarič, T. c. v. Prosen, and P. Prelovšek, *Phys. Rev. B* **77**, 064426 (2008).
- [24] A. Pal and D. A. Huse, *Phys. Rev. B* **82**, 174411 (2010).
- [25] M. Serbyn and J. E. Moore, ArXiv e-prints (2015), [arXiv:1508.07293](https://arxiv.org/abs/1508.07293) [[cond-mat.dis-nn](#)] .
- [26] D. J. Luitz, N. Laflorencie, and F. Alet, *Phys. Rev. B* **91**, 081103 (2015).
- [27] R. Singh, J. H. Bardarson, and F. Pollmann, ArXiv e-prints (2015), [arXiv:1508.05045](https://arxiv.org/abs/1508.05045) [[cond-mat.dis-nn](#)] .
- [28] D. M. Kennes and C. Karrasch, ArXiv e-prints (2015), [arXiv:1511.02205](https://arxiv.org/abs/1511.02205) [[cond-mat.str-el](#)] .
- [29] J. Z. Imbrie, ArXiv e-prints (2014), [arXiv:1403.7837](https://arxiv.org/abs/1403.7837) [[math-ph](#)] .
- [30] M. Schreiber, S. S. Hodgman, P. Bordia, H. P. Lüschen, M. H. Fischer, R. Vosk, E. Altman, U. Schneider, and I. Bloch, *Science* **349**, 842 (2015).
- [31] P. Bordia, H. P. Lüschen, S. S. Hodgman, M. Schreiber, I. Bloch, and U. Schneider, ArXiv e-prints (2015), [arXiv:1509.00478](https://arxiv.org/abs/1509.00478) [[cond-mat.quant-gas](#)] .
- [32] J. Smith, A. Lee, P. Richerme, B. Neyenhuis, P. W. Hess, P. Hauke, M. Heyl, D. A. Huse, and C. Monroe, ArXiv e-prints (2015), [arXiv:1508.07026](https://arxiv.org/abs/1508.07026) [[quant-ph](#)] .
- [33] N. Laflorencie, ArXiv e-prints (2015), [arXiv:1512.03388](https://arxiv.org/abs/1512.03388) [[cond-mat.str-el](#)] .
- [34] J. H. Bardarson, F. Pollmann, and J. E. Moore, *Phys. Rev. Lett.* **109**, 017202 (2012).
- [35] P. G. Harper, *Proceedings of the Physical Society. Section A* **68**, 874 (1955).

-
- [36] S. Aubry and G. André, *Ann. Israel Phys. Soc* **3**, 18 (1980).
- [37] D. J. Thouless, *Phys. Rev. B* **28**, 4272 (1983).
- [38] D. R. Grempel, S. Fishman, and R. E. Prange, *Phys. Rev. Lett.* **49**, 833 (1982).
- [39] R. E. Prange, D. R. Grempel, and S. Fishman, *Phys. Rev. B* **29**, 6500 (1984).
- [40] M. Kohmoto, *Phys. Rev. Lett.* **51**, 1198 (1983).
- [41] M. J. Stephen and E. Akkermans, *Phys. Rev. B* **33**, 3837 (1986).
- [42] M. Modugno, *New Journal of Physics* **11**, 033023 (2009).
- [43] G.-L. Ingold, A. Wobst, C. Aulbach, and P. Hnggi, *The European Physical Journal B - Condensed Matter and Complex Systems* **30**, 175 (2002).
- [44] C. Aulbach, A. Wobst, G.-L. Ingold, P. Hnggi, and I. Varga, *New Journal of Physics* **6**, 70 (2004).
- [45] R. B. Diener, G. A. Georgakis, J. Zhong, M. Raizen, and Q. Niu, *Phys. Rev. A* **64**, 033416 (2001).
- [46] S. Y. Jitomirskaya, *Annals of Mathematics* **150**, 1159 (1999).
- [47] D. J. Boers, B. Goedeke, D. Hinrichs, and M. Holthaus, *Phys. Rev. A* **75**, 063404 (2007).
- [48] L. D. Negro and N.-N. Feng, *Opt. Express* **15**, 14396 (2007).
- [49] J. B. Sokoloff, *Phys. Rev. B* **23**, 6422 (1981).
- [50] J. Sokoloff, *Physics Reports* **126**, 189 (1985).
- [51] M. Y. Azbel, *Phys. Rev. Lett.* **43**, 1954 (1979).
- [52] D. R. Hofstadter, *Phys. Rev. B* **14**, 2239 (1976).
- [53] J. Hebborn and E. Sondheimer, *Journal of Physics and Chemistry of Solids* **13**, 105 (1960).
- [54] S. Ostlund, R. Pandit, D. Rand, H. J. Schellnhuber, and E. D. Siggia, *Phys. Rev. Lett.* **50**, 1873 (1983).
- [55] M. Kohmoto, L. P. Kadanoff, and C. Tang, *Phys. Rev. Lett.* **50**, 1870 (1983).

- [56] Y. E. Kraus, Y. Lahini, Z. Ringel, M. Verbin, and O. Zeitler, *Phys. Rev. Lett.* **109**, 106402 (2012).
- [57] K. A. Madsen, E. J. Bergholtz, and P. W. Brouwer, *Phys. Rev. B* **88**, 125118 (2013).
- [58] F. Liu, S. Ghosh, and Y. D. Chong, *Phys. Rev. B* **91**, 014108 (2015).
- [59] H. L. Cycon, R. G. Froese, W. Kirsch, and B. Simon, *Schrödinger Operators. With Applications to Quantum Mechanics and Global Geometry*, Theoretical and Mathematical Physics, Vol. XI, 329 (Springer-Verlag Berlin Heidelberg, 1987).
- [60] R. Peierls, *Zeitschrift für Physik* **80**, 763 (1933).
- [61] P. Brüesch, S. Strässler, and H. R. Zeller, *Phys. Rev. B* **12**, 219 (1975).
- [62] L. Coleman, M. Cohen, D. Sandman, F. Yamagishi, A. Garito, and A. Heeger, *Solid State Communications* **12**, 1125 (1973).
- [63] R. Spal, C.-E. Chen, A. Denenstien, A. McGhie, A. Heeger, and A. MacDiarmid, *Solid State Communications* **32**, 641 (1979).
- [64] P. M. de Wolff, T. Janssen, and A. Janner, *Acta Crystallographica Section A* **37**, 625 (1981).
- [65] P. M. de Wolff, *Acta Crystallographica Section A* **30**, 777 (1974).
- [66] S. Lellouch, *Collective localization transitions in interacting disordered and quasiperiodic Bose superfluids*, *Theses*, Institut d'Optique Graduate School (2014).
- [67] J. E. Lye, L. Fallani, C. Fort, V. Guarrera, M. Modugno, D. S. Wiersma, and M. Inguscio, *Phys. Rev. A* **75**, 061603 (2007).
- [68] M. H. Anderson, J. R. Ensher, M. R. Matthews, C. E. Wieman, and E. A. Cornell, *Science* **269**, 198 (1995), <http://www.sciencemag.org/content/269/5221/198.full.pdf>.
- [69] C. C. Bradley, C. A. Sackett, J. J. Tollett, and R. G. Hulet, *Phys. Rev. Lett.* **75**, 1687 (1995).
- [70] K. B. Davis, M. O. Mewes, M. R. Andrews, N. J. van Druten, D. S. Durfee, D. M. Kurn, and W. Ketterle, *Phys. Rev. Lett.* **75**, 3969 (1995).
- [71] I. Bloch, J. Dalibard, and W. Zwerger, *Rev. Mod. Phys.* **80**, 885 (2008).

- [72] I. Bloch, J. Dalibard, and S. Nascimbene, *Nat Phys* **8**, 267 (2012).
- [73] M. Rigol and A. Muramatsu, *Phys. Rev. Lett.* **94**, 240403 (2005).
- [74] A. Minguzzi and D. M. Gangardt, *Phys. Rev. Lett.* **94**, 240404 (2005).
- [75] F. Heidrich-Meisner, S. R. Manmana, M. Rigol, A. Muramatsu, A. E. Feiguin, and E. Dagotto, *Phys. Rev. A* **80**, 041603 (2009).
- [76] J. P. Ronzheimer, M. Schreiber, S. Braun, S. S. Hodgman, S. Langer, I. P. McCulloch, F. Heidrich-Meisner, I. Bloch, and U. Schneider, *Phys. Rev. Lett.* **110**, 205301 (2013).
- [77] C. J. Bolech, F. Heidrich-Meisner, S. Langer, I. P. McCulloch, G. Orso, and M. Rigol, *Phys. Rev. Lett.* **109**, 110602 (2012).
- [78] M. Rigol and A. Muramatsu, *Phys. Rev. Lett.* **93**, 230404 (2004).
- [79] K. Rodriguez, S. R. Manmana, M. Rigol, R. M. Noack, and A. Muramatsu, *New Journal of Physics* **8**, 169 (2006).
- [80] E. Lieb, T. Schultz, and D. Mattis, *Annals of Physics* **16**, 407 (1961).
- [81] S. Sachdev, *Quantum Phase Transitions* (Cambridge University Press, 2011).
- [82] F. Franchini, *Notes on Bethe Ansatz Techniques* (Sissa web site, 2011).
- [83] E. H. Lieb and D. W. Robinson, *Comm. Math. Phys.* **28**, 251 (1972).
- [84] P. Calabrese and J. Cardy, *Phys. Rev. Lett.* **96**, 136801 (2006).
- [85] T. W. B. Kibble, *Journal of Physics A: Mathematical and General* **9**, 1387 (1976).
- [86] T. Kibble, *Physics Reports* **67**, 183 (1980).
- [87] W. H. Zurek, *Nature* **317**, 505 (1985).
- [88] W. Zurek, *Physics Reports* **276**, 177 (1996).
- [89] W. H. Zurek, U. Dorner, and P. Zoller, *Phys. Rev. Lett.* **95**, 105701 (2005).
- [90] R. Roth and K. Burnett, *Phys. Rev. A* **68**, 023604 (2003).
- [91] B. Damski, J. Zakrzewski, L. Santos, P. Zoller, and M. Lewenstein, *Phys. Rev. Lett.* **91**, 080403 (2003).
- [92] L. Fallani, J. E. Lye, V. Guarrera, C. Fort, and M. Inguscio, *Phys. Rev. Lett.* **98**, 130404 (2007).

-
- [93] V. Guarrera, L. Fallani, J. E. Lye, C. Fort, and M. Inguscio, *New Journal of Physics* **9**, 107 (2007).
- [94] L. Tanzi, E. Lucioni, S. Chaudhuri, L. Gori, A. Kumar, C. D'Errico, M. Inguscio, and G. Modugno, *Phys. Rev. Lett.* **111**, 115301 (2013).
- [95] B. Kramer and A. MacKinnon, *Reports on Progress in Physics* **56**, 1469 (1993).
- [96] D. J. Thouless, *Journal of Physics C: Solid State Physics* **5**, 77 (1972).
- [97] J. Biddle and S. Das Sarma, *Phys. Rev. Lett.* **104**, 070601 (2010).
- [98] J. Biddle, D. J. Priour, B. Wang, and S. Das Sarma, *Phys. Rev. B* **83**, 075105 (2011).
- [99] T. Roscilde, *Phys. Rev. A* **77**, 063605 (2008).
- [100] J. Bellissard and B. Simon, *Journal of Functional Analysis* **48**, 408 (1982).
- [101] E. Altman and R. Vosk, *Annual Review of Condensed Matter Physics* **6**, 383 (2015), <http://dx.doi.org/10.1146/annurev-conmatphys-031214-014701> .
- [102] L. F. Santos and M. Rigol, *Phys. Rev. E* **82**, 031130 (2010).
- [103] L. F. Santos and M. Rigol, *Phys. Rev. E* **81**, 036206 (2010).
- [104] M. Rigol, *Phys. Rev. A* **80**, 053607 (2009).
- [105] M. Rigol, *Phys. Rev. Lett.* **103**, 100403 (2009).
- [106] M. Srednicki, *Journal of Physics A: Mathematical and General* **32**, 1163 (1999).
- [107] D. C. Brody, D. W. Hook, and L. P. Hughston, *Journal of Physics A: Mathematical and Theoretical* **40**, F503 (2007).
- [108] M. Kollar and M. Eckstein, *Phys. Rev. A* **78**, 013626 (2008).
- [109] T. Vojta, C. Kotabage, and J. A. Hoyos, *Phys. Rev. B* **79**, 024401 (2009).
- [110] P. Ponte, Z. Papić, F. m. c. Huveneers, and D. A. Abanin, *Phys. Rev. Lett.* **114**, 140401 (2015).
- [111] N. Y. Yao, C. R. Laumann, J. I. Cirac, M. D. Lukin, and J. E. Moore, *ArXiv e-prints* (2014), [arXiv:1410.7407 \[cond-mat.dis-nn\]](https://arxiv.org/abs/1410.7407) .

-
- [112] J. Eisert, M. Cramer, and M. B. Plenio, *Rev. Mod. Phys.* **82**, 277 (2010).
- [113] M. Serbyn, Z. Papić, and D. A. Abanin, *Phys. Rev. Lett.* **111**, 127201 (2013).
- [114] M. Serbyn, Z. Papić, and D. A. Abanin, *Phys. Rev. Lett.* **110**, 260601 (2013).
- [115] R. Vosk and E. Altman, *Phys. Rev. Lett.* **110**, 067204 (2013).
- [116] R. Vosk and E. Altman, *Phys. Rev. Lett.* **112**, 217204 (2014).
- [117] B. Bauer and C. Nayak, *Journal of Statistical Mechanics: Theory and Experiment* **2013**, P09005 (2013).
- [118] T. Devakul and R. R. P. Singh, *Phys. Rev. Lett.* **115**, 187201 (2015).
- [119] C. Nadal, S. N. Majumdar, and M. Vergassola, *Phys. Rev. Lett.* **104**, 110501 (2010).
- [120] J. A. Kjäll, J. H. Bardarson, and F. Pollmann, *Phys. Rev. Lett.* **113**, 107204 (2014).
- [121] E. Baygan, S. P. Lim, and D. N. Sheng, *Phys. Rev. B* **92**, 195153 (2015).
- [122] P. Calabrese and J. Cardy, *Journal of Statistical Mechanics: Theory and Experiment* **2005**, P04010 (2005).
- [123] H. Kim and D. A. Huse, *Phys. Rev. Lett.* **111**, 127205 (2013).
- [124] C. K. Burrell and T. J. Osborne, *Phys. Rev. Lett.* **99**, 167201 (2007).
- [125] D. A. Huse, R. Nandkishore, and V. Oganesyan, *Phys. Rev. B* **90**, 174202 (2014).
- [126] D. J. Luitz, N. Laflorencie, and F. Alet, ArXiv e-prints (2015), [arXiv:1511.05141](https://arxiv.org/abs/1511.05141) [cond-mat.dis-nn] .
- [127] A. C. Potter, R. Vasseur, and S. A. Parameswaran, *Phys. Rev. X* **5**, 031033 (2015).
- [128] M. Schiulaz and M. Mller, *AIP Conference Proceedings* **1610**, 11 (2014).
- [129] M. Pino, B. L. Altshuler, and L. B. Ioffe, ArXiv e-prints (2015), [arXiv:1501.03853](https://arxiv.org/abs/1501.03853) [cond-mat.dis-nn] .
- [130] T. Grover and M. P. A. Fisher, *Journal of Statistical Mechanics: Theory and Experiment* **2014**, P10010 (2014).

-
- [131] W. De Roeck and F. m. c. Huveneers, *Phys. Rev. B* **90**, 165137 (2014).
- [132] A. Chandran, C. R. Laumann, and V. Oganesyan, ArXiv e-prints (2015), [arXiv:1509.04285](https://arxiv.org/abs/1509.04285) [cond-mat.dis-nn] .
- [133] T. Grover, ArXiv e-prints (2014), [arXiv:1405.1471](https://arxiv.org/abs/1405.1471) [cond-mat.dis-nn] .
- [134] C. Monthus, ArXiv e-prints (2015), [arXiv:1510.03711](https://arxiv.org/abs/1510.03711) [cond-mat.dis-nn] .
- [135] J. Vidal, D. Mouhanna, and T. Giamarchi, *Phys. Rev. Lett.* **83**, 3908 (1999).
- [136] J. Vidal, D. Mouhanna, and T. Giamarchi, *Phys. Rev. B* **65**, 014201 (2001).
- [137] X. Deng, R. Citro, A. Minguzzi, and E. Orignac, *Phys. Rev. A* **78**, 013625 (2008).
- [138] S. Iyer, V. Oganesyan, G. Refael, and D. A. Huse, *Phys. Rev. B* **87**, 134202 (2013).
- [139] V. P. Michal, B. L. Altshuler, and G. V. Shlyapnikov, *Phys. Rev. Lett.* **113**, 045304 (2014).
- [140] I. Mondragon-Shem and T. L. Hughes, *Phys. Rev. B* **90**, 104204 (2014).
- [141] R. Modak and S. Mukerjee, *Phys. Rev. Lett.* **115**, 230401 (2015).
- [142] X. Li, S. Ganeshan, J. H. Pixley, and S. Das Sarma, *Phys. Rev. Lett.* **115**, 186601 (2015).
- [143] Y. Wang, H. Hu, and S. Chen, ArXiv e-prints (2015), [arXiv:1505.06343](https://arxiv.org/abs/1505.06343) [cond-mat.dis-nn] .
- [144] G. D. Chiara, S. Montangero, P. Calabrese, and R. Fazio, *Journal of Statistical Mechanics: Theory and Experiment* **2006**, P03001 (2006).
- [145] G. Roux, T. Barthel, I. P. McCulloch, C. Kollath, U. Schollwöck, and T. Giamarchi, *Phys. Rev. A* **78**, 023628 (2008).
- [146] M. Serbyn, Z. Papić, and D. A. Abanin, *Phys. Rev. B* **90**, 174302 (2014).
- [147] M. Serbyn, Z. Papić, and D. A. Abanin, *Phys. Rev. X* **5**, 041047 (2015).

-
- [148] I. Mondragon-Shem, A. Pal, T. L. Hughes, and C. R. Laumann, *Phys. Rev. B* **92**, 064203 (2015).
- [149] A. Nanduri, H. Kim, and D. A. Huse, *Phys. Rev. B* **90**, 064201 (2014).
- [150] S. P. Lim and D. N. Sheng, ArXiv e-prints (2015), [arXiv:1510.08145 \[cond-mat.str-el\]](#) .
- [151] M. Goihl, M. Friesdorf, A. H. Werner, W. Brown, and J. Eisert, ArXiv e-prints (2016), [arXiv:1601.02666 \[cond-mat.quant-gas\]](#) .
- [152] T. Giamarchi, *Quantum Physics in One Dimension*, International Series of Monographs on Physics, Vol. 121 (Clarendon, Oxford, 2004).
- [153] B. Sutherland, *Beautiful Models* (2004).
- [154] S. R. White, *Phys. Rev. Lett.* **69**, 2863 (1992).
- [155] S. R. White, *Phys. Rev. B* **48**, 10345 (1993).
- [156] C. D. E. Boschi and F. Ortolani, *The European Physical Journal B* **41**, 503 (2004).
- [157] S. R. White and A. E. Feiguin, *Phys. Rev. Lett.* **93**, 076401 (2004).
- [158] A. E. Feiguin and S. R. White, *Phys. Rev. B* **72**, 220401 (2005).
- [159] O. F. Syljuåsen and A. W. Sandvik, *Phys. Rev. E* **66**, 046701 (2002).
- [160] C. R. Laumann, A. Pal, and A. Scardicchio, *Phys. Rev. Lett.* **113**, 200405 (2014).
- [161] M. Mehta, in *Random Matrices and the Statistical Theory of Energy Levels* (Academic Press, 1967).
- [162] K. Binder, *Phys. Rev. Lett.* **47**, 693 (1981).
- [163] B. I. Shklovskii, B. Shapiro, B. R. Sears, P. Lambrianides, and H. B. Shore, *Phys. Rev. B* **47**, 11487 (1993).
- [164] P. Jacquod and D. L. Shepelyansky, *Phys. Rev. Lett.* **79**, 1837 (1997).
- [165] Y. Y. Atas, E. Bogomolny, O. Giraud, and G. Roux, *Phys. Rev. Lett.* **110**, 084101 (2013).
- [166] R. Nandkishore, S. Gopalakrishnan, and D. A. Huse, *Phys. Rev. B* **90**, 064203 (2014).
- [167] R. Mondaini and M. Rigol, *Phys. Rev. A* **92**, 041601 (2015).
- [168] C. W. J. Beenakker, *Rev. Mod. Phys.* **69**, 731 (1997).

- [169] T. Guhr, A. Müller-Groeling, and H. A. Weidenmüller, *Physics Reports* **299**, 189 (1998).
- [170] M. L. Mehta, *Random matrices* (2004).
- [171] N. Chavda, H. Deota, and V. Kota, *Physics Letters A* **378**, 3012 (2014).
- [172] A. Rodriguez, L. J. Vasquez, K. Slevin, and R. A. Römer, *Phys. Rev. B* **84**, 134209 (2011).
- [173] E. S. Sørensen, M.-S. Chang, N. Laflorencie, and I. Affleck, *Journal of Statistical Mechanics: Theory and Experiment* **2007**, P08003 (2007).
- [174] J. Sato, B. Aufgebauer, H. Boos, F. Göhmann, A. Klümper, M. Takahashi, and C. Trippe, *Phys. Rev. Lett.* **106**, 257201 (2011).
- [175] V. Alba, *Phys. Rev. B* **91**, 155123 (2015).
- [176] D. J. Luitz, ArXiv e-prints (2016), [arXiv:1601.04058](https://arxiv.org/abs/1601.04058) [cond-mat.dis-nn] .
- [177] U. Schneider, L. Hackermüller, J. P. Ronzheimer, S. Will, S. Braun, T. Best, I. Bloch, E. Demler, S. Mandt, D. Rasch, and A. Rosch, *Nat Phys* **8**, 213 (2012).
- [178] M. P. A. Fisher, P. B. Weichman, G. Grinstein, and D. S. Fisher, *Phys. Rev. B* **40**, 546 (1989).
- [179] M. A. Cazalilla, R. Citro, T. Giamarchi, E. Orignac, and M. Rigol, *Rev. Mod. Phys.* **83**, 1405 (2011).
- [180] M. Valiente and D. Petrosyan, *Journal of Physics B: Atomic, Molecular and Optical Physics* **42**, 121001 (2009).
- [181] M. Valiente and D. Petrosyan, *Journal of Physics B: Atomic, Molecular and Optical Physics* **41**, 161002 (2008).
- [182] B. Sutherland, World Scientific, Singapore (2004).
- [183] S. Sorg, L. Vidmar, L. Pollet, and F. Heidrich-Meisner, *Phys. Rev. A* **90**, 033606 (2014).
- [184] D. Muth, D. Petrosyan, and M. Fleischhauer, *Phys. Rev. A* **85**, 013615 (2012).
- [185] L. Taddia, ArXiv e-prints (2013), [arXiv:1309.4003](https://arxiv.org/abs/1309.4003) [cond-mat.str-el] .
- [186] L. Vidmar, S. Langer, I. P. McCulloch, U. Schneider, U. Schollwöck, and F. Heidrich-Meisner, *Phys. Rev. B* **88**, 235117 (2013).

-
- [187] A. Messiah, Dover Publications, Mineola (1999).
- [188] S. Langer, M. J. A. Schuetz, I. P. McCulloch, U. Schollwöck, and F. Heidrich-Meisner, *Phys. Rev. A* **85**, 043618 (2012).
- [189] I. S. Gradshteyn and I. M. Ryzhik, Academic Press, Waltham (2007).
- [190] E. Fradkin, Addison-Wesley, Redwood City (1991).
- [191] M. Valiente, *Phys. Rev. A* **81**, 042102 (2010).
- [192] G. De Chiara, L. Lepori, M. Lewenstein, and A. Sanpera, *Phys. Rev. Lett.* **109**, 237208 (2012).
- [193] L. Lepori, G. De Chiara, and A. Sanpera, *Phys. Rev. B* **87**, 235107 (2013).
- [194] S. M. Giampaolo, S. Montangero, F. Dell’Anno, S. De Siena, and F. Illuminati, *Phys. Rev. B* **88**, 125142 (2013).
- [195] P. D. Francesco, P. Mathieu, and D. Sénéchal, *Conformal Field Theory* (1997).
- [196] G. Morandi, F. Napoli, and E. Ercolessi, *Statistical Mechanics: An Intermediate Course* (2001).
- [197] B. M. McCoy, E. Barouch, and D. B. Abraham, *Phys. Rev. A* **4**, 2331 (1971).
- [198] J. H. H. Perk and H. Au-Yang, *Journal of Statistical Physics* **2009**, 599 (2012).
- [199] M. A. Nielsen and I. L. Chuang, *Quantum Computation and Quantum Information* (2000).
- [200] T. Caneva, R. Fazio, and G. E. Santoro, *Phys. Rev. B* **76**, 144427 (2007).
- [201] L. Cincio, J. Dziarmaga, M. M. Rams, and W. H. Zurek, *Phys. Rev. A* **75**, 052321 (2007).
- [202] F. Pollmann, S. Mukerjee, A. G. Green, and J. E. Moore, *Phys. Rev. E* **81**, 020101 (2010).
- [203] J. Dziarmaga, *Phys. Rev. Lett.* **95**, 245701 (2005).
- [204] A. Polkovnikov, *Phys. Rev. B* **72**, 161201 (2005).
- [205] V. Mukherjee, U. Divakaran, A. Dutta, and D. Sen, *Phys. Rev. B* **76**, 174303 (2007).

-
- [206] B. Damski, *Phys. Rev. Lett.* **95**, 035701 (2005).
- [207] B. Damski and W. H. Zurek, *Phys. Rev. A* **73**, 063405 (2006).
- [208] P. Calabrese and J. Cardy, *Journal of Statistical Mechanics: Theory and Experiment* **2004**, P06002 (2004).
- [209] G. Vidal, J. I. Latorre, E. Rico, and A. Kitaev, *Phys. Rev. Lett.* **90**, 227902 (2003).
- [210] I. Peschel, *Journal of Physics A: Mathematical and General* **36**, L205 (2003).
- [211] M. I. Berganza, F. C. Alcaraz, and G. Sierra, *Journal of Statistical Mechanics: Theory and Experiment* **2012**, P01016 (2012).
- [212] P. Calabrese and A. Lefevre, *Phys. Rev. A* **78**, 032329 (2008).